FACULTY OF SCIENCE
UNIVERSITY OF COPENHAGEN

Dirac points and edge states in 2D materials

Ívar Gunnarsson

Niels Bohr Institute

Master's thesis in Physics

Advisor: Per Hedegård

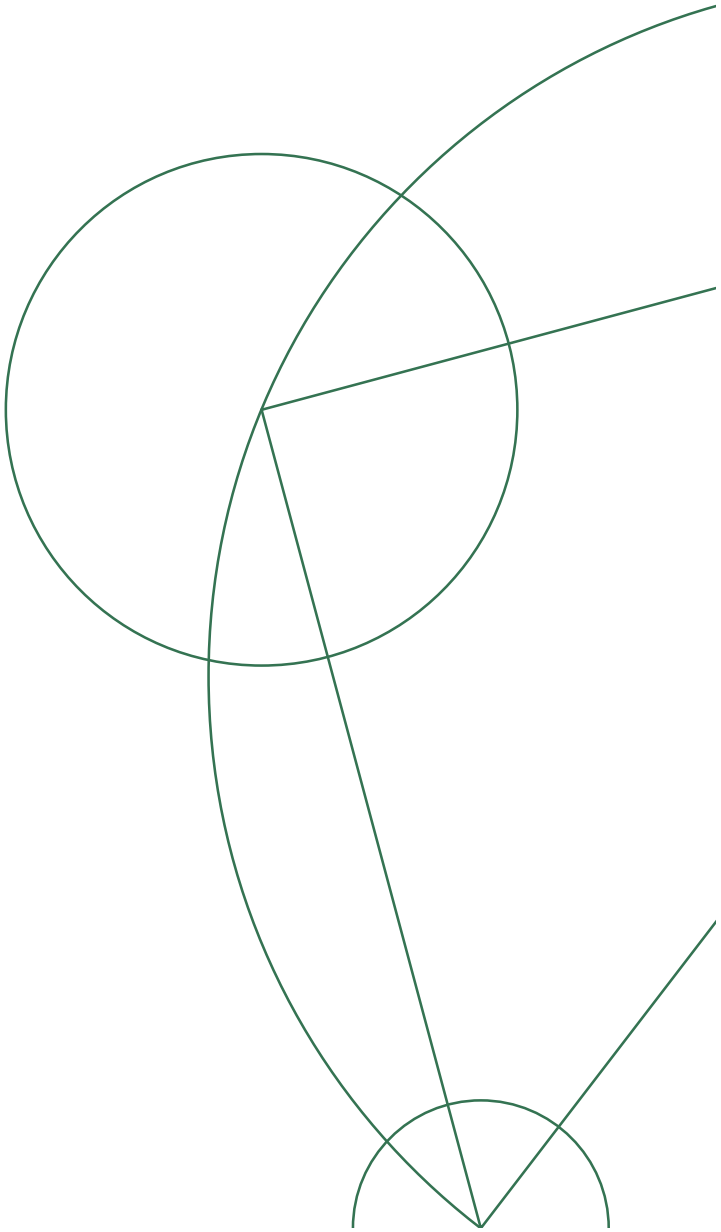

Dated: December 30, 2020

Abstract

In recent years, two-dimensional materials have become an important part of condensed matter physics. These atom-thick materials have been the staple of materials science since the first time single-layer graphene was isolated in 2004 [1], creating much excitement in the condensed matter physics community. Due to their favourable size, and the electronic properties that come along with many 2D materials, they are of immense interest to theorists and experimentalists alike. Having been one of the main focuses of many condensed matter physicists research, there exist a plethora of published papers on graphene and other 2D materials. It is one of the most active fields of research, and the many exotic phenomena intrinsic to 2D materials make it a very exciting field.

There is an outstanding issue, though, an issue that is prevalent in solid state physics. Many calculations are based on rather abstract notions and ideas that are hard to gain physical intuition for. Physics, and other natural sciences, are about prediction and explanation. Using immense computer power, or even just a highly mathematical framework, to calculate some desirable quantity may yield a prediction of said quantity, but does not necessarily offer any real insight into the science that is happening. In this thesis, we aim to bring more intuition to the calculations we perform. We do this by bringing in concepts from quantum chemistry, and apply them to active research topics in 2D carbon-based materials. Alongside analytical calculations, the heuristic model that we introduce proves to be immensely useful in predicting many properties of 2D materials. We apply the heuristic model to graphene nanoribbons (GNRs), which are finite-sized sheets of graphene, with different edge terminations and sizes. The edge and size of a GNR is what determines some of its most important properties, such as its topological classification [2], and it turns out that these highly mathematical definitions have a simple physical explanation within this framework.

The model is also applied to graphynes, graphene-like structures. With the heuristic model, we both provide a physical explanation of some important results, such as why the zigzag edge of graphene is magnetic, and also cast certain properties of graphene and graphynes into a new light, within the heuristic model.

Acknowledgements

First and foremost I would like to thank Per Hedegård, not only for being a great supervisor, but for teaching me a new perspective on physics, and with his (at times, tiring) relentless questioning, to not take everything I read as a given. Thanks to the CMT group for being a fantastic place to work, and to those there who did not hesitate to drop what they were doing, when I asked for help. Thanks to all my friends during the past six years who made studying physics such a pleasure, and especially to Anton Andersen for thorough proofreading.

Contents

1 Introduction **4**
1.1 Thesis outline . . . 4

2 Basics of graphene **6**
2.1 Tight-binding model . . . 6
2.2 Behaviour near **K** and **K′** . . . 9

3 Transfer matrix method **11**
3.1 Isotropic tight-binding model . . . 11
3.2 The Su-Schrieffer-Heeger model . . . 12
3.3 Heuristic model and zigzag graphene . . . 16
3.3.1 The SSH chain in heuristic model . . . 22
3.4 Conclusion . . . 22

4 Graphene nanoribbons **24**
4.1 Dirac points in AGNRs . . . 24
4.1.1 Dirac points in heuristic model . . . 28
4.2 Edge states in AGNRs . . . 29
4.2.1 Reduced AGNR model and zigzag (n = Odd) edge states . . . 29
4.2.2 Zigzag (n = Even) termination . . . 34
4.2.3 Zigzag' (n = Odd) termination . . . 36
4.2.4 Bearded AGNRs . . . 38
4.3 Interface states . . . 41
4.4 Conclusion . . . 44

5 Graphynes **45**
5.1 α-graphyne . . . 45
5.2 β- and γ-graphyne . . . 47
5.3 $(6, 6, 12)$-graphyne . . . 49
5.4 Edge states in graphyne . . . 53
5.4.1 Edge states in β- and γ-graphyne . . . 53
5.4.2 Edge states in (6, 6,12)-graphyne . . . 54
5.5 Graphynes in heuristic model . . . 56
5.5.1 β- and γ-graphyne in heuristic model . . . 56
5.5.2 (6,6,12)-graphyne in heuristic model . . . 57
5.6 Berry phase in graphynes . . . 58
5.6.1 Berry phase in β- and γ-graphyne . . . 62

5.6.2 Berry phase in (6,6,12)-graphyne . . . 62
5.7 Conclusion . . . 64

6 Conclusion and outlook **66**

Appendices **70**

A Neoclassical valence bond theory **70**

B AGNR band structures **73**

C Eigenvalues of discrete Laplacian **74**
C.1 Dirichlet boundary conditions . . . 74
C.2 Neumann boundary conditions . . . 75
C.3 Dirichlet-Neumann boundary conditions . . . 76

D Heuristic model and transfer matrix for AGNRs **78**
D.1 Heuristic model . . . 78
D.2 Bearded AGNR transfer matrix . . . 78
D.3 Zigzag and zigzag' transfer matrices . . . 80

E Interface states in AGNR heterojunctions **84**

F Edge states in (6,6,12) phase diagram **86**

G Berry phase for generic A-B Hamiltonian **88**

Chapter 1

Introduction

Two-dimensional materials are materials that are atom-thick. Considering the atom as a point-sized object, the whole structure is then planar, and importantly the electrons of these atoms are confined to move in this plane. It has long been known that the laws of nature can depend on the dimensionality of a system, and this is especially true in condensed matter physics. Of the many two-dimensional materials that are being researched, the best known is without a doubt graphene. Graphene is 2D carbon-based material that has been predicted to revolutionize the modern world. Repeated stacked layers create graphite, which is common in both electronics as well as everyday objects, like pencils, so graphene as a completely 2D material was proposed well before the turn of the century, and has been one of the stars of solid-state physics for a while now. For a very long time, it was only a theoretical proposal, and due to its being 2D, predicted by many to be thermodynamically unstable. In 2004 this all changed when Geim and Novoselov [1] became the first to produce single-layer graphene, using graphite and a roll of scotch tape, receiving the Nobel Prize in 2010.
Graphene is an incredibly strong material, and a sheet with the mass of cat's whiskers, is said to be strong enough to support the entire cat's weight. It is a gapless semi-metal and is therefore an excellent conductor with very high electron-mobility. The band structure around the Fermi level is linear in the momentum, giving a spectrum identical to that of a massless Dirac fermion, a discovery that gave birth to a "relativistic" branch of condensed matter physics. At half-filling the Dirac fermions are predicted to be the charge carriers, which has indeed been confirmed experimentally [3]. Graphene has been the topic of much of the research done in condensed matter physics the last two decades, and many of the results are based on either heavy numerical calculations, or abstract mathematical formulations of physical models. Both of these approaches have yielded numerous important results, and the intrinsic qualities of the material are known from A to Z. However neither of these approaches offer much physical insight into the underlying processes, or intuition for the results achieved. An example of this is the topological characterisation of graphene nanoribbons, one of the main topics of this thesis. This characterisation is based on an integral over the 1D Brillouin zone, an already abstract concept, and is related to the presence of edge states and Dirac points in the ribbons. In this thesis we represent a model capable of predicting Dirac points and edge states in a given hydrocarbon. The model is based on principles from quantum chemistry and offers a physically intuitive understanding of the results achieved.

1.1 Thesis outline

The thesis is outlined as follows:

- In chapter 2 we introduce the basic concepts of graphene, thereamong its lattice, band structure, Dirac points, and Berry phase.
- In chapter 3 we introduce the transfer matrix formalism, which will lay the mathematical groundwork for much of the work done in this thesis. It is first applied to the isotropic tight-binding model and the Su-Schrieffer-Heeger model, both of which will serve as incredibly important reference points in the following chapters. We also introduce the heuristic model mentioned above, which is capable of giving a physically intuitive description of edge states and Dirac points.
- In chapter 4 we discuss graphene nanoribbons (GNRs). Using the heuristic model introduced in chapter 3, we make predictions of edge states in GNRs and compare them with theoretical calculations. These results can be related to a topological invariant, which determines whether the ribbon is toplogically trivial or nontrivial.
- In chapter 5 we analyse graphynes, which are proposed hydrocarbonic structures, reminiscent of graphene. We describe the materials in an effective model, calculating the band structure and the edge state density. These structures serve as a test of the heuristic model, and the predictions we are able to make from it offer an interesting interpretation of the nature of Dirac points, within the heuristic model.

Chapter 2

Basics of graphene

In this chapter we introduce the basic properties of graphene, such as the lattice, band structure, and the band structure behaviour near the so-called Dirac points. Graphene is a carbon allotrope, with the atoms placed in a hexagonal structure (Figure 2.1). The structure can be divided into two triangular sublattices, which we label A and B (coloured blue and red in Figure 2.1). Each A atom is connected to its three neighbouring B atoms by the vectors

$$\boldsymbol{\delta}_1 = a_0 \frac{1}{2} \begin{pmatrix} -1 \\ -\sqrt{3} \end{pmatrix}, \ \boldsymbol{\delta}_2 = a_0 \frac{1}{2} \begin{pmatrix} 1 \\ -\sqrt{3} \end{pmatrix}, \ \boldsymbol{\delta}_3 = a_0 \begin{pmatrix} 0 \\ 1 \end{pmatrix}. \tag{2.0.1}$$

where $a_0 \simeq 1.4\,\text{Å}$ is the lattice spacing [4].
Carbon, which is the sixth element in the periodic table, when in its free form has the electron configuration $1s^2 2s^2 2p^2$ (given in the standard notation). This means that when found unbounded, the six electrons follow Hund's rules [5] and doubly occupy the 1s, 2s, and 2p orbitals. In graphene, the orbitals hybridise, such that one $2s$ orbital and two $2p$ orbitals have combined to form three orbitals of equal energy, leaving one p_z orbital to be filled. In each carbon atom of graphene, two electrons occupy the 1s orbital, while three electrons occupy the three different sp2 orbitals. The last electron occupies the remaining p_z orbital. The electrons occupying the sp2 orbitals of each atom, form direct overlap bonds with electrons on neighbouring atoms. These bonds are called σ bonds, and are stable enough to be ignored in our Hamiltonian [6]. The sole p_z electron on each atom also bonds with the neighbouring atoms, through a weaker π bond that allows the p_z electrons to hop between neighbouring atoms. The π bonds can be treated in a tight-binding model [6].

2.1 Tight-binding model

The simplest Hamiltonian that models the mobility of the π electrons is a nearest neighbour tight-binding model. This allows the electron of a π orbital to hop to one of its three neighbouring atoms. In second quantisation, the Hamiltonian can be written as

$$H = -t \sum_{\mathbf{r},\boldsymbol{\delta}} \left(c^\dagger_{A,\mathbf{r}} c_{B,\mathbf{r}+\boldsymbol{\delta}} + c^\dagger_{B,\mathbf{r}+\boldsymbol{\delta}} c_{A,\mathbf{r}} \right), \tag{2.1.1}$$

where $t \simeq 2.7\,\text{eV}$ is the hopping integral [4], $c^\dagger_{A,\mathbf{r}}$ is the creation operator that creates an electron on at $\mathbf{r}$, belonging to sublattice A and $c_{A,\mathbf{r}}$ annihilates the same electron. To calculate the band structure we choose the minimal unit cell, which contains one atom from each sublattice. It is highlighted in

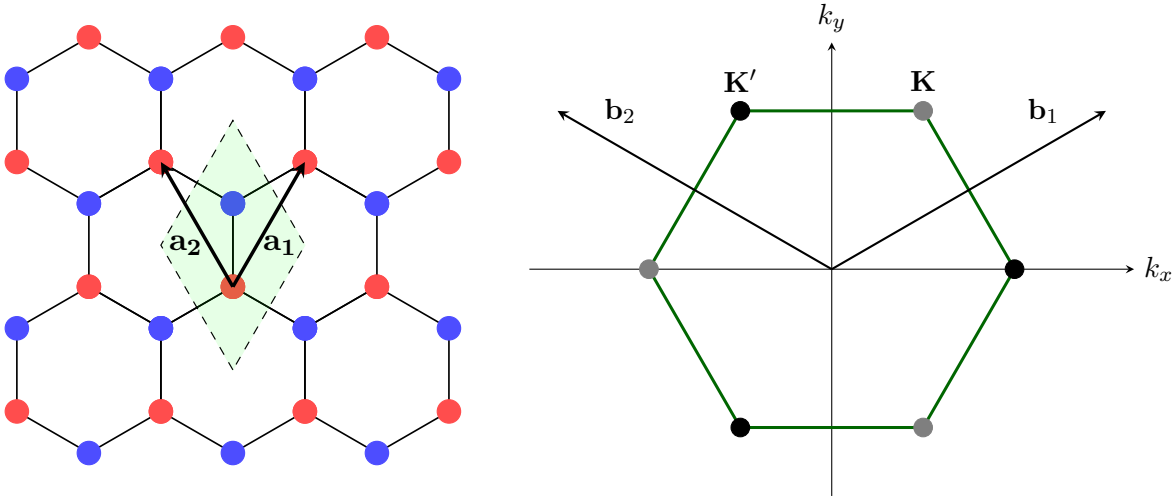

Figure 2.1: *Left*: The hexagonal structure of graphene consists of two interpolating triangular sublattices. *Right*: The first Brillouin zone of graphene. The six corners belong to two inequivalent (not connected by a reciprocal lattice vector) groups of points, $\mathbf{K}$ and $\mathbf{K}'$.

Figure 2.1. The translation vectors are given by

$$\mathbf{a}_1 = \frac{a_0}{2}\begin{pmatrix}\sqrt{3}\\ 3\end{pmatrix}, \tag{2.1.2a}$$

$$\mathbf{a}_2 = \frac{a_0}{2}\begin{pmatrix}-\sqrt{3}\\ 3\end{pmatrix}. \tag{2.1.2b}$$

The reciprocal lattice vectors that satisfy $\mathbf{a}_i \cdot \mathbf{b}_j = 2\pi\delta_{ij}$ are

$$\mathbf{b}_1 = \frac{2\pi}{3a_0}\begin{pmatrix}\sqrt{3}\\ 1\end{pmatrix}, \tag{2.1.3a}$$

$$\mathbf{b}_2 = \frac{2\pi}{3a_0}\begin{pmatrix}-\sqrt{3}\\ 1\end{pmatrix}. \tag{2.1.3b}$$

We transform from the localised states $|\mathbf{r}, A/B\rangle$ to Bloch states, using

$$|\mathbf{k}, A/B\rangle = \frac{1}{\sqrt{N}}\sum_{\mathbf{r}} \mathrm{e}^{i\mathbf{k}\cdot\mathbf{r}}|\mathbf{r}, A/B\rangle, \tag{2.1.4}$$

where N is the number of atoms in the crystal. The Hamiltonian from (2.1.1) can then be written in the momentum space representation, $H = \sum_{\mathbf{k}} c^\dagger_{\mathbf{k}\alpha} h_{\alpha\beta}(\mathbf{k}) c_{\mathbf{k}\beta}$[1] in which it is a 2×2 matrix

$$h(\mathbf{k}) = -t\begin{pmatrix}0 & 1+\mathrm{e}^{i\mathbf{k}\cdot\mathbf{a_1}}+\mathrm{e}^{i\mathbf{k}\cdot\mathbf{a_2}}\\ 1+\mathrm{e}^{-i\mathbf{k}\cdot\mathbf{a_1}}+\mathrm{e}^{-i\mathbf{k}\cdot\mathbf{a_2}} & 0\end{pmatrix} = -t\begin{pmatrix}0 & f(\mathbf{k})\\ f(\mathbf{k})^* & 0\end{pmatrix} = \mathbf{d}(\mathbf{k})\cdot\boldsymbol{\sigma}, \tag{2.1.5}$$

where $\mathbf{d}(\mathbf{k}) = \begin{pmatrix}h_x(\mathbf{k}) & h_y(\mathbf{k})\end{pmatrix}^T$ is a vector containing the real and imaginary parts of $f(\mathbf{k})$, and $\boldsymbol{\sigma}$ is a pseudospin, representing the fact that there are two sublattices. Using some trigonometric identities $f(\mathbf{k})$ can be rewritten

[1] In this thesis we will use lower case h for the matrix representation of a Hamiltonian operator H.

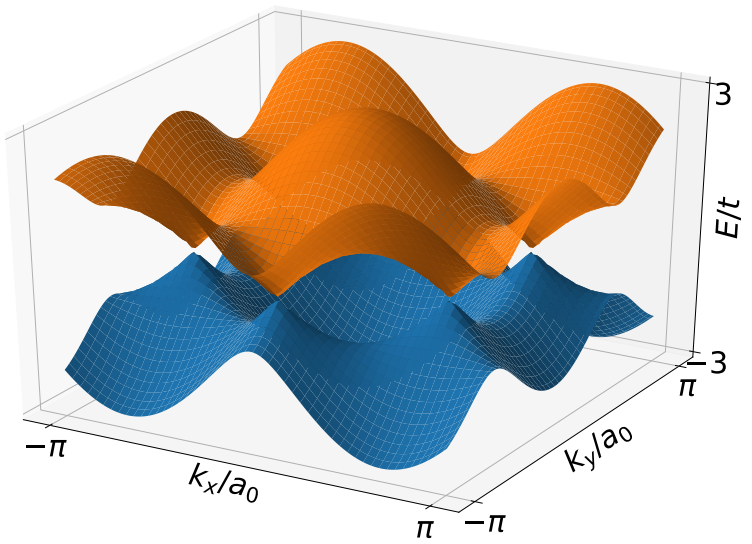

Figure 2.2: Graphene band structure, plotted for $-\pi \leq k_x/a_0 \leq \pi$ and $-\pi \leq k_y/a_0 \leq \pi$. The two bands meet at the six corners of the Brillouin zone. At half filling (one π electron pr. atom), the important features of graphene can be derived from these points.

$$f(\mathbf{k}) = 1 + 2\cos\left(\frac{\sqrt{3}}{2}k_x a_0\right)\cos\left(\frac{3}{2}k_y a_0\right) + 2i\cos\left(\frac{\sqrt{3}}{2}k_x a_0\right)\sin\left(\frac{3}{2}k_y a_0\right). \tag{2.1.6}$$

The spectrum is then given by

$$E(\mathbf{k}) = \pm t|f(\mathbf{k})| = \pm t\sqrt{1 + 4\cos\left(\frac{\sqrt{3}}{2}k_x a_0\right)\cos\left(\frac{3}{2}k_y a_0\right) + 4\cos^2\left(\frac{\sqrt{3}}{2}k_x a_0\right)}, \tag{2.1.7}$$

which is plotted in Figure 2.2. The eigenstates are two component spinors

$$\psi_{\mathbf{k}} = \frac{1}{\sqrt{2}}\begin{pmatrix} e^{-i\phi(\mathbf{k})} \\ 1 \end{pmatrix}, \tag{2.1.8}$$

where $\phi(\mathbf{k})$ is given by

$$\phi(\mathbf{k}) = \tan^{-1}\left(\frac{h_x(\mathbf{k}) - ih_y(\mathbf{k})}{E(\mathbf{k})}\right). \tag{2.1.9}$$

As we have not included an onsite term in the Hamiltonian, the Fermi level, which is where the interesting Physics happens, lies at $E = 0$. The points where two bands meet are therefore of great interest. The zero-points in the energy happen at the points in $\mathbf{k}$-space, where $f(\mathbf{k}) = 0$. As $f(\mathbf{k}) =$

$1+e^{i\mathbf{k}\cdot\mathbf{a}_1}+e^{i\mathbf{k}\cdot\mathbf{a}_2}$ is just a sum of three complex numbers, one of which lies along the positive real axis, the zero-points are found by solving the equations $(\mathbf{K}\cdot\mathbf{a}_1, \mathbf{K}\cdot\mathbf{a}_2) = (2\pi/3, 4\pi/3)$ and $(\mathbf{K}'\cdot\mathbf{a}_1, \mathbf{K}'\cdot\mathbf{a}_2) = (4\pi/3, 2\pi/3)$. The solution for $\mathbf{K}$ is

$$\mathbf{K} = \left(\frac{2\pi}{3\sqrt{3}}, \frac{2\pi}{3}\right), \tag{2.1.10}$$

and for $\mathbf{K}'$, the solutions are

$$\mathbf{K}' = \left(-\frac{2\pi}{3\sqrt{3}}, \frac{2\pi}{3}\right). \tag{2.1.11}$$

2.2 Behaviour near K and K′

At half-filling the lower band is completely filled, while the upper band is completely empty. The behaviour of the valence electrons is therefore dictated by the spectrum around these points. If we define $\mathbf{q} = \mathbf{k} - \mathbf{K}$ as the deviation from $\mathbf{K}$ and assume this deviation to be small, we can expand $f(\mathbf{K}+\mathbf{q})$ to first order to get

$$f(\mathbf{K}+\mathbf{q}) \approx 1 + e^{i\mathbf{K}\cdot\mathbf{a_1}}(1 + i\mathbf{q}\cdot\mathbf{a_1}) + e^{i\mathbf{K}\cdot\mathbf{a_2}}(1 + i\mathbf{q}\cdot\mathbf{a_2}) = \frac{3}{2}q_x - i\frac{3}{2}q_y. \tag{2.2.1}$$

Since $h(\mathbf{k}) = -t\left(\mathrm{Re}\left(f(\mathbf{k})\right)\sigma_x - \mathrm{Im}\left(f(\mathbf{k})\right)\sigma_y\right)$, the Hamiltonian can be written

$$h(\mathbf{K}+\mathbf{q}) = v_F\mathbf{q}\cdot\boldsymbol{\sigma}, \tag{2.2.2}$$

where $v_F = \frac{3t}{2}$ is the Fermi velocity (in unit of $\hbar = a_0 = 1$), and $\boldsymbol{\sigma}$ is a vector of Pauli matrices, coupling the momentum to the pseudospin. At $\mathbf{k}$ close to $\mathbf{K}'$ the Hamiltonian is

$$\begin{aligned} f(\mathbf{K}'+\mathbf{q}) \approx i\frac{\sqrt{3}}{2}q_x\left(e^{i\frac{2\pi}{3}} - e^{i\frac{4\pi}{3}}\right) + i\frac{3}{2}q_y\left(e^{i\frac{2\pi}{3}} + e^{i\frac{4\pi}{3}}\right) = -\frac{3}{2}q_x - i\frac{3}{2}q_y \\ \Rightarrow h(\mathbf{K}'+\mathbf{q}) = v_F\mathbf{q}'\cdot\boldsymbol{\sigma}, \quad \mathbf{q}' = (-q_x, q_y). \end{aligned} \tag{2.2.3}$$

What is remarkable about (2.2.2) and (2.2.3) is that at both $\mathbf{K}$ and $\mathbf{K}'$ the Hamiltonian takes the form of the Dirac equation for massless fermions, a relativistic equation even though the Fermi velocity is two orders of magnitude smaller than the speed of light [7]. The dispersion therefore forms a Dirac cone around the meeting points.

For $\mathbf{k}$ close to $\mathbf{K}$ and $\mathbf{K}'$, we can evaluate the Berry phase. The Berry phase is defined as the phase acquired by a wave function under adiabatic evolution of the parameters of the Hamiltonian, and can therefore be thought of as a "geometric phase" and is very widely used in quantum mechanics. The concept was first popularised by Michael Berry in 1984 [8], in what has become one of the most cited papers on quantum mechanics. A well known example of the appearence of the Berry phase is in the Aharonov-Bohm effect, wherein an electron's energy levels are affected by a magnetic field $\mathbf{B}$, which is only nonzero in a region impenetrable for the electron [9]. Mathematically the phase is defined [9]

$$\gamma_n = i\oint \langle\psi_n(\mathbf{R})\,|\boldsymbol{\nabla}_{\mathbf{R}}|\psi_n(\mathbf{R})\rangle\cdot d\mathbf{R}. \tag{2.2.4}$$

where $\mathbf{R}$ is a vector containing all the parameters of the Hamiltonian. In our case, $\mathbf{R}$ is just $\mathbf{q}$. The

integrand is a purely imaginary quantity as

$$\boldsymbol{\nabla}_{\mathbf{q}}\langle\psi_n(\mathbf{q})|\psi_n(\mathbf{q})\rangle = (\boldsymbol{\nabla}_{\mathbf{q}}\langle\psi_n(\mathbf{q})|)\,|\psi_n(\mathbf{q})\rangle + \langle\psi_n(\mathbf{q})|\,(\boldsymbol{\nabla}_{\mathbf{q}}|\psi_n(\mathbf{q})\rangle) = (\mathbf{A}_{\mathbf{q}})^* + \mathbf{A}_{\mathbf{q}} = 0. \tag{2.2.5}$$

The eigenstates of a Hamiltonian written as $h = q\,\hat{\mathbf{n}}\cdot\boldsymbol{\sigma}$, where $\hat{\mathbf{n}} = (\sin\theta\cos\varphi, \sin\theta\sin\varphi, \cos\theta)$ is a unit-vector, are two-component spinors given by $|\psi_+\rangle = \cos(\theta/2)\,|\uparrow\rangle + \mathrm{e}^{i\varphi}\sin(\theta/2)\,|\downarrow\rangle$, $|\psi_-\rangle = -\mathrm{e}^{-\imath\varphi}\sin(\theta/2)\,|\uparrow\rangle + \cos(\theta/2)\,|\downarrow\rangle$. The polar angle $\theta = \pi/2$, since $\mathbf{q}$ lies in the k_x-k_y plane, so the eigenstates are just

$$|\psi_+\rangle = \frac{1}{\sqrt{2}}\left(|\uparrow\rangle + \mathrm{e}^{i\varphi}\,|\downarrow\rangle\right),\ |\psi_-\rangle = \frac{1}{\sqrt{2}}\left(-\mathrm{e}^{i\varphi}\,|\uparrow\rangle + |\downarrow\rangle\right). \tag{2.2.6}$$

As the eigenstates only depend on φ, the only contribution to the Berry phase comes from A_φ. The Berry phases in the upper and lower bands at $\mathbf{k} = \mathbf{K}$ are then:

$$\gamma_- = i\int_0^{2\pi}\langle\psi_-|\partial_\varphi|\psi_-\rangle d\varphi = \frac{1}{2}\int_0^{2\pi} d\varphi = \pi, \tag{2.2.7a}$$

$$\gamma_+ = i\int_0^{2\pi}\langle\psi_+|\partial_\varphi|\psi_+\rangle d\varphi = -\frac{1}{2}\int_0^{2\pi} d\varphi = -\pi. \tag{2.2.7b}$$

At $\mathbf{k} = \mathbf{K}'$, $q_x \to -q_x \Rightarrow \varphi \to \pi - \varphi$, such that the eigenstates are $|\psi_+\rangle = \frac{1}{\sqrt{2}}|\uparrow\rangle - \frac{1}{\sqrt{2}}\mathrm{e}^{-i\varphi}|\downarrow\rangle$, $|\psi_-\rangle = \frac{1}{\sqrt{2}}\mathrm{e}^{\imath\varphi}|\uparrow\rangle + \frac{1}{\sqrt{2}}|\downarrow\rangle$, so the Berry phase becomes

$$\gamma_- = -\frac{1}{2}\int_0^{2\pi} d\varphi = -\pi, \tag{2.2.8a}$$

$$\gamma_+ = \frac{1}{2}\int_0^{2\pi} d\varphi = \pi, \tag{2.2.8b}$$

which is the opposite of $\mathbf{K}$. The two Dirac points having opposite Berry phase means that, if the hopping parameters are varied, they can come together to annihilate with each other and open a gap [10]. We will discuss this further in chapter 5, and give specific examples of how it happens.

Chapter 3

Transfer matrix method

In two-dimensional materials, edge states play an important role in a variety of contexts. They are states whose wave function is confined to the edge of some material. That means that when the electron attempts to move into the bulk, its propagation is suppressed and the energy needed to move further into the bulk increases. Edge states play an important role in condensed matter physics, not least in the field of topology. The number of edge states present in a model can be linked to a topological invariant [11], determining which topological phases can exist in a material. The robustness of edge states can also say something about the robustness of the topological phases at play, and which symmetries may protect them.
In this chapter we develop a method that can determine whether a given model supports edge states. The method is simple and uses the transfer matrix, a powerful tool that among other things is used to solve the 1D Ising model. The idea is to use the Schrödinger equation to obtain an iterative expression for the probability amplitude for each site in the wave function that is a solution to $H\psi = E\psi$. To illustrate the method, we show that the simple isotropic tight-binding model in one dimension with open boundary conditions does not support localised edge states.

3.1 Isotropic tight-binding model

In first quantisation, the isotropic tight-binding Hamiltonian of a 1D chain is

$$H = -t \sum_{i=1} \left(|i\rangle\langle i+1| + |i+1\rangle\langle i| \right), \tag{3.1.1}$$

where $|i\rangle$ is an orbital localised to the i^{th} atom. This could for example describe the π-electrons in polyacetylene [6]. As the localised orbitals form a complete set, any eigenstate of the Hamiltonian can be expressed in their basis

$$H|\psi\rangle = E|\psi\rangle, \ |\psi\rangle = \sum_{i=1} a_i \, |i\rangle \, . \tag{3.1.2}$$

Taking the inner product with some localised state bra, $\langle j|$, on both sides, we get

$$\langle j| \sum_{i=1} a_i H|i\rangle = E\langle j| \sum_{i=1} a_i |i\rangle \Rightarrow \langle j| \sum_{i=1} a_i \left(|i+1\rangle + |i-1\rangle \right) = E \sum_{i=1} a_i \langle j|i\rangle. \tag{3.1.3}$$

As the orbitals are orthonormal, $\langle j|i\rangle = \delta_{ij}$, where δ_{ij} is the Kronecker delta, we get

$$-t\left(a_{j-1}+a_{j+1}\right)=Ea_j \quad \Rightarrow \quad a_{j+1}=-\frac{E}{t}a_j-a_{j-1}. \tag{3.1.4}$$

We have now determined an iterative expression for the probability amplitude on each site in the model. To see if this expression allows for edge states, we introduce the vector $\beta_j=\begin{pmatrix}a_j & a_{j-1}\end{pmatrix}^T$. The vector β_{j+1} is then

$$\beta_{j+1}=\begin{pmatrix}a_{j+1}\\ a_j\end{pmatrix}=\begin{pmatrix}-\frac{E}{t} & -1\\ 1 & 0\end{pmatrix}\begin{pmatrix}a_j\\ a_{j-1}\end{pmatrix}=T\beta_j. \tag{3.1.5}$$

Let $\beta_1=\begin{pmatrix}a_1 & 0\end{pmatrix}^T=xB_++yB_-$. Here we have utilized that since T is diagonizable, we can write any vector as a linear combination of its eigenvectors, $B_\pm$. Since $\beta_{j+1}=T^j\beta_1$, we can express β_{j+1} using the eigenvalues and eigenvectors of T:

$$\beta_{j+1}=T^j\left(xB_++yB_-\right)=x\lambda_+^jB_++y\lambda_-^jB_-. \tag{3.1.6}$$

The eigenvalues $\lambda_\pm$ are found by solving the secular equation:

$$\left(-\frac{E}{t}-\lambda\right)(-\lambda)-(-1)=0 \quad \Rightarrow \quad \lambda_\pm=-\frac{E}{2t}\pm\sqrt{\left(\frac{E}{2t}\right)^2-1}. \tag{3.1.7}$$

There are two areas of interest: the one where $\left|\frac{E}{2t}\right|\leq 1$ and where $\left|\frac{E}{2t}\right|>1$. In the first case we can write $-\frac{E}{2t}=\cos(k)$, which means

$$\lambda_\pm=\mathrm{e}^{\pm ik}. \tag{3.1.8}$$

This corresponds to the usual the bulk plane wave solution to the Schrödinger equation, with eigenvalue $E=-2t\cos(k)$. This wave function is delocalised, and its probability amplitude is constant in the entire crystal. The other scenario, $\left|\frac{E}{2t}\right|>1$ lets us write $-\frac{E}{2t}=\cosh\kappa$ (up to a sign) and means that

$$\lambda_\pm=\cosh\kappa\pm|\sinh\kappa|. \tag{3.1.9}$$

The convention chosen here means that $|\lambda_+|>1$ and $|\lambda_-|<1$. The consequence is the first term on the r.h.s. of (3.1.6) increases exponentially uninhibited into the bulk, which normalisation of the wave function forbids. To compensate for this we must set $x=0$, which leaves us with

$$\beta_1=yB_-. \tag{3.1.10}$$

As $\beta_1\propto\begin{pmatrix}1 & 0\end{pmatrix}^T$ which is not an eigenvector of T (T has off-diagonal elements), the above equation is a contradiction. There are therefore no edge states in the isotropic tight-binding model.

3.2 The Su-Schrieffer-Heeger model

The Su-Schrieffer-Heeger (SSH) model is a nearest neighbour tight-binding model where the hopping integral is staggered, and alternates between every pair of sites. Its simplicity makes it very valuable, and we shall repeatedly refer back to it, and will therefore cover it extensively in this section. The staggered hopping increases the unit cell, which now contains two inequivalent sites which we refer to as A and B sites (red and blue sites respectively in Figure 3.1). In this section we calculate the

spectrum and show that for $t_1 < t_2$ the model supports edge states and has a quantised Zak phase, where t_1 is intracell hopping parameter, and t_2 is the intercell parameter (see Figure 3.1).

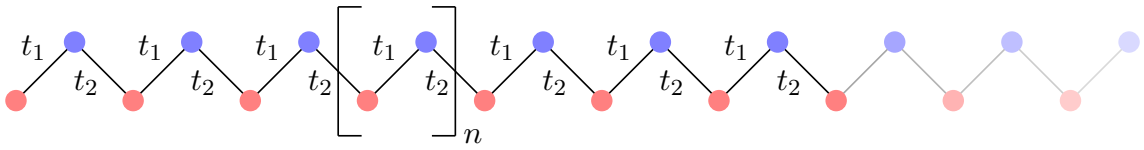

Figure 3.1: The Su-Schrieffer-Heeger chain, with alternating hopping amplitudes.

The Hamiltonian describing this model is

$$H = -\sum_{j=1} \left[t_1 \left(|j, A\rangle\langle j, B| + |j, B\rangle\langle j, A| \right) + t_2 \left(|j, B\rangle\langle j+1, A| + |j+1, A\rangle\langle j, B| \right) \right]. \tag{3.2.1}$$

Note that here the sum is over unit cells, in each of which there are two sites – before each unit cell contained one site and the distinction was arbitrary. To find the bulk spectrum, we apply periodic boundary conditions and transform the localised state kets $|i, A/B\rangle$ to Fourier space

$$|k, A/B\rangle = \frac{1}{\sqrt{N}} \sum_{j=1}^{N} \mathrm{e}^{-ikj} |i, A/B\rangle, \tag{3.2.2}$$

where N is the number of atoms in the chain. Writing the Hamiltonian in the basis of $|k, A/B\rangle$

$$H|k, A\rangle = -\left(t_1 + \mathrm{e}^{-ik} t_2\right) |k, B\rangle, \tag{3.2.3}$$

$$H|k, B\rangle = -\left(t_1 + \mathrm{e}^{ik} t_2\right) |k, A\rangle, \tag{3.2.4}$$

gives the 2×2 Hamiltonian

$$h = -\begin{pmatrix} 0 & t_1 + \mathrm{e}^{ik} t_2 \\ t_1 + \mathrm{e}^{-ik} t_2 & 0 \end{pmatrix} = -\left(t_1 + t_2 \cos(k)\right) \sigma_x + t_2 \sin(k) \sigma_y. \tag{3.2.5}$$

The spectrum is then given by

$$E(k) = \pm \sqrt{t_1^2 + t_2^2 + 2 t_1 t_2 \cos k}, \tag{3.2.6}$$

which is gapped for $t_1 \neq t_2$ with a band gap of $\Delta = 2|t_1 - t_2|$.
We now look for eigenstates of the Hamiltonian that do not belong to the above given spectrum of Bloch waves, once again using the transfer matrix method. Let $|\psi\rangle = \sum_{j=1} \left(a_j |j, A\rangle + b_j |j, B\rangle \right)$ be an eigenstate of the Hamiltonian. We can split the Schrödinger equation in two by taking the inner product with both $\langle n, A|$ and $\langle n, B|$:

$$\langle n, A|H|\psi\rangle = E\langle n, A|\psi\rangle \quad \Rightarrow \quad -\left(t_1 b_n + t_2 b_{n-1}\right) = E a_n, \tag{3.2.7}$$

$$\langle n, B|H|\psi\rangle = E\langle n, B|\psi\rangle \quad \Rightarrow \quad -\left(t_1 a_n + t_2 a_{n+1}\right) = E b_n. \tag{3.2.8}$$

As (3.2.7) holds for all n, we can let $n \to n+1, n-1 \to n$ and obtain an equation for the vector $\beta_{n+1} = \begin{pmatrix} b_{n+1} & a_{n+1} \end{pmatrix}^T$. This equation is expressed as

$$\beta_{n+1} = T \beta_n, \tag{3.2.9}$$

where the transfer matrix T is

$$T = \begin{pmatrix} \frac{E^2}{t_1 t_2} - \frac{t_2}{t_1} & \frac{E}{t_2} \\ -\frac{E}{t_2} & -\frac{t_1}{t_2} \end{pmatrix}. \tag{3.2.10}$$

Writing $\beta_1 = \begin{pmatrix} b_1 & a_1 \end{pmatrix}^T = xB_+ + yB_-$, as above we get $\beta_{n+1} = T^n \beta_1 = x\lambda_+^n B_+ + y\lambda_-^n B_-$. The eigenvalues are

$$\lambda_\pm = \frac{E^2 - t_1^2 - t_2^2}{2t_1 t_2} \pm \sqrt{\left(\frac{E^2 - t_1^2 - t_2^2}{2t_1 t_2}\right)^2 - 1} = X \pm \sqrt{X^2 - 1}. \tag{3.2.11}$$

Once again, $-1 \leq X \leq 1$ corresponds to Bloch waves. For $X > 1$, $\lambda_+ > 1$ and for $X < -1$, $\lambda_- < -1$. The former case indicates $E^2 > 2t_1 t_2 + t_1^2 + t_2^2$, which means that E either lies below the valence band or above the conduction band. As this is not a very realistic outcome, we look at $X < -1 \Rightarrow E < |t_1 - t_2|$ meaning that E lies in the band gap. When $|\lambda_+| < 1$ and $|\lambda_-| > 1$, we must set $y = 0$ for the wavefunction to be normalisable. When $y = 0$, which means $\beta_1 \propto B_+$, the ratio between the coefficients of B_+ must equal $b_1/a_1 = -E/t_1$. The eigenvectors $B_\pm$ are

$$B_\pm = \frac{1}{\sqrt{2}} \begin{pmatrix} -\frac{t_1 + t_2 \lambda_\pm}{E} \\ 1 \end{pmatrix}, \tag{3.2.12}$$

which we have chosen to normalise. As the ratio between the vector's elements is simply the top element, we now have an equation for E which we can solve analytically.

$$-\frac{t_1}{E} - \frac{t_2}{E}\lambda_+ = -\frac{E}{t_1} \quad \Rightarrow \quad E^2 = \frac{E^2 + t_1^2 - t_2^2}{2} + \frac{1}{2}\sqrt{E^4 - 2E^2\left(t_1^2 + t_2^2\right) + \left(t_2^2 - t_1^2\right)}. \tag{3.2.13}$$

As the l.h.s. goes to zero as $E \to 0$, so must the right. We expand the square root to second order around $E = 0$:

$$E^2 \approx \frac{E^2}{2} + \frac{t_1^2 - t_2^2}{2} + \frac{\sqrt{\left(t_2^2 - t_1^2\right)^2}}{2} - \frac{E^2\left(t_1^2 + t_2^2\right)}{\sqrt{\left(t_2^2 - t_1^2\right)^2}} = \frac{E^2}{2} + \frac{t_1^2 - t_2^2}{2} + \frac{|t_2^2 - t_1^2|}{2} + \frac{E^2\left(t_1^2 + t_2^2\right)}{|t_2^2 - t_1^2|}. \tag{3.2.14}$$

In order for the r.h.s to go to zero as $E \to 0$, the second and third term must cancel which they exactly do in the case $t_2 > t_1$. The SSH model therefore supports a localised edge state at the end of the chain, as long as $t_2 > t_1$, a crucial feature we shall come back to later. The energy of the edge state is $E = 0$, a surprising detail, as it is not completely localised to the first site, but rather decays into the chain. It is a straightforward matter to verify this numerically. Simulating a chain with $N = 100$ sites, we find an edge state with energy $E = 0$ at each end of the chain, see Figure 3.2. If we had not had an even number of sites (i.e. an integer number of unit cells), we would only have one edge state. The fact that the state has zero energy is not totally intuitive since it decays into the bulk, but it is actually very simple to construct the state's wave function, explaining this. If we only allow the state to live on the A sites, the state is (for some normalisation constant R)

$$|\psi\rangle = R\sum_{j=1}(a_j|j,A\rangle + b_j|j,B\rangle) = R\sum_{j=1} a_j|j,A\rangle, \tag{3.2.15}$$

then each B site's two neighbours must interfere destructively:

$$-t_1 a_j - t_2 a_{j+1} = b_j E = 0 \Rightarrow a_{j+1} = -\frac{t_1}{t_2}a_j. \tag{3.2.16}$$

As $t_1 < t_2$ this gives an exponentially decreasing wavefunction

$$|\psi\rangle = R\sum_{j=1}\left(-\frac{t_1}{t_2}\right)^{j-1}|j,A\rangle. \tag{3.2.17}$$

We now determine R:

$$\langle\psi|\psi\rangle = 1 \Rightarrow R^2\sum_{j=1}\left(-\frac{t_1}{t_2}\right)^{2j-2} = R^2\frac{t_2^2}{t_1^2}\sum_{j=1}\left[\left(-\frac{t_1}{t_2}\right)^2\right]^j = 1, \tag{3.2.18}$$

as $|t_1/t_2| < 1$ and the sum is just a geometric series, we get

$$R^2\frac{t_2^2}{t_1^2}\frac{1}{1-\left(-\frac{t_1}{t_2}\right)^2} = 1 \Rightarrow R = \frac{t_1}{t_2}\sqrt{1-t_1^2/t_2^2}, \tag{3.2.19}$$

giving us the wave function for the edge state

$$|\psi\rangle = \frac{t_1}{t_2}\sqrt{1-t_1^2/t_2^2}\sum_{j=1}\left(-\frac{t_1}{t_2}\right)^{j-1}|j,A\rangle. \tag{3.2.20}$$

The wave function explains the alternating sign of a_j that we see in Figure 3.2.
As in the isotropic case, the transfer matrix eigenvalues can also directly give the Bloch wave spectrum. As $\lambda_+\lambda_- = 1$, $|\lambda_\pm| = 1$ corresponds to the plane wave states $\lambda_\pm = \mathrm{e}^{\pm ik}$. Solving the equation

$$\lambda_+ = \cos(k) + i\sin(k) \quad \Rightarrow \quad \frac{E^2 - t_1^2 - t_2^2}{2t_1t_2} = \cos(k) \quad \Rightarrow \quad E = \pm\sqrt{t_1^2 + t_2^2 + 2t_1t_2\cos(k)} \tag{3.2.21}$$

shows us how powerful the transfer matrix is, as it contains information about both the bulk spectrum and the localised edge states.
Before moving on from the SSH model, we calculate the Zak phase in the (at half-filling) occupied band using the transfer matrix's eigenvectors. In the bulk $\lambda_\pm = \mathrm{e}^{\pm ik}$, so the eigenvectors become

$$\mathbf{B}_\pm = \frac{1}{\sqrt{2}}\begin{pmatrix} -\dfrac{t_1 + t_2\mathrm{e}^{\pm ik}}{E} \\ 1 \end{pmatrix} = \frac{1}{\sqrt{2}}\begin{pmatrix} z_\pm/E \\ 1 \end{pmatrix}, \tag{3.2.22}$$

where E is the norm of $z = |z|\mathrm{e}^{i\varphi}$, and φ is given by

$$\varphi = \arctan\left(\frac{t_2\sin(k)}{t_1 + t_2\cos(k)}\right). \tag{3.2.23}$$

The Zak phase is defined [11]

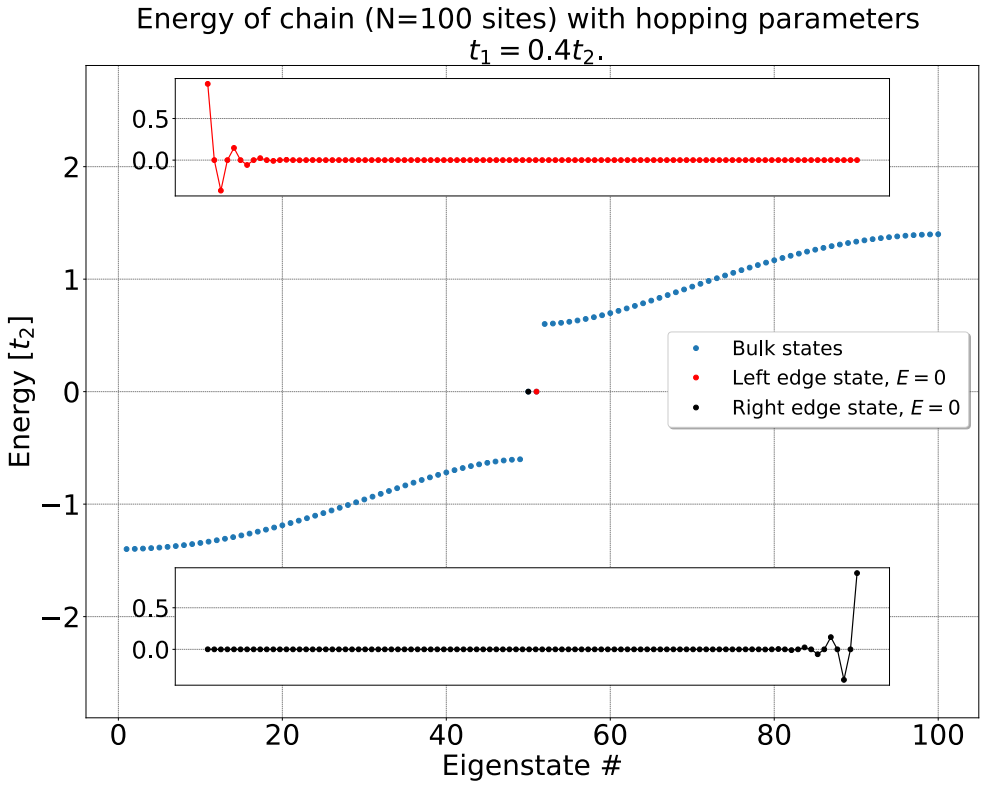

Figure 3.2: Numerical results of the SSH model for $t_1 = 0.4t_2$ (t_1 is the intracell hopping parameter) with 100 sites. We find an edge state at each end of the chain.

$$\gamma = i \int_{-\pi}^{\pi} dk \langle \psi_k | \partial_k | \psi_k \rangle, \tag{3.2.24}$$

where the integrand is just the Berry connection that also appeared in the Berry phase in the previous chapter. As the boundary does not put any constraints on the bulk eigenvectors, $|\psi_k\rangle$, they can therefore be taken to be any of the transfer matrices eigenvectors. Choosing B_+ gives us the expression

$$\gamma = i \int_{-\pi}^{\pi} dk \ (\mathbf{B}_+)^* \cdot (\partial_k \mathbf{B}_+) = \frac{i}{2} \int_{-\pi}^{\pi} dk \, \mathrm{e}^{-i\varphi} \partial_k \mathrm{e}^{i\varphi} = -\frac{1}{2} \int_{-\pi}^{\pi} dk \, \partial_k \varphi. \tag{3.2.25}$$

This integral is a contour integral in the complex z-plane. The contour is a circle with its centre at $(t_1, 0)$ and radius $|t_2|$. If the contour winds about the origin once, the integral equals 2π, and if it does not, the integral is equal to zero. For $t_1 < t_2$, it winds about the origin, while for $t_1 > t_2$ it does not (see Figure 3.3). When $t_1 = t_2$, it is ill defined and a convention must be chosen. We will discuss this ambiguity more in the next chapter.

3.3 Heuristic model and zigzag graphene

Having shown that edge states exist in the SSH model, we now move on to a bigger beast, namely graphene. It is well established that graphene with a zigzag termination supports edge states [10, 12],

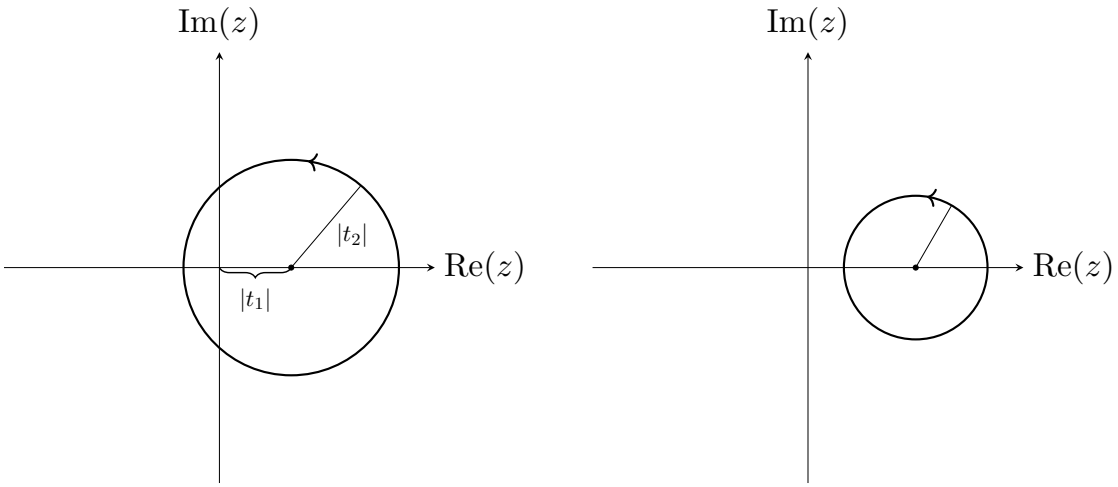

Figure 3.3: *Left*: As $t_1 < t_2$, the contour of integration winds around the origin once, so the integral in (3.2.25) is nonzero. *Right*: $t_1 < t_2$, so the contour does not wind around the origin and the integral is zero.

but the density of edge states along the zigzag boundary is not as well established. To give a prediction of the edge state density and a physical understanding of their origin, we introduce a heuristic model based on methods used in chemistry. In order to properly establish the heuristic model, we start by making some very basic considerations about the tight-binding model: consider two π electrons on neighbouring carbon atoms whose localised states are $|1\rangle$ and $|2\rangle$, connected by the hopping matrix element t, such that $H|1\rangle = -t|2\rangle$ and vice versa ($t > 0$). The Hamiltonian ground state is then the even linear combination the two $(|1\rangle + |2\rangle)/\sqrt{2}$, also called the bonding orbital. The many-body ground state of the system is the one where both electrons occupy the bonding orbital, with their spins pointing in opposite directions – the energy is $-2t$, and the gap between the bonding orbital and the anti-bonding orbital (odd combination of the two atomic orbitals) is $2t$. Visually we can represent this by a double bond between the two atoms, see Figure 3.4, with the bonding orbital representing one of the bonds and the implicit σ-bond present representing the other.

$$\mathrm{C}{=}{=}\mathrm{C}$$

Figure 3.4: Double bond between two Carbon atoms as a visualisation of the state $|\text{even}\rangle = (|1\rangle + |2\rangle)/\sqrt{2}$.

Constructing the ground state of a system of carbon atoms can then be loosely seen as filling the system with as many double bonds as possible. In Figure 3.5 polyacetylene $(C_2H_2)_3$ is drawn with carbon atoms at each corner and double bonds placed in different configurations. If we think of the two configurations as quantum mechanical states, the first configuration would be $d^\dagger_{\text{even},12}d^\dagger_{\text{even},34}d^\dagger_{\text{even},56}|0\rangle$ and the second would be $d^\dagger_{\text{even},14}d^\dagger_{\text{even},23}d^\dagger_{\text{even},45}|0\rangle$, where $d^\dagger_{\text{even},ij}$ creates an electron pair on the sites i and j in an even linear combination. It is important to note that neither of the two states are actual eigenstates of the full tight-binding Hamiltonian, as for example the $2 \to 3 + (\text{h.c.})$ term in the Hamiltonian acting on the first configuration does not return the same state. The ground state is instead some superposition of the two configurations along with some excited states which carry less weight. So rather than giving an exact picture of the ground state of the system, filling a material such as polyacetylene with double bonds can give us a rough idea of the ground state energy, and how

many unpaired electrons there might be (i.e. if we are not able to pair up every electron). For example if we were to take an open chain like polyacetylene, but with an odd number of carbon atoms, this method correctly predicts one unpaired zero-energy state.

Figure 3.5: Polyacetylene with double bonds drawn in two different configurations. The Carbon atoms are located at the corners, with implicit hydrogen atoms outside the corners.

If we instead take a closed chain of carbon atoms like benzene (see Figure 3.6) the spectrum is $E = -2t\cos(k)$ with $k \in [-2\pi/3, -\pi/3, 0, \pi/3, 2\pi/3, \pi]$, since periodic boundary conditions apply. At half-filling the ground state is the one where the $k = 0, \pm\pi/3$ levels are doubly occupied and the ground state energy of the system is $-8t$, and the gap between the highest occupied and lowest unoccupied state is $2t$ – this gap is the true measure of the stability of the benzene ring, an important point we will return to when we discuss graphynes (graphene-like structures). This state is represented by a ring inside the benzene structure. Besides being a closed chain which gives it an energetic advantage over a polyacetylene chain of the same size $(C_2H_2)_3$, benzene has a special stability related to its aromaticity [13], a property that unfortunately is beyond the scope of this thesis. In this heuristic model a circle is more stable than the alternative of placing three double bonds. The name of the game is therefore to fill any material we are concerned with with as many circles and double bonds as possible, and if there are any sites that are left unpaired we predict the existence of an edge state.
Graphene as a material can be seen as a repeating set of connected benzene rings, where each carbon-hydrogen bond of benzene is replaced by a σ-bond pairing carbon atoms of two neighbouring rings. Zigzag graphene is known to support edge states which our model also predicts, as we shall see: we start by drawing as many circles as possible, and when that is done, we draw double bonds on any remaining pairs. The formalism is sketched in Figure 3.7 with zigzag graphene as the example. In the sketching we have neglected double bonds on the bottom edge and on the sides, as we are concerned with zigzag graphene that has translational invariance in the x-direction and is semi-infinite in the y-direction.
The model predicts an unpaired electron on every third site along the zigzag edge. We can confirm this both analytically and numerically. Numerically it is a simple matter of simulating a graphene sheet of finite size and vary the width such that the zigzag edge becomes longer and longer, and calculate the number of edge states for varying number of unit cells. For a graphene sheet with two zigzag terminations, we would expect one edge state for every third unit cell (the unit cell is defined in the first sketch in Figure 3.7) on each edge, so all in all 3/2 unit cells pr. edge state. This numerical analysis is done with the Python package Pybinding [14], and gives exactly the result we expect (see the linear fit in Figure 3.8).
To confirm the finding analytically we replace the localised states $|m; i, j\rangle$, where m refers to the position inside the unit cell (site enumeration is given in Figure 3.7) and i and j refer to the horizontal and vertical position of the unit cell, with a semi-localised state $|m; k_x, j\rangle$, where k_x is the wave number of the Bloch wave. In doing this, we assume translational invariance in the x-direction. Inside the unit cell j there are four sites, two of which are connected to neighbouring unit cells $j \pm 1$. We can reduce the problem to the SSH model by introducing two projection operators Q and P. Q projects into states that are not connected to neighbouring unit cells (sites 2 and 3), and P projects into states that are (sites 1 and 4). The two sum to identity, are orthogonal and idempotent. An effective Hamiltonian can then be constructed acting on each subspace. As we are mainly interested in the P states, we derive the effective Hamiltonian on that subspace, H_P (the derivation is of course identical for the

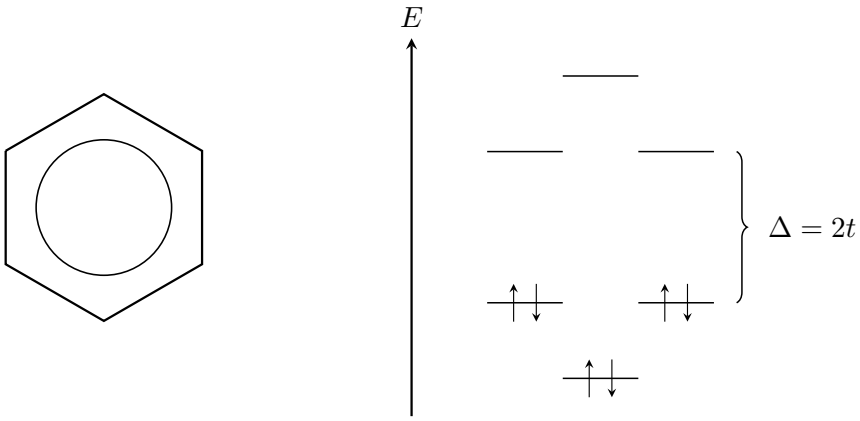

Figure 3.6: *Left*: Ground state drawing of benzene, with the circle representing the aromaticity of the compound. *Right*: The spectrum, with the three lowest orbitals doubly occupied to give a many-body ground state energy of $-8t$ and excitation energy of $2t$.

two). Using their idempotence, the identity $\mathbb{1} = P + Q$ and multiplying from the left by P and Q each on the Schrödinger equation, we get

$$H\left|\psi\right\rangle = E\left|\psi\right\rangle \Rightarrow PH(P+Q)\left|\psi\right\rangle = EP\left|\psi\right\rangle \Rightarrow PHP\left|\psi_P\right\rangle + PHQ\left|\psi_Q\right\rangle = E\left|\psi_P\right\rangle, \tag{3.3.1a}$$

$$H\left|\psi\right\rangle = E\left|\psi\right\rangle \Rightarrow QHP\left|\psi_P\right\rangle + QHQ\left|\psi_Q\right\rangle = E\left|\psi_Q\right\rangle \Rightarrow \left|\psi_Q\right\rangle = (E - QHQ)^{-1}QHP\left|\psi_P\right\rangle, \tag{3.3.1b}$$

where $\left|\psi_P\right\rangle = P\left|\psi\right\rangle$ and $\left|\psi_Q\right\rangle = Q\left|\psi\right\rangle$, giving us an effective Hamiltonian on the P subspace

$$H_P = PHP + PHQ\frac{1}{E - QHQ}QHP \tag{3.3.2}$$

for which the states $\left|\psi_P\right\rangle$ satisfy their own effective Schrödinger equation $H_P\left|\psi_P\right\rangle = E\left|\psi_P\right\rangle$. H_P itself depends on the eigenvalue of the full Hamiltonian $H = H_P + H_Q$ so the equation must be solved self consistently or with an ansatz. The first term in H_P is the usual hopping term between the bottom site of one unit cell and the top site of the unit cell below. The second term gives an onsite energy proportional to E, and an effective hopping term from $m = 1 \to 4$:

$$\begin{aligned} H_P\left|1; k_x, j\right\rangle &= -t\left|4; k_x, j+1\right\rangle + PHQ\frac{1}{E - QHQ}\left(1 + \mathrm{e}^{-ik_x}\right)\left|2; k_x, j\right\rangle \\ &= -t\left|4; k_x, j+1\right\rangle - t\left(1 + \mathrm{e}^{-ik_x}\right)\frac{1}{E^2 - t^2}\left(E\left|2; k_x, j\right\rangle - t\left|3; k_x, j\right\rangle\right) \\ &= -t\left|4; k_x, j+1\right\rangle + \frac{t^2 E}{E^2 - t^2}\left|1; k_x, j\right\rangle - \frac{t^3}{E^2 - t^2}\left(2 + 2\cos k_x\right)\left|4; k_x, j\right\rangle. \end{aligned} \tag{3.3.3}$$

As H_P is hermitian, we get the same $4 \to 1$ hopping term. We know the SSH model has a zero-energy edge state when $|t_1| < |t_2|$. We therefore make the ansatz $E = 0$ such that the onsite potential vanishes and the effective hopping which we label $\tilde{t}$ becomes $\tilde{t} = -4t\cos^2(k_x/2)$. The model is now completely reduced to the SSH model with $t_1 \to \tilde{t}$ and $t_2 \to t$. $\tilde{t}(E = 0, k_x)$ is plotted in Figure 3.9. At $k_x = \pm 2\pi/3$, $|\tilde{t}| = t$ and becomes smaller than t for $|k| > 2\pi/3$ – that is to say $|\tilde{t}(E = 0, k_x)|$ is smaller than $|t|$ for exactly one third of the allowed values of k_x, confirming that zigzag graphene carries an edge state on every third site along the edge. These calculations also explain why graphene is non-magnetic in the bulk, but magnetic along the zigzag edge. The bulk is non-magnetic because

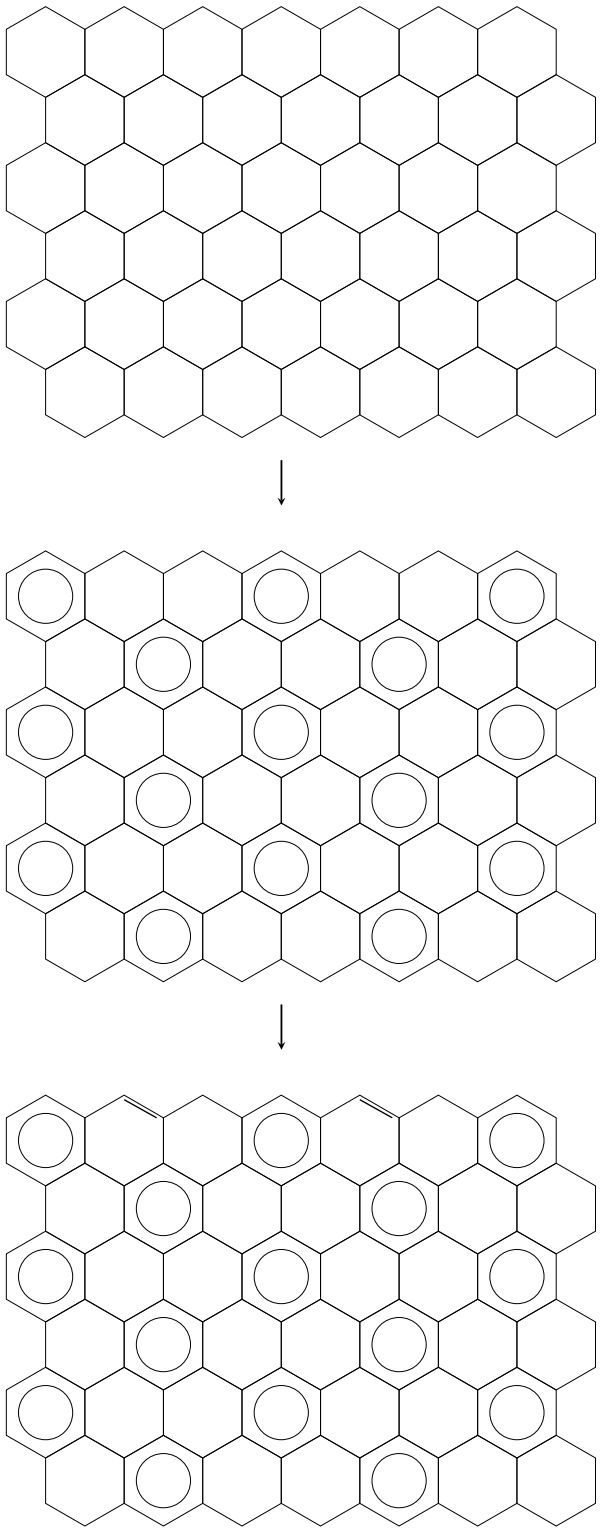

Figure 3.7: Filling graphene with circles and double bonds to construct the many body ground state. In the first step we fill in as many circles as possible. In the second step we pair the remaining unpaired electrons along the zigzag edge with a double bond, leaving one unpaired electron on every third site on the edge. The density of unpaired electrons on the zigzag edge is then predicted to be 1/3. Without an edge (translational invariance in both directions) there would be no need for double bonds.

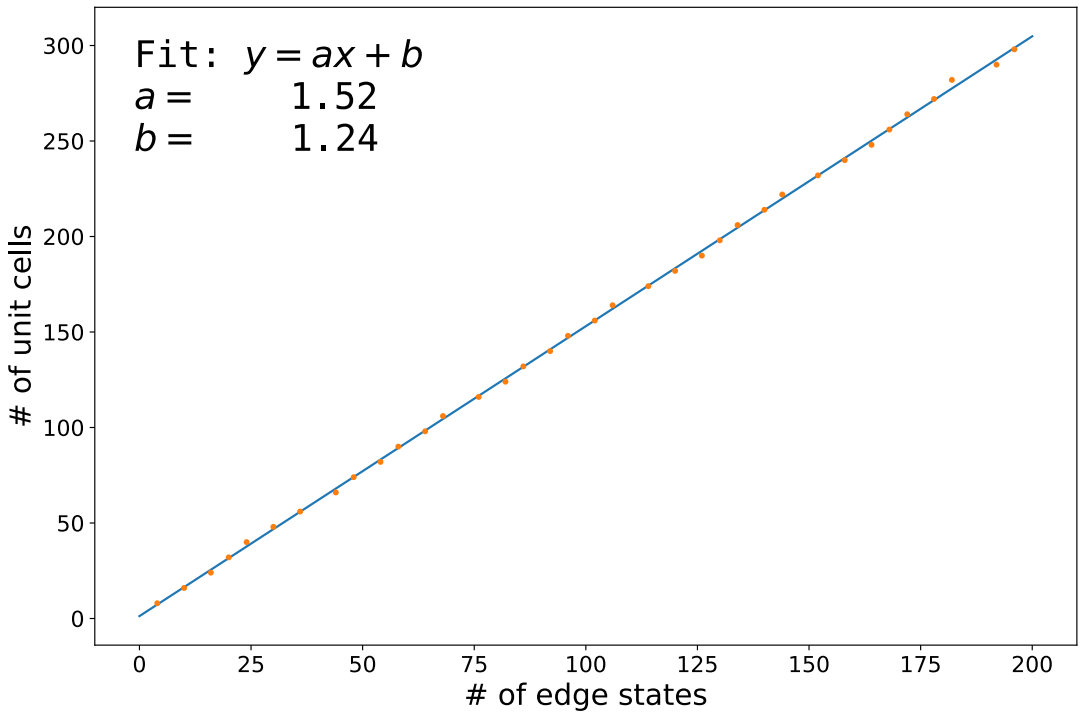

Figure 3.8: Simulating a graphene ribbon with varying length of the zigzag edge. With two zigzag edges there are 1.5 unit cells pr. edge state present in the system. The parameter b is nonzero because the edge states are found by counting zero-energy states, and some graphene ribbons have Dirac points (depending on the length of the zigzag edge) which also contribute to the count. The overcounting is not a problem as we go to sufficiently large ribbons. If all ribbons had Dirac points, b should ideally equal 2 as there is a Dirac point on each sublattice.

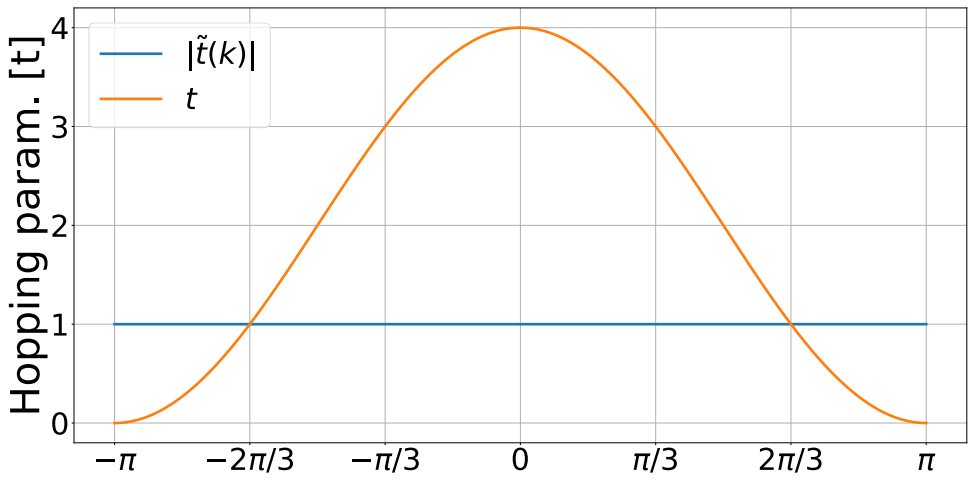

Figure 3.9: Hopping parameters of effective zigzag graphene as a function of the wave number.

each aromatic circle is equally filled by a spin up and spin down electrons. A magnetic edge will due to the Pauli principle minimize the Coulomb repulsion between the unpaired electrons, as having the same spin will forbid them from occupying the same atomic orbital. In fact we can show that in the Hubbard model, these spins will align – this is done in appendix A. What we use is an effective version of the Hubbard model, used in Neoclassical valence bond theory [15]. Since Ref. [15] is unpublished at the time of writing, the important parts are covered in appendix A.

3.3.1 The SSH chain in heuristic model

The heuristic model also gives an intuitive explanation for why the SSH model has an edge state when $t_1 < t_2$ and none when $t_1 \geq t_2$ (see Figure 3.10). In the critical case, $t_1 = t_2$, the double bonds can be placed between every second link, but no link is more stable than any other. Therefore it is not favourable to leave an unpaired electron on the first site. When $t_1 < t_2$ case however, it is more favourable to place the first double bond on the inter-unitcell pair (between sites (j,B) and (j+1,A)), leaving the first electron without a partner. To move into the crystal this electron would have to break up a stronger t_2 bond and replace it with a weaker t_1 bond, which suppresses its propagation into the bulk. The Dirac point of the critical case can in fact be understood as an ambiguity in where to place the bonds. In the bulk, there are two ways of placing the double bonds, which are equally stable, and it is only at the edge that one configuration is preferred over the other.
The Dirac point which is a property of the bulk spectrum of course, can actually be seen as a consequence of this ambiguity. This ambiguity turns out to not only be present in the 1D chain, but is also similarly present in 2D materials. We will touch more upon this point later.

3.4 Conclusion

In this chapter we have introduced the main tools of this thesis. The transfer matrix will be the mathematical formalism that we use to analyse graphene and graphynes, while the heuristic model, the star of the show, will offer predictions and physical intuition. In this chapter, the heuristic model

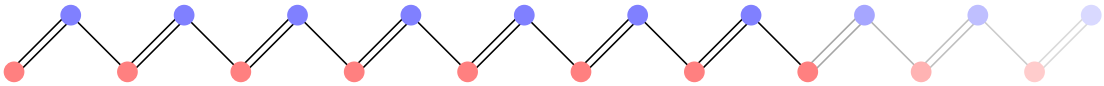

(a) When $t_1 \geq t_2$, the double bonds are placed on the intracell links, leaving no site unpaired and no edge state.

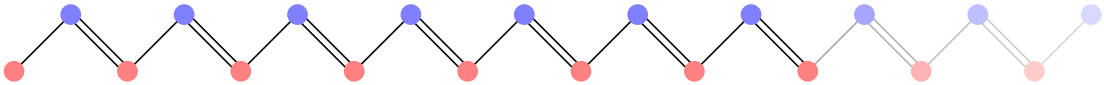

(b) When the $t_1 < t_2$, the double bonds are placed on the intercell links. This leaves the first site unpaired, and an edge state is present.

Figure 3.10: The SSH chain in the heuristic model for $t_1 \geq t_2$ and $t_1 < t_2$.

was used to offer a simple explanation for why the zigzag edge of graphene is magnetic, and we shall see in the following chapters how powerful it is.

Chapter 4

Graphene nanoribbons

Graphene nanoribbons (GNRs) are finite sized graphene ribbons, on length scales of 10^{-8} m. They exist with a variety of edge terminations, heights and can be characterised by their spatial symmetries. In this chapter we concern ourselves with armchair-edge GNRs (AGNRs) which refers to the edge which we consider semi-infinite. We discuss three different edge terminations, which we label zigzag, zigzag' and bearded (see Figure 4.1). AGNRs can be classified according to their topology [2] which is characterised by a binary invariant $Z_2 = 0, 1$. The invariant is given by an integral of the Berry connection over the 1D Brillouin zone [11]. If an AGNR has $Z_2 = 0$ it is said to be topologically trivial, and if $Z_2 = 1$ it is said to be topologically nontrivial. In this chapter we attempt to reformulate the topological classification in the language of the heuristic model and edge states, developed in the previous chapter. We start by introducing the tight-binding Hamiltonian and consider the conditions that give rise to a zero-energy Dirac point in the spectrum.

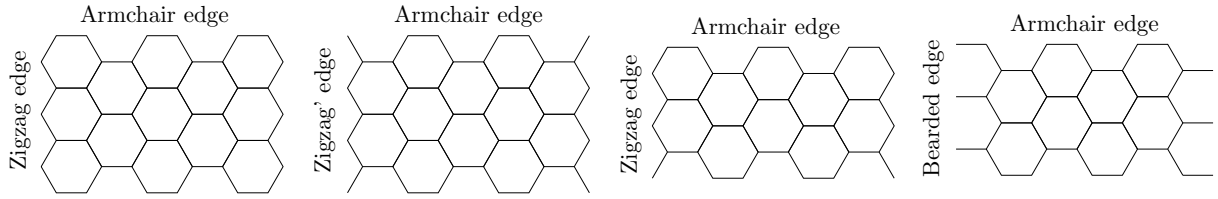

Figure 4.1: The four different AGNRs we will be analyzing in this chapter. From left to right, they are labelled zigzag (with an odd number of rows), zigzag' (with an odd number of rows), zigzag (with an even number of rows), and bearded (with an even number of rows). To see how the rows are numbered, see Figure 4.2. In a shorthand notation, we will sometimes refer to an AGNR with n rows as nAGNR.

4.1 Dirac points in AGNRs

Like in pristine graphene, the lattice of any AGNR can be divided into two sublattices. The nearest neighbour tight-binding Hamiltonian can then be seen as a product between a sublattice-operator that flips the sublattice component of a state, and a real space component that moves the state within a given sublattice. In matrix form the Hamiltonian can be written as a Kronecker product

$$h = \begin{pmatrix} 0 & 1 \\ 0 & 0 \end{pmatrix} \otimes h_B + \begin{pmatrix} 0 & 0 \\ 1 & 0 \end{pmatrix} \otimes h_R = \frac{1}{2} \left[\sigma_1 \otimes (h_B + h_R) + \sigma_2 \otimes (i h_B - i h_R) \right], \tag{4.1.1}$$

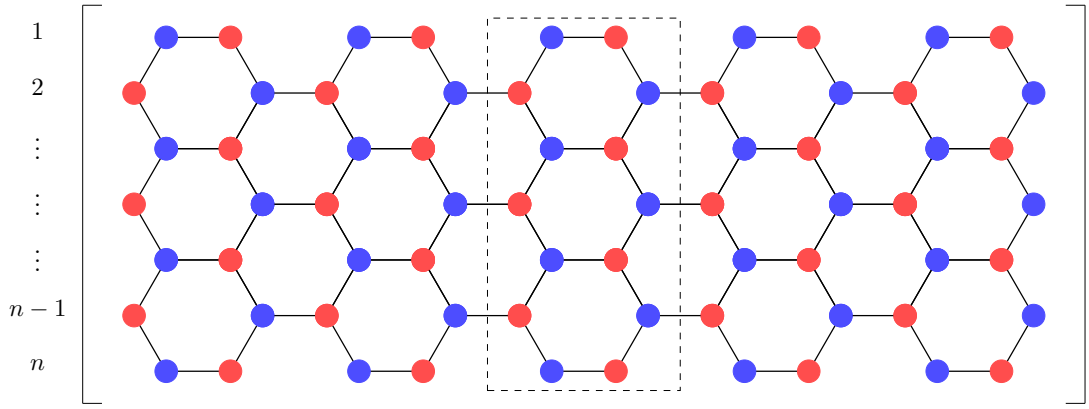

Figure 4.2: A zigzag AGNR with n rows, where n is odd.

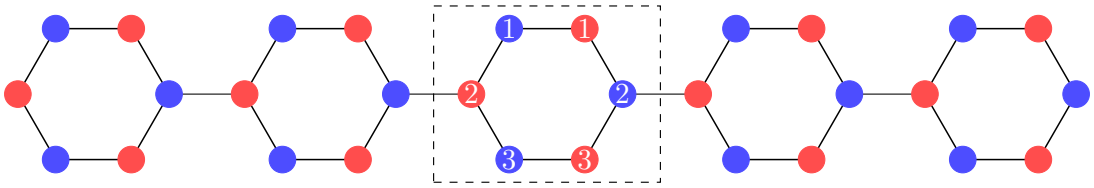

Figure 4.3: Zigzag 3AGNR. This AGNR does not have a Dirac point.

where h_B and h_R act on the blue and red sublattice (see Figure 4.2). For h to be hermitian, $h_B = h_R^\dagger$ must hold. The localised orbitals on the blue and red sublattice are then $|i, j; \downarrow\rangle$ and $|i, j; \uparrow\rangle$, respectively. For small AGNRs, we can analytically show if a Dirac point exists, by analysing the sublattice component of the Hamiltonian. As Dirac points are (in the absence of onsite terms) zero-energy points in the spectrum, they are due to chiral symmetry sublattice polarised, i.e. localised entirely to one sublattice [1]. This is incredibly important and we will repeatedly make use of this fact. The fact that a state is sublattice polarised means that the sublattice on which the state does not exist, yields expressions about the nonzero amplitudes. In the present context, it means that we can look for zero-energy eigenvalues of the $n \times n$ matrix, $h_{B/R}$, instead of the full $2n \times 2n$ matrix (n is the number of rows of the AGNR and the number of sites of each sublattice in the unit cell). We take zigzag 3AGNR (Figure 4.3) as one of two examples. As the eigenvalues are found by solving the characteristic equation $\det(h_B - E\mathbb{1}) = 0$, a zero-energy eigenvalue ensures $\det(h_B) = 0$. We write the matrix in the basis given in Figure 4.3:

$$h_B = -t \begin{pmatrix} 1 & 1 & 0 \\ 1 & \mathrm{e}^{ik} & 1 \\ 0 & 1 & 1 \end{pmatrix}. \tag{4.1.2}$$

As $\det(h_B) = -t\left(\mathrm{e}^{ik} - 2\right)$ which is never zero for $k \in \mathbb{R}$, there is no Dirac point in 3AGNR. For 5AGNR (Figure 4.4) however

[1] See Ref. [16] for an elegant proof.

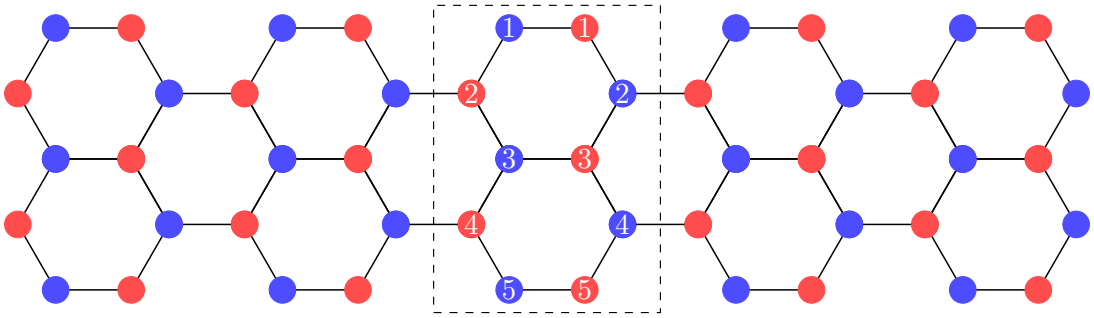

Figure 4.4: Zigzag 5AGNR. This AGNR does have a Dirac point.

$$h_B = -t \begin{pmatrix} 1 & 1 & 0 & 0 & 0 \\ 1 & \mathrm{e}^{ik} & 1 & 0 & 0 \\ 0 & 1 & 1 & 1 & 0 \\ 0 & 0 & 1 & \mathrm{e}^{ik} & 1 \\ 0 & 0 & 0 & 1 & 1 \end{pmatrix} \tag{4.1.3}$$

$$\det(h_B) = -t\left(3 - 4\mathrm{e}^{ik} + \mathrm{e}^{2ik}\right) = 0 \quad \Leftrightarrow \quad k = 0, \tag{4.1.4}$$

meaning that there is a Dirac point at $k = 0$. If the Dirac point is localised to the blue sublattice, it means that for a given red site, the neighbouring blue sites' amplitudes must interfere destructively. The amplitude on each blue site c_i is then found by solving the equations

$$\begin{aligned} c_1 + c_2 &= 0, \\ c_1 + c_2 + c_3 &= 0, \\ c_2 + c_3 + c_4 &= 0, \\ c_3 + c_4 + c_5 &= 0, \\ c_4 + c_5 &= 0. \end{aligned} \tag{4.1.5}$$

As $h_R(k = 0) = h_B(k = 0)$, there is an equivalent Dirac point on the red sublattice. Solving (4.1.5), the eigenstates are found to be

$$\left|\psi_{B/R}\right\rangle = |\downarrow / \uparrow\rangle \otimes |\varphi\rangle \doteq |\downarrow / \uparrow\rangle \otimes \frac{1}{2} \begin{pmatrix} 1 \\ -1 \\ 0 \\ 1 \\ -1 \end{pmatrix}. \tag{4.1.6}$$

Here $\doteq$ means that the ket state is represented as a column vector. As the two states are degenerate, any superposition $|\psi\rangle = \alpha\,|\psi_B\rangle + \beta\,|\psi_R\rangle$ is also an eigenstate of $h_B(k = 0)$. Expanding (4.1.3) to first order in k, the Hamiltonian (4.1.1) becomes

$$h = -t\left[\sigma_1 \otimes \begin{pmatrix} 1 & 1 & 0 & 0 & 0 \\ 1 & 1 & 1 & 0 & 0 \\ 0 & 1 & 1 & 1 & 0 \\ 0 & 0 & 1 & 1 & 1 \\ 0 & 0 & 0 & 1 & 1 \end{pmatrix} + \sigma_2 \otimes \begin{pmatrix} 0 & 0 & 0 & 0 & 0 \\ 0 & k & 0 & 0 & 0 \\ 0 & 0 & 0 & 0 & 0 \\ 0 & 0 & 0 & k & 0 \\ 0 & 0 & 0 & 0 & 0 \end{pmatrix}\right] \tag{4.1.7}$$

of which $|\psi\rangle$ is an eigenstate:

$$\begin{aligned}\langle\varphi|\, h\, |\psi\rangle = -t\sigma_2 \left(\alpha \langle\varphi|\, h^{(1)}\, |\varphi\rangle\, |\downarrow\rangle + \beta \langle\varphi|\, h^{(1)}\, |\varphi\rangle\, |\uparrow\rangle\right) = t\left(i\alpha \langle\varphi|\, h^{(1)}\, |\varphi\rangle\, |\uparrow\rangle - i\beta \langle\varphi|\, h^{(1)}\, |\varphi\rangle\, |\downarrow\rangle\right) \\ = \langle\varphi|\, E\, |\psi\rangle\,.\end{aligned} \tag{4.1.8}$$

$\langle\varphi|\, h^{(1)}\, |\varphi\rangle = k/2$, so the above yields two equations

$$-i\beta\frac{tk}{2} = \alpha E, \tag{4.1.9a}$$

$$i\alpha\frac{tk}{2} = \beta E, \tag{4.1.9b}$$

which can be compacted into the matrix equation

$$\frac{tk}{2}\begin{pmatrix} 0 & i \\ -i & 0 \end{pmatrix}\begin{pmatrix}\alpha \\ \beta\end{pmatrix} = E\begin{pmatrix}\alpha \\ \beta\end{pmatrix} \quad \Rightarrow \quad E = \pm\frac{tk}{2}, \tag{4.1.10}$$

confirming that the energy is linear around $k = 0$.
Having analysed the first two odd-numbered zigzag AGNRs and shown whether or not they have a Dirac point, let us look at the general case. We take an odd-numbered zigzag AGNR and assume that if there is a Dirac point, it lies at $k = 0$. Like in (4.1.5), the amplitudes of either sublattice would have to satisfy the following set of equations:

$$\begin{aligned} c_1 + c_2 &= 0, \\ c_1 + c_2 + c_3 &= 0, \\ c_2 + c_3 + c_4 &= 0, \\ &\vdots \\ c_{N-3} + c_{N-2} + c_{N-1} &= 0, \\ c_{N-2} + c_{N-1} + c_N &= 0, \\ c_{N-1} + c_N &= 0. \end{aligned} \tag{4.1.11}$$

This set of equations yields two edge conditions, namely the first equation and the last equation. Setting $c_1 = 1$ (up to a normalisation factor), the equations can be solved iteratively. We end up with a state, whose real space component is given by

$$|\varphi\rangle \doteq R \begin{pmatrix} 1 \\ -1 \\ 0 \\ 1 \\ -1 \\ \vdots \\ 0 \\ 1 \\ -1 \\ \vdots \end{pmatrix} \tag{4.1.12}$$

for some normalisation factor R. In the bulk each site's amplitude is the negative sum of the previous two sites', giving a repeating sequence of $1, -1, 0$. As it is repeating, the sequence can be terminated in one of three ways, $(c_{N-2}, c_{N-1}, c_N) = (0, 1, -1)$, $(c_{N-2}, c_{N-1}, c_N) = (-1, 0, 1)$, and $(c_{N-2}, c_{N-1}, c_N) = (-1, 1, 0)$. Of these, only the first satisfies the second edge condition, and only the first obeys mirror symmetry, as each site should have the same probability amplitude (up to a phase) as its mirror-symmetric partner. Therefore every third odd-numbered AGNR has a $k = 0$ Dirac point. As 5AGNR has one, there are Dirac points at $n = 5, 11, 17, 23, \cdots = 6m + 5, m \in \mathbb{N}_0$. This can be seen by simply calculating the band structure of AGNRs which is a straightforward matter as the Hamiltonian for a given nanoribbon has a very general form. The band structure of AGNRs with $n = 3, 5, 7, 9$ rows can be seen in appendix B. It can also be shown analytically which we do in section 4.2.

4.1.1 Dirac points in heuristic model

The heuristic model introduced in the previous chapter which served as an intuitive way of predicting edge states in graphene, can also be used to predict the existence of Dirac points in AGNRs in a physically meaningful way. The idea is to fill the AGNR with as many aromatic circles as possible, and if there is a leftover chain of atoms there is a Dirac point. The reasoning is that the circles represent the low- and high-energy part of the spectrum, and the chain which, dealt with individually, has a zero-energy Dirac point, connecting the high and low energy parts of the spectrum. The aromatic rings are placed in rows parallel to the armchair edge, and can be associated with a row number – i.e. the chain of aromatic rings in the top the zigzag AGNR of Figure 4.5 can be associated with row number 2. Maximizing the number of aromatic rings means putting a chain of rings associated with every third row number, i.e. starting from the top would put chains of aromatic rings in rows $2, 5, 8, \ldots, n-1$. Putting a chain of rings in row number $n-1$ serves as the boundary condition for the nanoribbon. A way of classifying an AGNR with n rows is to use the modular arithmetic equivalence class:

- if $n - 1 \equiv_3 2 \Rightarrow n \equiv_3 0$: the entire ribbon is filled with rings and there is no leftover row at the bottom.
- $n \equiv_3 1$: the entire ribbon is filled with rings and there is one row of atoms with leftover bonds. These lone bonds can be filled with double bonds.
- $n \equiv_3 2$: the entire ribbon is filled with rings and there are two rows of leftover atoms. These two rows are responsible for the Dirac point.

where $n \equiv_3 x$ means $n = x \pmod 3$. The three scenarios are shown in Figure 4.5 on four different zigzag AGNRs. The condition of $n \equiv_3 2$ for a Dirac point to exist predicts AGNRs with $n = 5, 8, 11, \ldots = 2 + 3m$ rows ($m \in \mathbb{N}$) to have Dirac points. This is in line with what we found in the analytical calculation above, but there we only looked at odd n (the termination and unit cell both change when n is even in a zigzag AGNR). As this is a bulk property, it is true for zigzag, zigzag' and bearded AGNRs alike, as the band structure is independent of the unit cell.

4.2 Edge states in AGNRs

In this section we utilize two methods of determining whether a given AGNR hosts edge states – the heuristic model introduced in chapter 3, and an analytical model. Building on the results of the previous section, we will obtain a theoretical prediction of whether or not a nanoribbon has a Dirac point and how many edge states it has. In the SSH model, we saw that these two quantities marked the topologically trivial, the critical and topologically nontrivial phase. In the topologically trivial phase, there was no edge state and no Zak phase, in the critical phase there was a Dirac point, but no edge state, and the Zak phase was ill-defined, and the nontrivial phase was characterised by an edge state and a Zak phase $\gamma = \pi$. Our approach in this section will be to transform the Hamiltonian of a given AGNR into a set of connected one-dimensional chains. These chains can be decoupled into separate chains, which will give a prediction of the phase of the AGNR. The chains can be analysed individually, and the contribution from each to the total Zak phase can simply be summed. The procedure is similar to the one used on zigzag graphene in chapter 3 (which with translational invariance in one-direction could immediately be written as a 1D chain) where for a given unit cell, we take the sites whose nearest neighbours are all part of the same unit cell, and project them out. As the simplest possible example, we take 3AGNR with a zigzag termination. The unit cell is given in Figure 4.3. Once again we introduce P and Q, which project into sites sites connected to neighbouring unit cells and sites not connected to neighbouring unit cells, respectively. The sites labelled 1 and 3 in Figure 4.3 have no nearest neighbour sites in the neighbouring unit cells, so these sites belong to the Q subspace, whereas the sites labelled 2 belong to the P subspace. The reduced model is shown in Figure 4.6.
The reduced model is just the SSH model with $t_1 = \tilde{t} = 2t^3/(E^2 - t^2)$ and $t_2 = t$. In the $E = 0$ case, $|t_1| > |t_2|$, indicating a gapped spectrum with no edge states and no Zak phase. This is as expected from the spectrum given in appendix B, and the heuristic model does not predict any edge states (see Figure 4.5). As mentioned the general case nAGNR will reduce to a set of coupled chains, as we show in the following section.

4.2.1 Reduced AGNR model and zigzag ($n =$ Odd) edge states

In this section we introduce a reduced model for the AGNR lattice, with the zigzag termination as the first example. As the unit cell of the zigzag termination is different for an odd and even number of rows, we start by considering n odd. For a given n, the AGNR will be reduced to a η coupled chains, which depends on the termination:

- zigzag ($n =$ Odd) reduces to $\eta = \frac{n-1}{2}$ coupled chains
- zigzag ($n =$ Even) reduces to $\eta = \frac{n}{2}$ coupled chains
- zigzag' ($n =$ Odd) reduces to $\eta = \frac{n+1}{2}$ coupled chains
- bearded ($n =$ Even) reduces to $\eta = \frac{n}{2}$ coupled chains

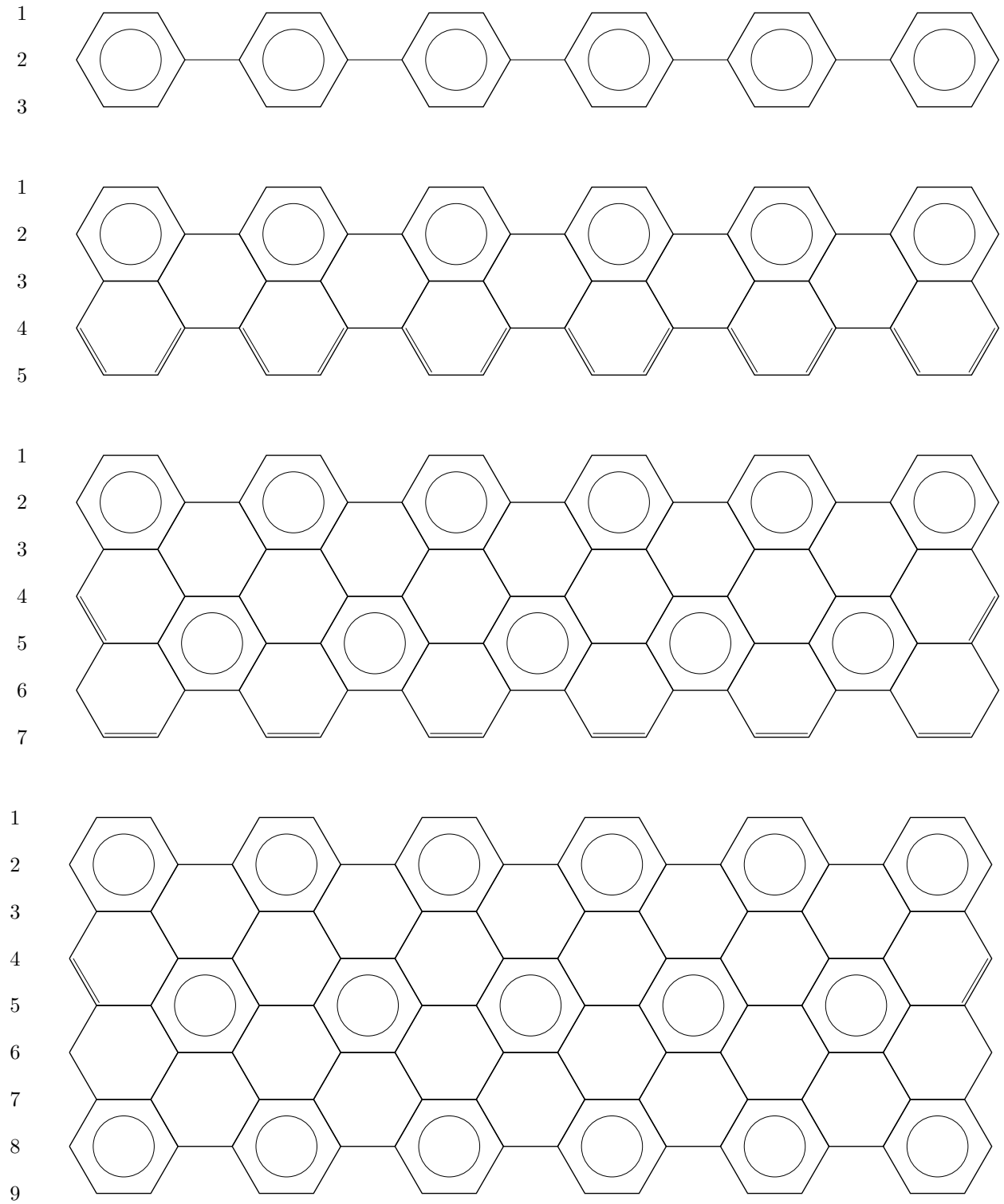

Figure 4.5: Four different zigzag AGNRs with the number of rows $n \equiv_3 0, 2, 1, 0$, respectively. $n \equiv_3 2$ correctly predicts a Dirac point, whereas the others do not have one. Notice how the bonds at the bottom are placed in 5AGNR, the $n \equiv_3 2$ case. In the bulk, each bond might just as well have been shifted one pair over, but due to the edge, the configuration chosen is the right one. We will refer to the leftover chain responsible for the Dirac point, as a *Dirac chain*.

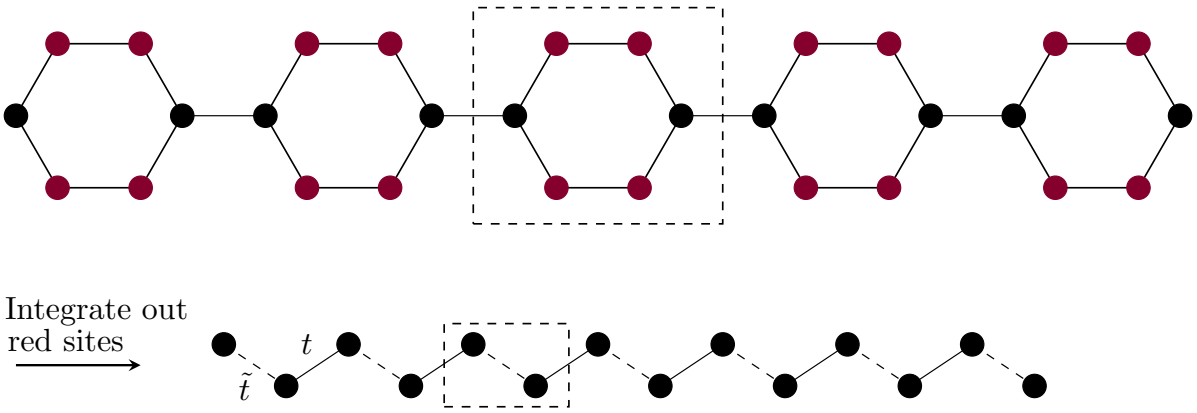

Figure 4.6: By integrating out the Q sites (red) of an AGNR we can reduce it to a one-dimensional chain, or a set of one-dimensional chains, with different hopping amplitudes, $\tilde{t}(E)$ and t.

The reduced model (Figure 4.7b) is a rectangular lattice with effective hopping parameters that depend on the parameters of the Hamiltonian. We derive the hopping parameters $\tilde{t}$ and t^* and the onsite energy ε from Figure 4.7b. We show the expressions for the hopping parameters by applying the effective Hamiltonian H_P to just one site of a given nAGNR (Figure 4.7a) as an example. As a reminder, the effective Hamiltonian on the P subspace is

$$H_P = PHP + PHQ\frac{1}{E - QHQ}QHP \tag{4.2.1}$$

The first term is just the hopping between nearest neighbour P sites, while the second is a little more involved. First QHP brings the P state into the Q subspace with a factor of $(-t)$. Thereafter $1/(E - QHQ)$ will either move it on to the neighbouring Q state with a factor of $(-t)/(E^2 - t^2)$ (the denominator, which comes from the inversion, is the determinant of the $E - QHQ$ matrix), or it will return the same Q state with a factor of $E/(E^2 - t^2)$. The last term will then bring the Q state back to one of its neighbouring P states. We label the states $|m, i, j\rangle$, where m refers to the chain, $i = 1, 2$ refers to the horizontal index inside the unit cell (and also distinguishes between the two sublattices), and j dictates the unit cell. Following the reasoning above, we can deduce

$$\begin{aligned} H_P\,|m,i,j\rangle = 2\varepsilon\,|m,i,j\rangle - t\left(\delta_{i,1}\,|m,2,j-1\rangle + \delta_{i,2}\,|m,1,j+1\rangle\right) - 2\tilde{t}\sigma^x_{ii'}\,\big|m,j,i'\big\rangle - \\ \tilde{t}\sigma^x_{ii'}\left(\big|m+1,i',j\big\rangle + \big|m-1,i',j\big\rangle\right) - 2t^*\left(|m+1,i,j\rangle + |m-1,i,j\rangle\right), \end{aligned} \tag{4.2.2}$$

where summation over repeated indices is implied. The parameters are given as

$$\varepsilon = Et_0(E), \tag{4.2.3a}$$

$$\tilde{t} = tt_0(E), \tag{4.2.3b}$$

$$t^* = -Et_0(E), \tag{4.2.3c}$$

$$t_0(E) = \frac{t^2}{E^2 - t^2}. \tag{4.2.3d}$$

The horizontal internal hop, $2\tilde{t}$ is twice the skewed internal hop $\tilde{t}$, as there are two horizontal paths through the Q subspace, whereas for the skewed hop there is only one path. The factor of 2 in front of the onsite potential ε has the same origin, with there being two ways of entering the Q subspace

and returning to the same P site. This holds for *all* the chains in the reduced zigzag model when the number of rows, n, is odd. For other terminations, the first and last chains may not have the factor of 2.

For small n, it is actually easy to construct the linear combinations that decouple the chains. To show an example, we decouple zigzag 7AGNR in two steps. The procedure is outlined in Figure 4.8. The result is three independent SSH models that can be analysed individually – any feature of an AGNR (Dirac points, edge states, Zak phase) can then be extracted from individually analysing the decoupled chains. The decoupled models have onsite energies $\epsilon = \lambda_i \varepsilon$ and internal hopping elements $t_1 = \lambda_i \tilde{t}$ (there is always a common factor in front of ε and $\tilde{t}$). The factors λ_i will turn out to be crucial for the topological characterisation of an AGNR.

Before dealing further with 7AGNR, we consider the SSH chain with $t_1 = \lambda\tilde{t} = \lambda t^3/(E^2 - t^2)$, $t_2 = t$, and onsite energy $\epsilon = \lambda\varepsilon = \lambda E t^2/(E^2 - t^2)$. When $|t_1| < |t_2|$, the chain hosts edge states with energy equal to the onsite energy, leading to the self consistency equation for E

$$E = \epsilon = \lambda \frac{Et^2}{E^2 - t^2}. \tag{4.2.4}$$

The solutions are $E = 0, \pm\sqrt{\lambda + 1}t$. The non-zero solutions are exactly the values at which $t_1 = t$, which is the critical case. The non-zero solutions do therefore not describe edge states, but can describe Dirac-like points, where two low-energy (high-energy) bands meet at some point in k-space. These are not actual Dirac points, as the bands below and above the points are completely filled (empty). The $E = 0$ solution gives $t_1 = -\lambda t$. The magnitude of λ therefore dictates whether or not an edge state or Dirac point is present. If $|\lambda| > 1$ there is neither an edge state or a Dirac point and the contribution to the Zak phase is zero. If $|\lambda| = 1$ there is a Dirac point and as mentioned, the Zak phase is ill-defined. If $|\lambda| < 1$ there is an edge state, and an associated Zak phase $\gamma = \pi$. For a given AGNR there will be η chains each with potential to host an edge state or carry a Dirac point. Of the three values of λ in the reduced model for 7AGNR (see Figure 4.8), two are greater than 1 and one is smaller than 1, meaning that zigzag 7AGNR has one edge state and a Zak phase of π. This result is in agreement with what we find using the heuristic model (see Figure 4.5).

In general it is not feasible to decouple the set of chains like done in Figure 4.8. In fact a far simpler method that can be generalised to any n, is to just view the set of chains as a tight-binding model with open boundary conditions. It is clear that the onsite potential $\lambda\varepsilon$ and internal hopping $\lambda\tilde{t}$ need not be considered separately, and the coupled chains can in fact be described by a Hamiltonian of the form

$$H = 2\sum_{j=1}^{\eta} |j\rangle\langle j| - \sum_{j=1}^{\eta} \left(|j+1\rangle\langle j| + |j\rangle\langle j+1|\right). \tag{4.2.5}$$

We set out to find the eigenvalues and eigenstates of this Hamiltonian. The first term is the identity and does not change the eigenstates. The last sum contains a term with the state $|\eta + 1\rangle$. To ensure the boundary conditions are satisfied, we demand $|\eta+1\rangle = |0\rangle = 0$. For periodic boundary conditions, the eigenstates are plane waves $|k\rangle = \sum_j \mathrm{e}^{ikj}|j\rangle$, but for open boundary conditions k is not a good quantum number. We choose as an ansatz a linear combination of Bloch waves with opposite momenta that ensures the state goes to zero at $j = 0$:

$$|\kappa\rangle = \frac{-i}{\sqrt{2}}\left(|k\rangle - |-k\rangle\right) = \sqrt{\frac{2}{\eta+1}} \sum_{j=1}^{\eta+1} \sin(kj)\,|j\rangle. \tag{4.2.6}$$

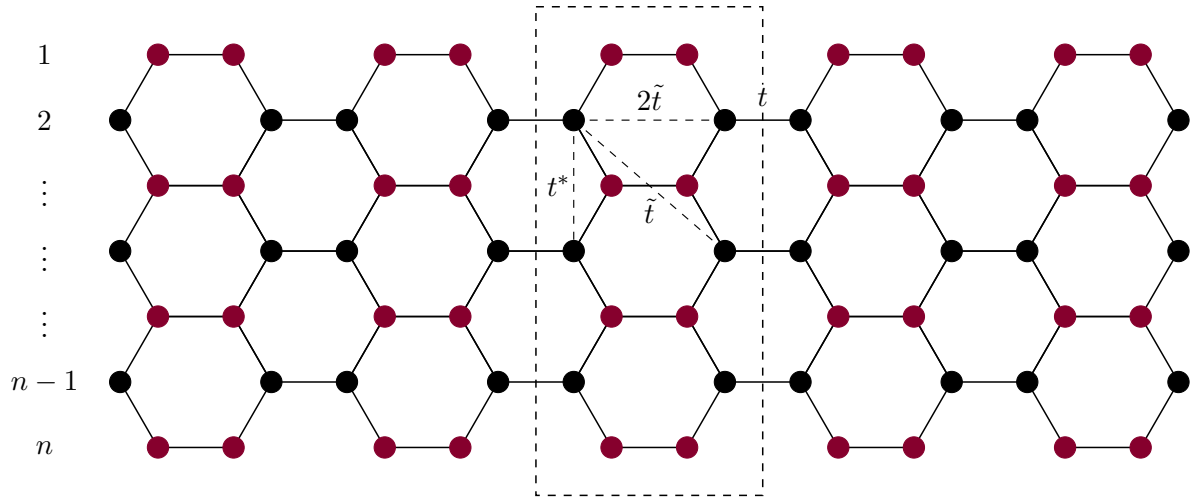

(a) A general zigzag edge AGNR with n rows. The P and Q sites are marked with black and red as in Figure 4.6, and the unit cell is drawn. This lattice reduces to a set of connected chains. The hopping elements of the effective lattice are shown.

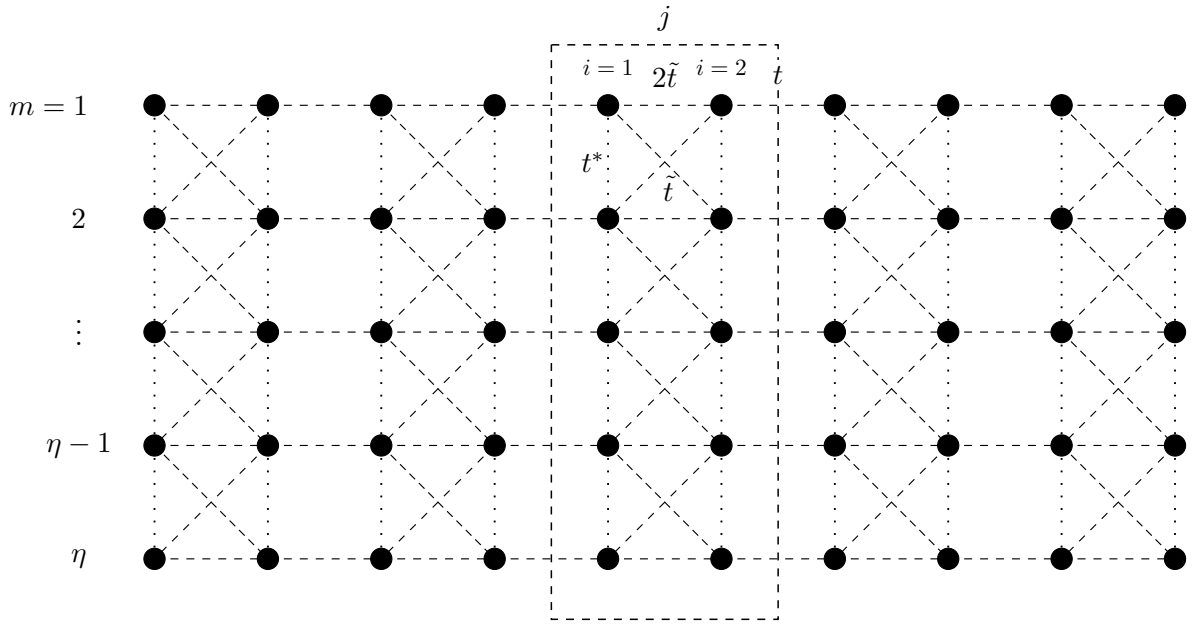

(b) Reduced lattice of a zigzag edge AGNR, which contains four different hopping parameters. There are two horizontal hops, t and $2\tilde{t}$, that are external and internal hops of the unit cell respectively. There is one vertical hop between sites on neighbouring chains, t^*. Finally inside the unit cell, there is a skewed hop between sites on neighbouring chains, $\tilde{t}$. Besides the hopping parameters, there is also an onsite term, 2ε. All parameters of the effective Hamiltonian with the exception of t are dependent on E. The sites are labelled by chain $m = 1, \ldots, \eta$, sublattice $i = 1, 2$, and unit cell j.

Figure 4.7: Original and reduced lattice of a zigzag nAGNR.

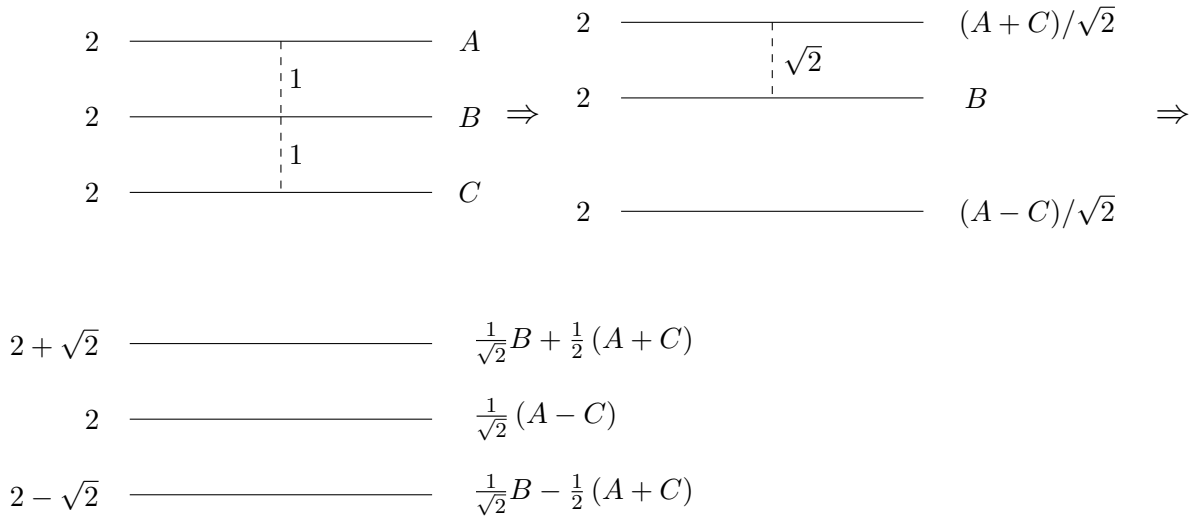

Figure 4.8: Decoupling of zigzag 7AGNR in the reduced model into three independent chains. The number on the left of a chain indicates the factor in front of the internal hopping parameter $\tilde{t}$ and onsite term ε. The number by the dashed line connecting the chains is the factor in front of the external hops, $\tilde{t}$ and t^*. The letters on the right label the chains and their superpositions.

To satisfy the second condition, k must be quantized $k(\eta+1) = m\pi \Rightarrow k = \mu\pi/(\eta+1), \mu \in [1, \ldots, \eta]$. The bulk eigenvalues are the same as for periodic boundary conditions

$$\lambda = 2 - 2\cos(k). \tag{4.2.7}$$

There are two especially interesting eigenvalues, $\lambda = 1$ or $\lambda < 1$. The first is equivalent to $\cos(k) = 1/2$. This happens at

$$k = \frac{\pi}{3} \quad \Rightarrow \quad \frac{\mu\pi}{\eta+1} = \frac{\pi}{3} \quad \Rightarrow \quad n = 6\mu - 1, \tag{4.2.8}$$

which is just the subset of $\{n \in \mathbb{N} | n \equiv_3 2\}$ consisting of odd numbers. As $0 < k < \pi$, there is only one Dirac point (and not another at $k = 5\pi/3$). This is, once again, in line with what we have found above for Dirac points in AGNRs, lending more credence to the heuristic model. The number of edge states is dictated by the number of eigenvalues smaller than 1. This is true when $\cos(k) > 1/2 \Rightarrow k < \pi/3$. The number of edge states is then the number of integers $\mu > 0$ that satisfy

$$\frac{\mu\pi}{\eta+1} < \frac{\pi}{3} \quad \Rightarrow \quad \mu < \frac{\eta+1}{3} = \frac{n+1}{6}. \tag{4.2.9}$$

The number of positive integers that satisfy the inequality is given by $\lfloor \frac{n}{6} \rfloor$, where $\lfloor x \rfloor$ is the floor function, giving the largest integer smaller than or equal to x. A way of looking at this result is that for every third row of benzene rings (alternatively, every sixth row of atoms) one more edge state appears, since of course $\lfloor \frac{n+6}{6} \rfloor = 1 + \lfloor \frac{n}{6} \rfloor$. This is also in line with the edge state density we found in zigzag graphene with translational invariance, in chapter 3.

4.2.2 Zigzag ($n =$ Even) termination

The unit cell of an AGNR with a zigzag termination changes if the number of rows is even. The lattice and unit cell are both shown in Figure 4.9.

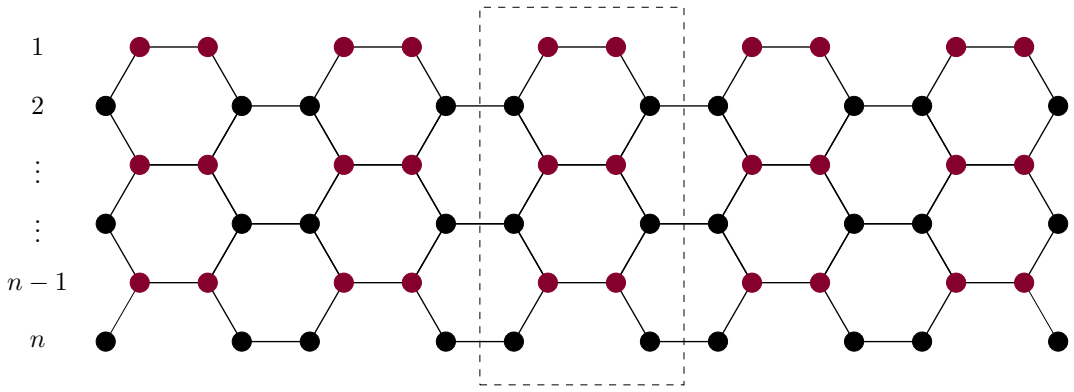

Figure 4.9: Zigzag AGNR with $n =$ Even rows, with P and Q sites marked black and red respectively. Q sites are projected out to reach an effective model like above.

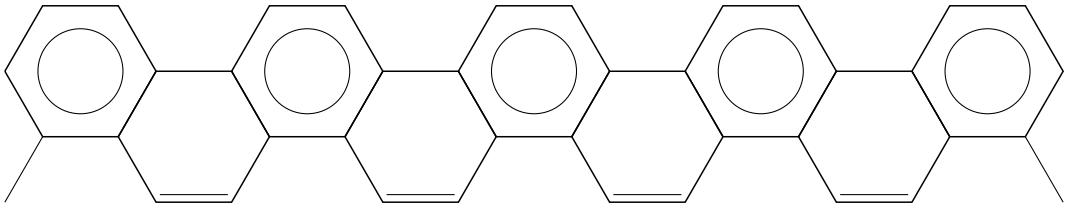

Figure 4.10: Smallest possible zigzag AGNR with an even number of rows. The heuristic model predicts one edge state, which with knowledge of zigzag AGNRs with odd numbered rows can be used to predict the total number of edge states for a given even n.

In terms of the heuristic model, the key difference is a dangling π bond at each end. In the above section we saw that adding three rows of benzene rings (six rows of atoms) to the zigzag AGNR means that there is one more edge state. The same heuristic analysis can be applied here, since adding six rows of atoms looks the same whether the number of rows, n, is even or odd. We therefore only need to see how many edge states the smallest possible AGNR has, and we then know that new edge states should appear at the same frequency. According to the heuristic model, the smallest AGNR ($n = 4$) has one edge state (see Figure 4.10). The total number of edge states is then according to the heuristic model $\lfloor \frac{n+2}{6} \rfloor$.
We prove this mathematically by using the same approach as above. By integrating out all the sites that have no nearest neighbours in different unit cells, we are left with a reduced lattice similar to the one above. The difference is the bottom chain has a different internal hopping parameter ($\tilde{t}$ instead of $\tilde{2t}$) and the onsite potential is similarly different. The effective 1D model that we are left to solve is then described by the Hamiltonian

$$H = 2\sum_{j=1}^{\eta} |j\rangle\langle j| - \sum_{j=1}^{\eta} (|j+1\rangle\langle j| + |j\rangle\langle j+1|) - |\eta\rangle\langle\eta| \doteq \begin{pmatrix} 2 & 1 & & & 0 \\ 1 & 2 & 1 & & 0 \\ & 1 & \ddots & \ddots & \\ & & \ddots & \ddots & 1 \\ 0 & & & 1 & 1 \end{pmatrix}. \tag{4.2.10}$$

We start by making the (perhaps obvious) observation that the tight-binding Hamiltonian is just the discrete Laplacian operator, the eigenvalues and eigenvectors of which are well known for different

boundary conditions. As opposed to the open boundary conditions in the previous section (also known as Dirichlet boundary conditions), what we have here is known as mixed Dirichlet-Neumann boundary conditions to the Laplacian. The eigenvalues are

$$\lambda = 4\sin^2\left(\frac{\pi\left(\mu-\frac{1}{2}\right)}{2\eta+1}\right),\ \mu = 1,\dots,\eta. \tag{4.2.11}$$

See appendix C for a proof. The number of eigenvalues smaller than 1 is the number of integers greater than 0 that satisfy

$$\frac{\pi\left(\mu-\frac{1}{2}\right)}{2\eta+1} < \frac{\pi}{6} \quad \Rightarrow \quad \mu < \frac{n+4}{6}, \tag{4.2.12}$$

which is given by $\lfloor\frac{n+2}{6}\rfloor$, confirming the prediction of the heuristic model. A Dirac point is possible when the last inequality becomes an equality, with m satisfying

$$\mu = \frac{n+4}{6} \quad \Rightarrow \quad n = 6\mu - 4 = 6\mu' + 2, \tag{4.2.13}$$

which holds for $n = 8, 14, 20, \dots$. This is just the even numbers contained in the set $\{n \in \mathbb{N} | n \equiv_3 2\}$, once again confirming what our heuristic model predicted.

4.2.3 Zigzag' (n = Odd) termination

We now consider a ribbon with a zigzag' termination, which is only well defined for an odd number of rows. It is characterised by having a dangling π bond at the top and at the bottom of the zigzag edge (see Figure 4.11). In the above sections we argued that adding 6 rows of atoms meant adding one edge state to the system. As the dangling bonds are unaltered after adding more rows to the zigzag' AGNR, this still holds. To make a prediction of the number of edge states in the system from the heuristic model, we therefore only need to check how many edge states the smallest AGNRs support. From Figure 4.12, we see that the heuristic model predicts one edge state for $n = 3$ and $n = 5$, and two for $n = 7$. This is one more than for the zigzag termination, and enough to make a general prediction. The number of edge states for n rows is $\lfloor\frac{n+6}{6}\rfloor = \lfloor\frac{n}{6}\rfloor + 1$.
After integrating the red sites out of the zigzag' lattice, we are left with a model described by the Hamiltonian

$$H = 2\sum_{j=1}^{\eta}|j\rangle\langle j| + \sum_{j=1}^{\eta}\left(|j+1\rangle\langle j| + |j\rangle\langle j+1|\right) - |1\rangle\langle 1| - |\eta\rangle\langle\eta| \doteq \begin{pmatrix} 1 & 1 & & & 0 \\ 1 & 2 & 1 & & 0 \\ & 1 & \ddots & \ddots & \\ & & \ddots & 2 & 1 \\ 0 & & & 1 & 1 \end{pmatrix}. \tag{4.2.14}$$

The eigenvalues are given by

$$\lambda_\mu = 2 - 2\cos\left(\frac{\mu\pi}{\eta+1}\right),\ \mu = 0,\dots\eta-1. \tag{4.2.15}$$

The proof of this is also given in C. We see that the eigenvalues are identical to the zigzag case, but with μ being allowed to assume the value $\mu = 0$, in which case $\lambda_{\mu=0} = 0$. This means that in a zigzag'

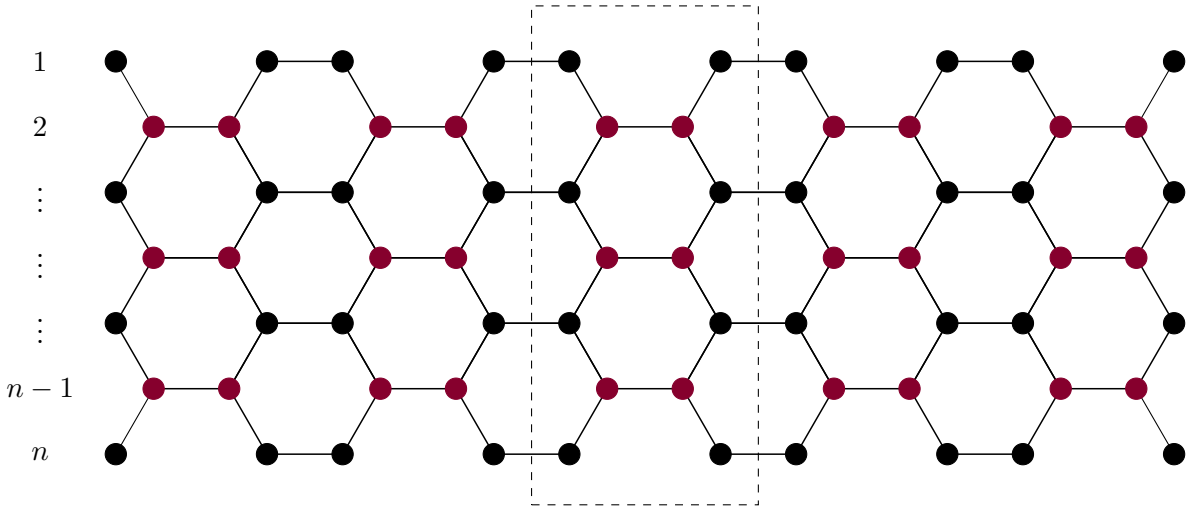

Figure 4.11: AGNR with n rows with a zigzag' termination. The red sites are projected out to give the effective model described in (4.2.14).

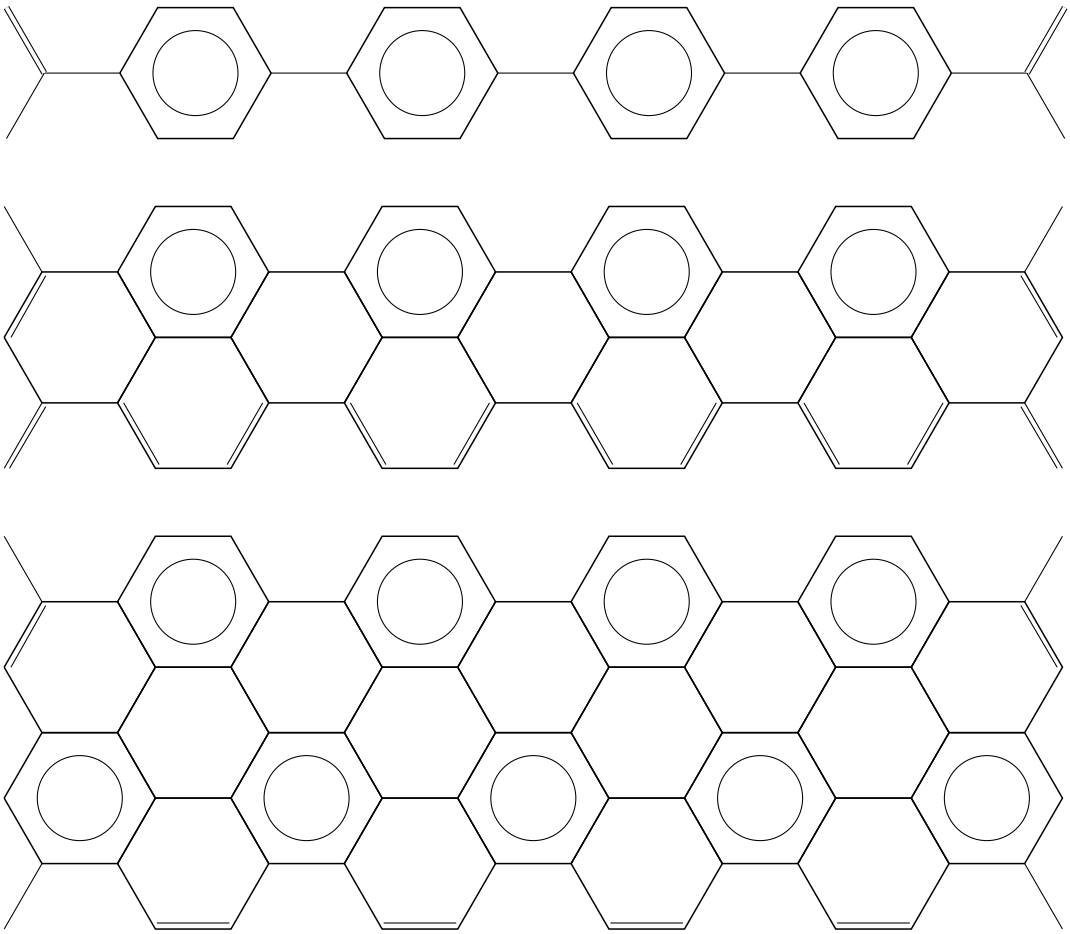

Figure 4.12: Three smallest zigzag' AGNRs, with 3, 5, and 7 rows. The ones with $n = 3$ and $n = 5$ rows have one edge state at each end, whereas the one with $n = 7$ rows has two.

nAGNR, there is always one more edge state than in the corresponding zigzag AGNR, $\lfloor \frac{n}{6} \rfloor + 1$, in agreement with the heuristic model.
Since λ is actually the decay factor of the edge state, a $\lambda = 0$ eigenvalue corresponds to an eigenstate entirely localised to the first unit cell. This can also be explained in the heuristic model. In Figure 4.12, there is an unpaired site on one of the outermost dangling π bonds, and in order for it to propagate into the bulk it must break up an aromatic circle.

4.2.4 Bearded AGNRs

The last armchair edged nanoribbon that we will be studying is the one with a so called bearded termination (Figure 4.13a). The bearded termination has an even number of rows, n and is characterised by $n/2$ dangling π bonds at each end of the ribbon. This termination is very different to the ones discussed above. In the zigzag and zigzag' terminations, our heuristic analysis of zigzag graphene from chapter 3 predicted that for every sixth row added to the ribbon, a new edge state would emerge. This analysis is not valid for the bearded termination, and in order to make a prediction of the number of edge states in a given bearded AGNR, we first need to know the edge state density. The heuristic model predicts two unpaired electrons on every three sites, see Figure 4.14.
From Figure 4.13 we see a bearded AGNR can also be reduced to a set of connected chains (Figure 4.13b), but in a significantly more muddled way, making the approach we took above harder to use. In fact there is no obvious way of decoupling them as we have done, even for the smallest possible ribbon, 4AGNR. This forces us to use another method in order to find the edge states.
Fortunately there is another way to predict the edge states in the system, and the Dirac points are known from the $n =$ Even zigzag AGNRs (because Dirac points is a bulk property and independent of termination). The procedure is to once again assume that any potential edge states in the system have zero energy and are sublattice polarised. From this we can construct a transfer matrix for zero-energy states, which we show by a few examples in appendix D to have the form $T_{ij} = \min(i, j)\,(-1)^{i+j}$. In fact, this way of deriving a general transfer matrix can also be done for the zigzag and zigzag' AGNRs, and this gives matrices that take the forms of (4.2.5), (4.2.10), and (4.2.14). We also show this in appendix D. It is not feasible to find the eigenvalues of the bearded transfer matrix, and we need to use another method of finding the number of edge states in a given bearded AGNR.
In chapter 3 we showed that with translational invariance the zigzag edge of graphene hosts edge states in every third unit cell. In section 4.2.1 we showed that this was also the case in the discrete case. We can therefore find the number of edge states in a given bearded AGNR by considering graphene with a bearded termination, with translational invariance along the bearded edge. Like in chapter 3 we should be able to calculate the density of edge states in graphene with a bearded termination by reducing the problem to an effective SSH model. We start by considering the unit cell of graphene with a bearded termination along the x-direction, see Figure 4.14.
Like in chapter 3, we can construct an effective hopping from site 1 to 4 by integrating out the sites that are not connected to neighbouring unit cells, $j \pm 1$. This effective hopping $\tilde{t}$ can be found by using the Hamiltonian of the form (4.2.1) on a state $|1; k_x, j\rangle$

$$H_P|1; k_x, j\rangle = -t|4; k_x, j-1\rangle - QHP\frac{1}{E - QHQ}|2; k_x, j\rangle. \tag{4.2.16}$$

The operator $E - QHQ$ can be inverted by writing $E - QHQ$ in matrix form with the Q states forming

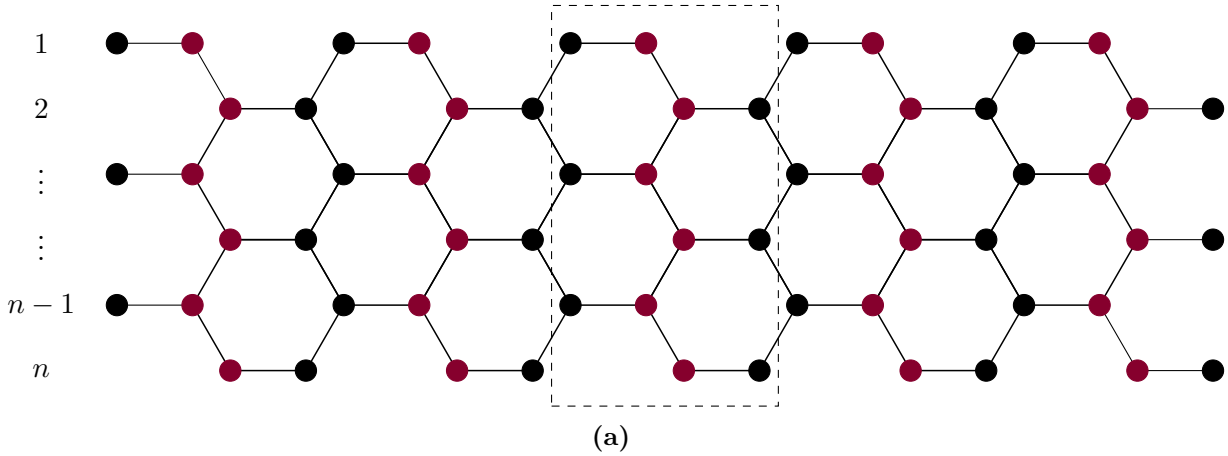

(a)

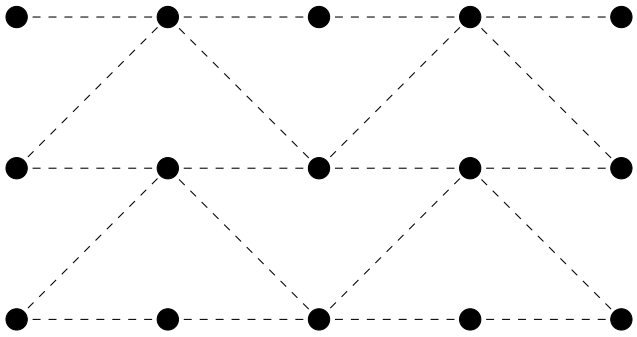

(b)

Figure 4.13: AGNR with n rows with a bearded termination, and the reduced model. The reduced model looks significantly different to the ones encountered above.

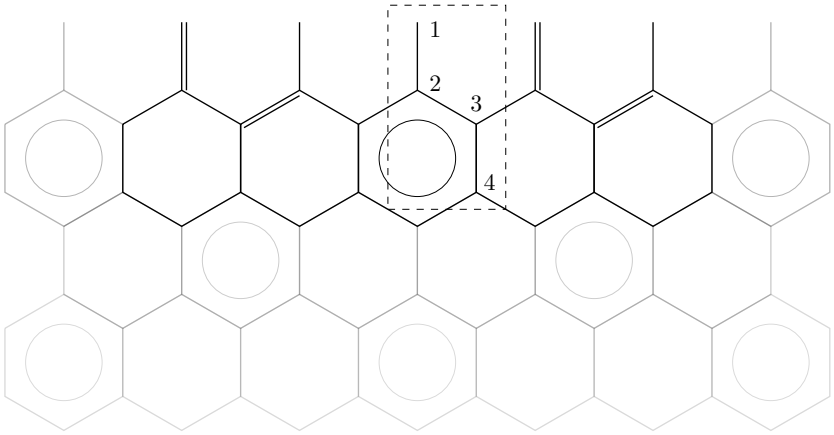

Figure 4.14: Graphene with a bearded edge and its unit cell. We label the states by $|m; k_x, j\rangle$, where $m = 1, ..., 4$ refers to the placement inside the unit cell from top to bottom, j refers to the row, and k_x is the Bloch wave number.

the basis

$$E - QHQ \doteq \begin{pmatrix} E & t\left(1+\mathrm{e}^{ik_x}\right) \\ t\left(1+\mathrm{e}^{-ik_x}\right) & E \end{pmatrix} = E\sigma_0 + t\left(1+\cos(k_x)\right)\sigma_1 - t\sin(k)\sigma_2. \tag{4.2.17}$$

The inverse of any combination of Pauli matrices is

$$\left(a_0\sigma_0 + a_1\sigma_1 + a_2\sigma_2 + a_3\sigma_3\right)^{-1} = \frac{1}{a_0^2 - a_1^2 - a_2^2 - a_3^2}\left(a_0\sigma_0 - a_1\sigma_1 - a_2\sigma_2 - a_3\sigma_3\right). \tag{4.2.18}$$

such that

$$\begin{aligned}(E - QHQ)^{-1} &\doteq \frac{1}{E^2 - t^2\left(1+\cos(k_x)\right)^2 - t^2\sin^2(k_x)}\left(E\sigma_0 - t\left(1+\cos(k_x)\right)\sigma_1 + t\sin(k_x)\sigma_2\right) \\ &= \frac{1}{E^2 - 4t^2\cos^2\left(\frac{k_x}{2}\right)}\begin{pmatrix} E & -t\left(1+\mathrm{e}^{ik_x}\right) \\ -t\left(1+\mathrm{e}^{-ik_x}\right) & E \end{pmatrix},\end{aligned} \tag{4.2.19}$$

which means

$$\begin{aligned}H_P|1;k_x,j\rangle &= -t|4;k_x,j-1\rangle - QHP\left(\frac{Et}{E^2 - 4t^2\cos^2\left(\frac{k_x}{2}\right)}|2,k_x,j\rangle - \frac{t^2}{E^2 - 4t^2\cos^2\left(\frac{k_x}{2}\right)}\left(1+\mathrm{e}^{-ik_x}\right)|3;k_x,j\rangle\right) \\ &= \frac{Et^2}{E^2 - 4t^2\cos^2\left(\frac{k_x}{2}\right)}|1;k_x,j\rangle - \frac{t^3\left(1+\mathrm{e}^{ik_x}\right)}{E^2 - 4t^2\cos^2\left(\frac{k_x}{2}\right)}|4;k_x,j\rangle,\end{aligned} \tag{4.2.20}$$

giving an effective hopping

$$\tilde{t}(E,k_x) = \frac{t^3\left(1+\mathrm{e}^{ik_x}\right)}{E^2 - 4t^2\cos^2\left(\frac{k_x}{2}\right)} \tag{4.2.21}$$

from $1 \to 4$, corresponding to t_1 in the SSH model. The effective Hamiltonian now describes an SSH chain of the form

$$\begin{aligned}H = \sum_{j=1}\Big(&\varepsilon(E,k_x)|j,A\rangle\langle j,A| + \varepsilon(E,k_x)|j,B\rangle\langle j,B| - \tilde{t}(E,k_x)|j,B\rangle\langle j,A| - \tilde{t}^*(E,k_x)|j,A\rangle\langle j,B| \\ &-t|j,B\rangle\langle j+1,A| - t|j+1,A\rangle\langle j,B|\Big),\end{aligned} \tag{4.2.22}$$

where the star in this case refers to complex conjugation. If we use the ansatz $E = 0$, we get

$$\tilde{t}(E=0,k_x) = \frac{t^3\left(1+\mathrm{e}^{ik_x}\right)}{-4t^2\cos^2\left(\frac{k_x}{2}\right)} = -\frac{t}{1+\mathrm{e}^{-ik_x}}. \tag{4.2.23}$$

We see that $|\tilde{t}(E=0,k_x)| \leq 1$ for $|k_x| \leq 2\pi/3$ and $|\tilde{t}(E=0,k_x)| > 2\pi/3$, so two thirds of the allowed values of k_x give an effective internal hopping that is smaller than the external hopping, which is the condition for edge states. This means that in two out of three unit cells there must be an edge state,

confirming what the heuristic model predicted. For AGNRs it means that when we make the bearded AGNR larger (adding two rows), every second time we add two new rows we also gain a new edge state. This means that for $n = 4, 6, 8, 10, \ldots$ rows, the number of edge states is either $1, 1, 2, 3, \ldots$ or $1, 2, 2, 3 \ldots$. To know which we have to calculate the number of edge states for $n = 4$ and $n = 6$, using the transfer matrices.

$$T_4 = \begin{pmatrix} 1 & -1 \\ -1 & 2 \end{pmatrix} = \frac{3}{2}\sigma_0 - \sigma_1 - \frac{1}{2}\sigma_0. \tag{4.2.24}$$

The eigenvalues are $\lambda = \frac{3}{2} \pm \sqrt{1 + \frac{1}{4}} = \frac{1}{2}\left(3 \pm \sqrt{5}\right)$ indicating that there is one edge state for $n = 4$ rows. For $n = 6$ rows the transfer matrix is

$$T = \begin{pmatrix} 1 & -1 & 1 \\ -1 & 2 & -2 \\ 1 & -2 & 3 \end{pmatrix}, \tag{4.2.25}$$

with eigenvalues $\lambda = 0.31,\ 0.64,\ 5.05$. As there are two edge states (also in line with the prediction of the heuristic model, see Figure D.1 in appendix D), the number of edge states for $n = 4, 6, 8, 10, \ldots$ is $1, 2, 2, 3, \ldots = \lfloor \frac{n}{3} \rfloor$.

4.3 Interface states

One of the main conclusions of Ref. [2] is that AGNRs can host interface states when joined together to form a heterojunction. Interface states are simply states that are localised to the boundary between the two AGNRs. If the AGNRs are of different topology, they host an odd number of interface states on the boundary between the two AGNRs, while there is an even number of interface states if they are topologically equivalent. Visually, joining two AGNRs means placing two of them next to each other, and creating extra σ bonds to join them (see the dashed bonds in Figure 4.15 4.16).
In this chapter we have analysed edge states and Dirac points in GNRs, and can now entirely predict how many edge states a given AGNR has and if it has a Dirac point, both through physical intuition and by analytical means, by showing that the ribbons (with the exception of the bearded) could be diagonalized as a set of SSH chains. In chapter 3 we calculated the Zak phase of the SSH model, which is related to the topological invariant, Z_2. There is still the outstanding question of whether or not to count the critical SSH chain in the topological or the trivial phase. Interface states can give physical meaning to this question. In fact interface states follow naturally from the analysis of edge states and Dirac points, and can be understood completely in the heuristic model. We will for zigzag and zigzag' terminations include Dirac points in the topological phase (for example, this means that the Zak phase of 5AGNR with the zigzag termination, $\gamma = \pi$, because it has a Dirac point and no edge states), which we will argue below. If we accept this classification, a ribbon can be

1. topologically nontrivial, by
   (a) having an odd number of edge states and no Dirac point, or
   (b) having an even number of edge states and a Dirac point.
2. topologically trivial, by
   (a) having an odd number of edge states and a Dirac point, or

(b) having an even number of edge states and no Dirac point.

If we have two topologically inequivalent AGNRs, neither of which have Dirac points (1a and 2b), it is because one of them has an odd number of edge states and the other has an even number. When joined, as many edge states as possible will pair up using the extra available π bond, but there will always remain an odd number of unpaired electron which are localised to the boundary. If they are topologically equivalent, there will be an even number of interface states. If there are two topologically equivalent ribbons, and one of them has a Dirac point, we can also explain the interface states (or lack thereof) in the heuristic model. In the heuristic model a Dirac point means there is an ambiguity in where to place the double bonds, an ambiguity the edge solves. But if the ribbon is joined with another ribbon, the configuration chosen by that given edge might change. This is perfectly illustrated by joining a zigzag AGNR with 5 rows and a zigzag' AGNR with 3 rows – this is shown in Figure 4.15. The Dirac chain in 5AGNR acts in this context as an edge state, as the double bonds can change configuration to pair up with the unpaired state on the opposite AGNR, serving as a justification for the convention of having the Dirac point part of the topologically nontrivial phase. See appendix E for more examples.

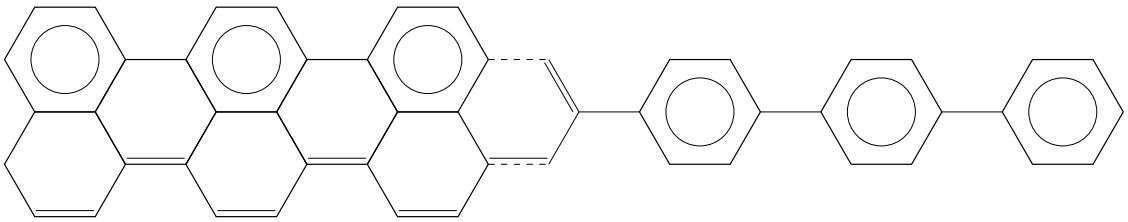

Figure 4.15: When two topologically equivalent AGNRs are joined there is no interface state. The zigzag 5AGNR has a Dirac point and no edge state, while the zigzag' 3AGNR has no Dirac point and one edge state. The joining of the two AGNRs changes the configuration of double bonds that an isolated zigzag AGNR with 5 rows otherwise has.

It was not possible to reduce the bearded AGNRs to a set of SSH chains, but we managed to find an expression for the number of edge states and Dirac points for an AGNR with n rows. We can therefore still try to relate them to a topological quantity, but we cannot naively assume that the Dirac points of bearded AGNRs behave exactly the same way as those of the zigzag/zigzag' AGNRs. To understand if it does play the same role, we look at heterojunctions with bearded ribbons, where one has a Dirac point. The smallest such ribbon has 8 rows, and $\lfloor \frac{8}{3} \rfloor = 2$ edge states. If we pair it with a bearded ribbon with 4 rows and $\lfloor \frac{4}{3} \rfloor = 1$ edge state, we would expect an even number of interface states, if the Dirac chain plays the same role as before.
In the heterojunction shown in Figure 4.16, the Dirac chain does not to play the same role as in the above. However, if we combine a bearded ribbon with 8 rows and 2 edge states with a bearded ribbon with 10 rows and 3 edge states, the heuristic model actually predicts zero interface states, because the Dirac chain in the bearded 8AGNR changes its configuration to pair up with the leftover edge state on the bearded 10AGNR (see Figure E.3 in appendix E). This means that we cannot assign a unique convention for bearded AGNRs with Dirac points. This is in contrast to the results from Ref. [2], where a unique convention *is* chosen for bearded AGNRs. However, in our model, it only made sense for the zigzag and zigzag' AGNRs, because we could interpret those as separate SSH chains. As this was not the case with the bearded ribbons, it is not viable to try to classify them in terms of SSH chains.
We now have all the information necessary to classify zigzag and zigzag' AGNRs according to their

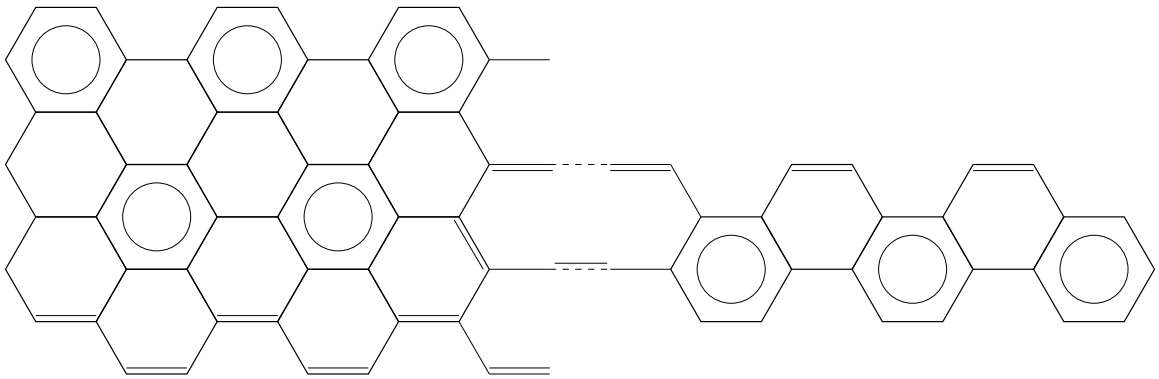

Figure 4.16: Heterojunction with two bearded AGNRs, one with a Dirac point and two edge states, the other with one edge state.

topology. There is a summary of the results in Table 4.1.

Termination	Zigzag (n = odd)	Zigzag (n = even)	Zigzag'	Bearded
Edge states	$\lfloor \frac{n}{6} \rfloor$	$\lfloor \frac{n+2}{6} \rfloor$	$\lfloor \frac{n}{6} \rfloor + 1$	$\lfloor \frac{n}{3} \rfloor$
Dirac point	$n \equiv_3 2$	$n \equiv_3 2$	$n \equiv_3 2$	$n \equiv_3 2$

Table 4.1: Summary of this chapter's finding for AGNRs. It should be noted that the expressions given for number of edge states is by no means unique for the given values of n. For example, $\lfloor \frac{n-1}{6} \rfloor = \lfloor \frac{n}{6} \rfloor$ for $n =$ Odd.

The topology is characterised by the invariant Z_2, which is related to the Zak phase through the relation [2]

$$(-1)^{Z_2} = \mathrm{e}^{i \sum_n \gamma_n} \tag{4.3.1}$$

where the sum is over occupied bands. It is clear that when $Z_2 = 0$ the Zak phase equals an even multiple of π, whereas if $Z_2 = 1$, the Zak phase equals an odd multiple of π. For the zigzag and zigzag' AGNRs, we want to construct a function that returns 1 when the sum of edge states and Dirac points is odd, and 0 when it is even. This can be done by using $f(n) = \lfloor \frac{n+2}{3} \rfloor$. If n is odd, $f(n)$ is even when $n \equiv_3 2$, otherwise $f(n)$ is odd. If n is even, $f(n)$ is odd when $n \equiv_3 2$, otherwise $f(n)$ is odd – $f(n)$ therefore returns an odd or even number depending on whether or not there is a Dirac point. For the zigzag AGNRs, the Z_2 invariant is then

$$Z_2 = \frac{1 + (-1)^{\lfloor \frac{n+3}{2} \rfloor + \lfloor \frac{n}{6} \rfloor}}{2} \tag{4.3.2}$$

for odd n. When n is even, the invariant is

$$Z_2 = \frac{1 - (-1)^{\lfloor \frac{n+3}{2} \rfloor + \lfloor \frac{n+2}{6} \rfloor}}{2}. \tag{4.3.3}$$

Zigzag' is similar to zigzag, except it always has one more edge state. Z_2 then becomes

$$Z_2 = \frac{1 - (-1)^{\lfloor \frac{n+3}{2} \rfloor + \lfloor \frac{n}{6} \rfloor}}{2} \tag{4.3.4}$$

for odd n.

4.4 Conclusion

In this chapter we have through heuristic and analytical methods calculated the number of edge states and Dirac points in different types of graphene nanoribbons. In the first section we showed that Dirac points are localised to separate sublattices, and the spectrum which is linear around $k = 0$ corresponds to a mixing of these two polarised states. The sublattice polarisation meant that we could derive conditions for the Dirac point that could only be satisfied for certain row numbers. We proceeded to give a physical explanation of why Dirac points exist in AGNRs, making a direct correlation with a simple 1D tight-binding chain, an explanation that gave the same conditions for the existence of Dirac points. Next we turned to edge states, which the heuristic model could predict completely for any ribbon. Having proven each of these predictions with analytical calculations, we finally turned to the topological classification of AGNRs in terms of edge states and Dirac points. This was done by reducing the problem to a set of independent one-dimensional SSH chains, which could be decoupled into separate chains, and analysed individually. We gave an intuitive argument for why in the critical case, the Dirac point belongs in the topological instead of the trivial class, allowing us to write an expression for the topological invariant for the zigzag and zigzag' ribbons. Unfortunately, this was not possible for the bearded AGNRs, as it could not be reduced to independent SSH chains, and even if it had been, the ribbons with Dirac points did not fit into a unique convention.

Chapter 5

Graphynes

In this chapter we look at graphynes, which are carbon-based two-dimensional materials similar to graphene. They consist of both sp2-hybridised atoms, each of which has three nearest neighbours (like in graphene) and sp-hybridised atoms, each of which has two nearest neighbours. They are a theoretical proposal, and very hard to synthesize experimentally [17, 18]. Predicted to rival (or even better) graphene's electronic properties [19], their synthesis would be extremely lucrative.
We will be analyzing four different graphynes in an effective model, wherein the π orbitlas of the sp-hybridised atoms are seen as links in an effective hopping, rather than individual orbitals contributing a band to the band structure. In the effective model there will be between one and three different hopping elements, all in graphene-like structures. For each of the graphynes we will explain the conditions that give rise to Dirac points and try to understand them in the heuristic model introduced in chapter 3. This analysis will contribute to a deeper understanding of Dirac points and edge states, and will serve as validation for the heuristic model applied to more exotic systems. The four types of graphyne we will look at are called α-, β-, γ-, and (6,6,12)-graphyne. All of them along with their unit cells are sketched in Figure 5.1.

5.1 α-graphyne

The first will be a very brief analysis, as α-graphyne immediately reduces to graphene in the effective model. The α-graphyne lattice (Figure 5.1a) is very similar to the hexagonal lattice of graphene, with two sp-hybridised carbon atoms placed between the sp2-hybridised carbon atoms. We can integrate out π orbitals of the sp-hybridised atoms, by considering two operators P and Q that project into π orbitals on sp2-hybridised atoms and π orbitals on sp-hybridised atoms respectively. As shown in chapter 3, this yields an effective Hamiltonian acting on the P states

$$H_P = PHP + PHQ\frac{1}{E - QHQ}QHP, \tag{5.1.1}$$

where H is the simple tight-binding Hamiltonian and E is the eigenenergy, which is to be solved self consistently. The first term is zero, as there are no nearest neighbour hoppings between sp2-hybridised atoms. The second term gives an effective hopping across the sp-hybridised orbitals as well as an on-site energy that we label

$$\tau = \frac{t_1^2 t_2}{E^2 - t_2^2} \tag{5.1.2}$$

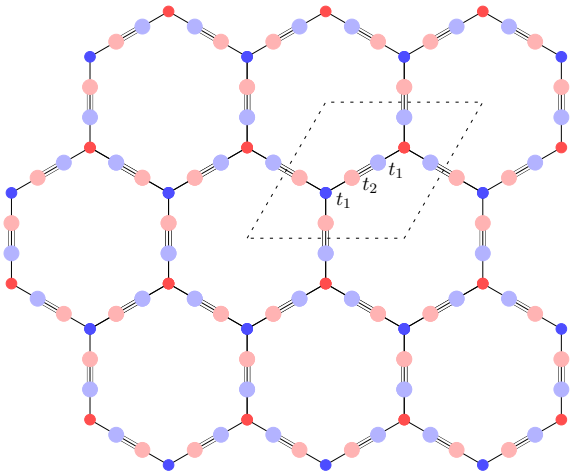

(a) α-graphyne.

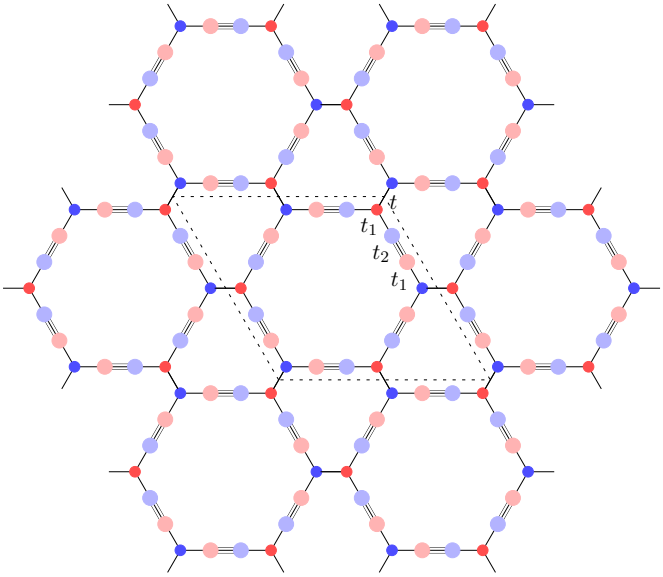

(b) β-graphyne.

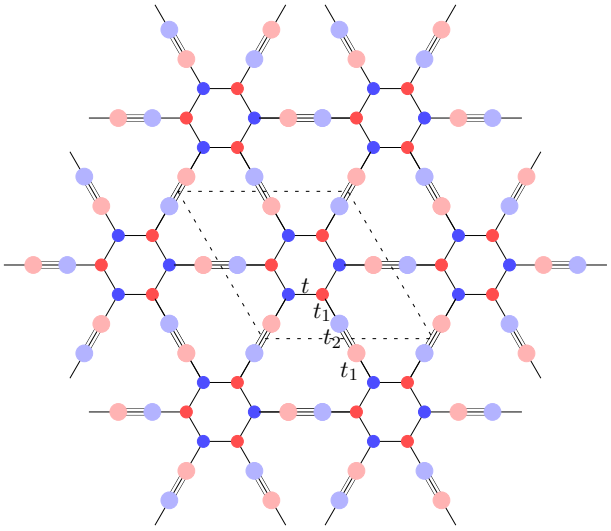

(c) γ-graphyne.

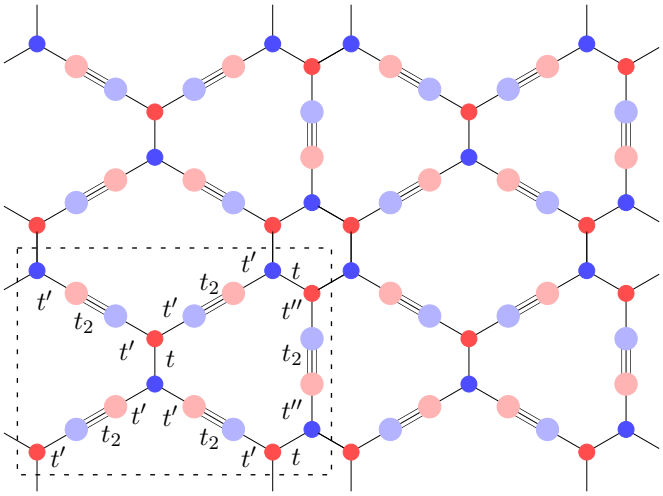

(d) $(6, 6, 12)$-graphyne.

Figure 5.1: Four different graphynes. α-, β-, and γ-graphyne all have a unit cell and Brillouin zone identical to those of graphene, whereas $(6, 6, 12)$-graphyne has a rectangular unit cell and Brillouin zone. The sp-hybridised atoms form triple bonds with each other.

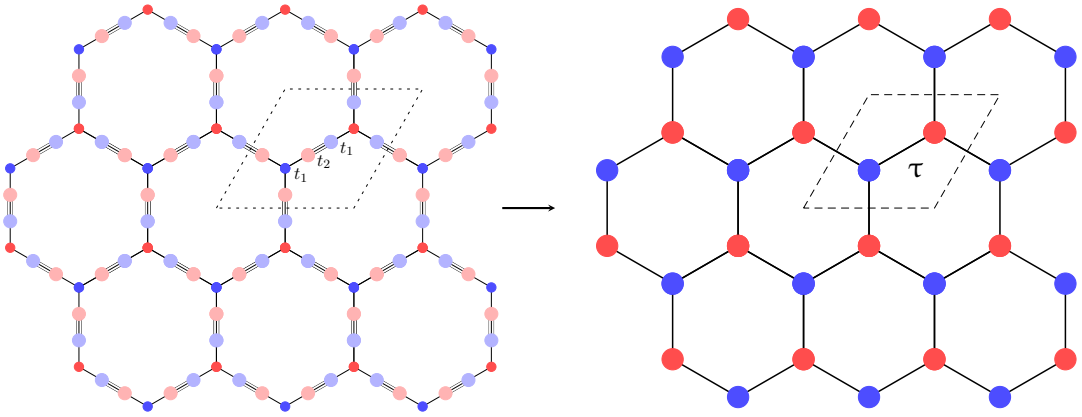

Figure 5.2: The triple bonds of α-graphyne are integrated out to give the graphene lattice, with an effective hopping parameter τ. In the effective lattice, all properties of graphene should also hold for α-graphyne.

and

$$\varepsilon = \frac{Et_1^2}{E^2 - t_2^2}. \tag{5.1.3}$$

We are not immediately interested in an exact expression for τ, but will rather try to understand at which values of τ Dirac points exist. In the case of α-graphyne, the lattice is replaced by an effective hexagonal lattice with hopping τ, which is the usual graphene lattice just with a modified hopping parameter – see Figure 5.2. Graphene has two Dirac points at the corners of the Brillouin-zone, which exist at all values of $\tau \neq 0$, so the same must be the case for α-graphyne. In this model α-graphyne has all the properties of graphene explained in chapter 2, but with modified hopping-dependent parameters, such as the Fermi velocity.

5.2 β- and γ-graphyne

β- and γ-graphyne (Figure 5.1b and 5.1c) are also hexagonal structures. If we apply the same procedure of integrating out the Q orbitals to the β-graphyne and γ-graphyne lattices, we are left with almost identical lattices, with the distinction that for β-graphyne the effective hopping, τ is the intracell hopping and t is the intercell hopping, and vice versa for γ-graphyne. As a matter of convention, we will for both lattices adopt the notation that t is the intracell hopping and τ is the intercell hopping, and see which regimes of τ allow for Dirac points. The reduced lattice is shown in Figure 5.3. As the nearest-neighbour tight-binding Hamiltonian only connects sites belonging to different sublattices (blue and red), the Hamiltonian can be constructed as a Kronecker product:

$$h = \left[\begin{pmatrix} 0 & 1 \\ 0 & 0 \end{pmatrix} \otimes h_B + \begin{pmatrix} 0 & 0 \\ 1 & 0 \end{pmatrix} \otimes h_R\right] = \frac{1}{2}\left[\sigma_1 \otimes (h_B + h_R) + \sigma_2 \otimes (ih_B - ih_R)\right], \tag{5.2.1}$$

where h_B and h_R act on blue and red sites respectively, like in the previous chapter.
Using the labelling of orbitals and unit vectors given in Figure 5.3, and for simplicity setting $t = 1$,

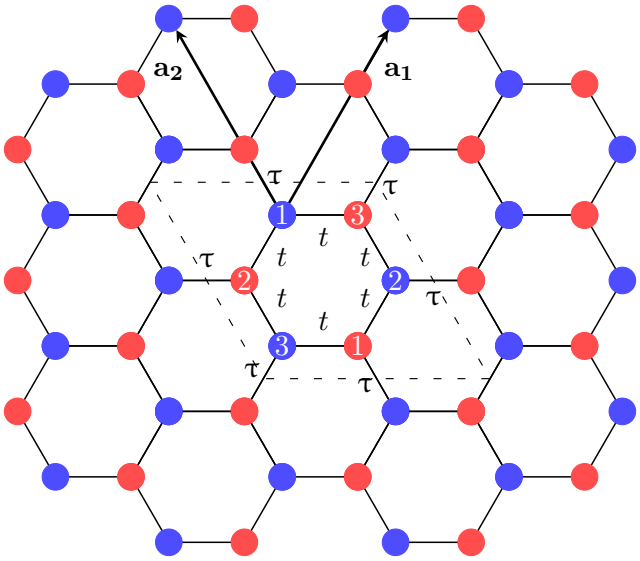

Figure 5.3: Reduced lattice of β- and γ-graphyne.

h_B and h_R take the form

$$h_B = -\begin{pmatrix} \tau e^{i\mathbf{k}\cdot\mathbf{a_2}} & 1 & 1 \\ 1 & \tau e^{i\mathbf{k}\cdot(\mathbf{a_1}-\mathbf{a_2})} & 1 \\ 1 & 1 & \tau e^{-i\mathbf{k}\cdot\mathbf{a_1}} \end{pmatrix}, \tag{5.2.2a}$$

$$h_R = -\begin{pmatrix} \tau e^{-i\mathbf{k}\cdot\mathbf{a_2}} & 1 & 1 \\ 1 & \tau e^{-i\mathbf{k}\cdot(\mathbf{a_1}-\mathbf{a_2})} & 1 \\ 1 & 1 & \tau e^{i\mathbf{k}\cdot\mathbf{a_1}} \end{pmatrix}. \tag{5.2.2b}$$

We solve the equation $\det(h_B) = 0$ to find the Dirac points:

$$\det(h_B) = -2 - \tau^3 + \tau\left(2e^{i\frac{3}{2}k_x}\cos\left(\frac{3\sqrt{3}}{2}k_y\right) + e^{i3k_x}\right). \tag{5.2.3}$$

To make things easier we look for solutions, where $k_x = 0$, leaving us with

$$-2 - \tau^3 + \tau\left(2\cos\left(\frac{3\sqrt{3}}{2}k_y\right) + 1\right) = 0. \tag{5.2.4}$$

We immediately see that for $\tau = 1$ (where it reduces to the graphene lattice) there is a Dirac point at $\mathbf{k} = (0, 0)$. This is no surprise, as graphene is of course known to have Dirac points. However at $\tau = 1$, $\mathbf{k} = (0, 0)$ is the *only* solution to $\det(h_B) = 0$, meaning that the two Dirac points that are usually located at two distinct corners of the Brillouin zone (when choosing the minimal unit cell, as done in chapter 2) merge to one point, the centre of the Brillouin zone. This means that of the six bands, four of them are linear around $\mathbf{k} = (0, 0)$ when the choice of unit cell is made as above. Considering $\tau \neq 1$ and $k_x = 0$, $\det(h_B) = 0$ yields the expression

$$\cos\left(\frac{3\sqrt{3}}{2}k_y\right) = \frac{1}{\tau} + \frac{\tau^2}{2} - \frac{1}{2}. \tag{5.2.5}$$

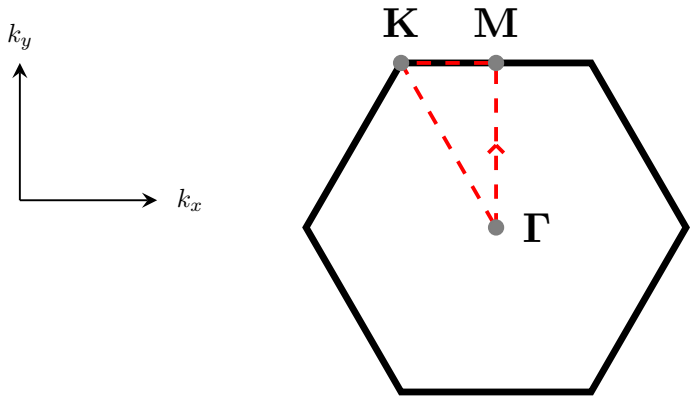

$$\mathbf{\Gamma} = (0,0)$$
$$\mathbf{M} = \frac{2\pi}{3}\left(0, \frac{1}{\sqrt{3}}\right)$$
$$\mathbf{K} = \frac{2\pi}{3c}\left(-\frac{1}{3}, \frac{1}{\sqrt{3}}\right)$$

Figure 5.4: First Brillouin zone for the reduced lattice of both β- and γ-graphyne, with the important high symmetry points given in units of $a_0 = 1$. The band structure for the two graphynes is plotted along the higlighted path, see Figure 5.5.

For the solutions, k_y to be real, the r.h.s. must satisfy

$$-1 \leq \frac{1}{\tau} + \frac{\tau^2}{2} - \frac{1}{2} \leq 1, \tag{5.2.6}$$

which guarantees Dirac points for

$$-2 \leq \tau \leq -1 \vee \tau = 1, \tag{5.2.7}$$

which lie at

$$\mathbf{k}'_{\pm} = \left(0, \pm\frac{2}{3\sqrt{3}}\cos^{-1}\left(\frac{1}{\tau} + \frac{\tau^2 - 1}{2}\right)\right). \tag{5.2.8}$$

There are two solutions, since cos is an even function. As $h_B = h_R^\dagger$, the existence of a Dirac point on one sublattice for a given $\mathbf{k} = \mathbf{k}'$ guarantees the existence of one on the opposite sublattice at the same $\mathbf{k}$, since $\det\left(h_B\left(\mathbf{k}'\right)\right) = 0 \Rightarrow \det\left(h_R\left(\mathbf{k}'\right)\right) = \left(\det\left(h_B\left(\mathbf{k}'\right)\right)\right)^* = 0$. For β-graphyne, $\tau = -1.17$ and for γ-graphyne, $\tau = -0.87$ [20]. For these values we expect β-graphyne to have one Dirac point and γ-graphyne to have none, which is confirmed by the band structures calculated along the $\Gamma \to M \to K \to \Gamma$ path in the first Brillouin zone (see Figure 5.4), shown in Figure 5.5.

5.3 $(6, 6, 12)$-graphyne

The last graphyne structure we will look at is $(6, 6, 12)$-graphyne (Figure 5.1d). In recent years there have been successful attempts at synthesizing a model compound [18]. Integrating out the π orbitals of the sp-hybridised atoms gives us three different hoppings, $t = 1$, τ_1 and τ_2. The effective lattice is shown in Figure 5.6.
The Hamiltonian has the same form as in (5.2.1). In the basis lain out in Figure 5.6, h_B and h_R take the form

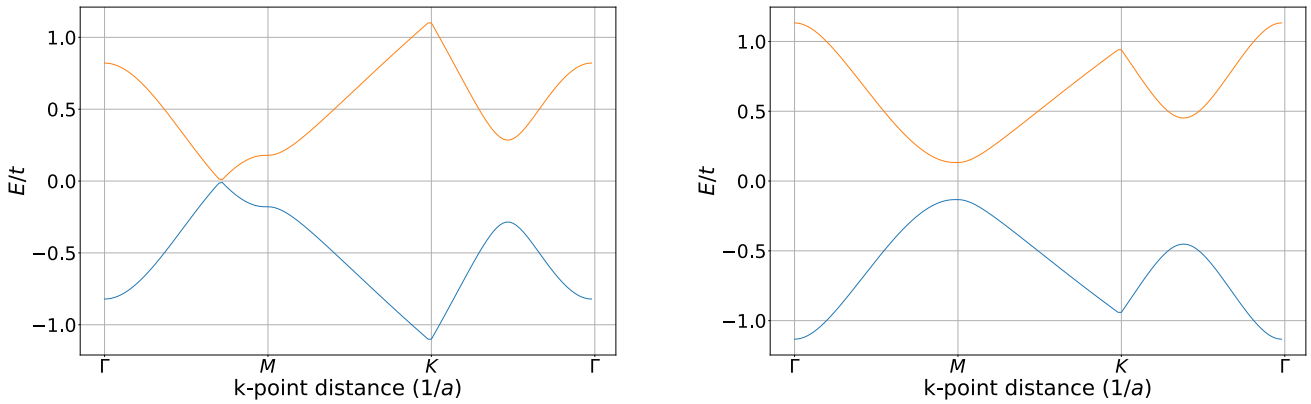

(a) β-graphyne. **(b)** γ-graphyne

Figure 5.5: Band structure of β- and γ-graphyne in the reduced model, showing the highest occupied band and lowest unoccupied band. β-graphyne exists in the regime of τ's that allow for a Dirac point, but γ-graphyne does not. The values of τ used are taken from Ref. [20].

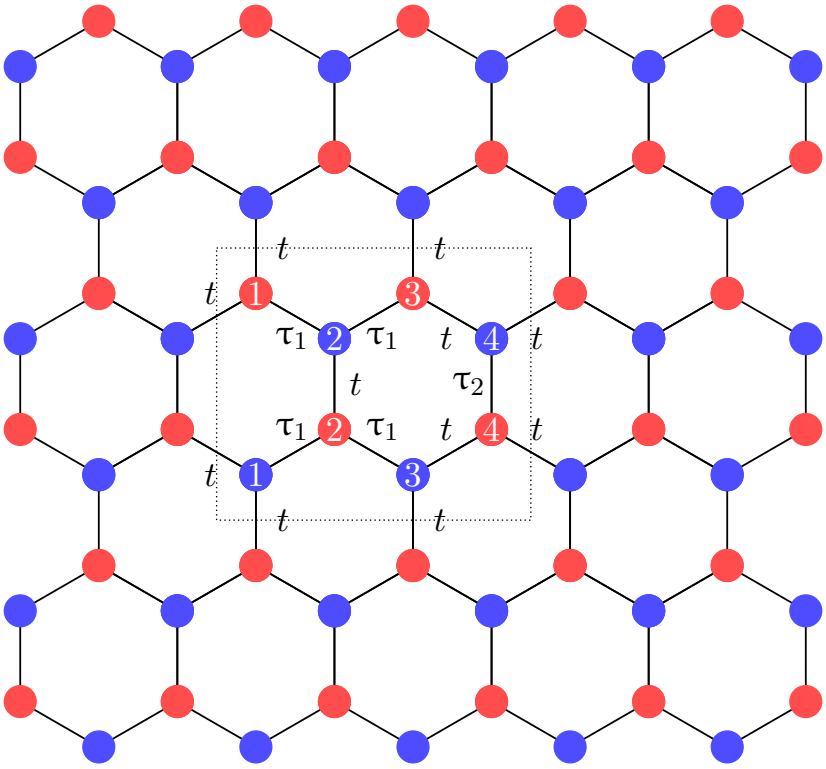

Figure 5.6: Reduced lattice of (6,6,12)-graphyne.

$$h_B = -\begin{pmatrix} e^{-ik_y a_2} & \tau_1 & 0 & e^{ik_x a_1} \\ \tau_1 & 1 & \tau_1 & 0 \\ 0 & \tau_1 & e^{-ik_y a_2} & 1 \\ e^{-ik_x a_1} & 0 & 1 & \tau_2 \end{pmatrix}, \tag{5.3.1a}$$

$$h_R = -\begin{pmatrix} e^{ik_y a_2} & \tau_1 & 0 & e^{ik_x a_1} \\ \tau_1 & 1 & \tau_1 & 0 \\ 0 & \tau_1 & e^{ik_y a_2} & 1 \\ e^{-ik_x a_1} & 0 & 1 & \tau_2 \end{pmatrix}. \tag{5.3.1b}$$

Note that since the unit cell has mirror symmetry, $h_R(k_x, k_y) = h_B(k_x, -k_y)$. As the Brillouin zone is rectangular, the band structure is calculated along the path $\mathbf{\Gamma} \to \mathbf{X}' \to \mathbf{M} \to \mathbf{X} \to \mathbf{\Gamma}$. Along this path we can find the conditions for Dirac points to exist, by solving $\det(h_B) = 0$.

$$\det(h_B) = 2\tau_1^2 (1 - \cos(k_x a_1)) + e^{-2ik_y a_2}\tau_2 - 2e^{-ik_y a_2}\left(1 + \tau_1^2 \tau_2\right) = 0. \tag{5.3.2}$$

We start by setting $k_y = 0$ (this corresponds to the $\mathbf{\Gamma} \to \mathbf{X}'$ part of the path):

$$-2 + 2\tau_1^2 (1 - \cos(k_x a_1) - \tau_2) + \tau_2 = 0 \quad \Rightarrow \quad \cos(k_x a_1) = \frac{\tau_2 - 2 + 2\tau_1^2 - 2\tau_1^2\tau_2}{2\tau_1^2}. \tag{5.3.3}$$

As above, for the solution k_x to be real, τ_1 and τ_2 must satisfy

$$-1 \leq \frac{\tau_2 - 2 + 2\tau_1^2 - 2\tau_1^2\tau_2}{2\tau_1^2} \leq 1. \tag{5.3.4}$$

For the first part of the condition, we get

$$-1 \leq \frac{\tau_2 - 2 + 2\tau_1^2 - 2\tau_1^2\tau_2}{2\tau_1^2} \quad \Rightarrow \quad 0 \leq (\tau_2 - 2)\left(1 - 2\tau_1^2\right), \tag{5.3.5}$$

which is fulfilled when

$$\tau_2 \geq 2 \wedge 1 \geq 2\tau_1^2 \quad \vee \quad \tau_2 \leq 2 \wedge 1 \leq 2\tau_1^2. \tag{5.3.6}$$

For the second part of (5.3.4) to hold, we get

$$1 \geq \frac{\tau_2 - 2 + 2\tau_1^2 - 2\tau_1^2\tau_2}{2\tau_1^2} \quad \Rightarrow \quad 2 \geq \tau_2\left(1 - 2\tau_1^2\right), \tag{5.3.7}$$

which is true for

$$\tau_2 \leq \frac{2}{1 - 2\tau_1^2} \wedge 1 \geq 2\tau_1^2 \quad \vee \quad \tau_2 \geq \frac{2}{1 - 2\tau_1^2} \wedge 1 \leq \tau_1^2. \tag{5.3.8}$$

The conditions given here guarantee at least one pair of Diracs point in the spectrum, one of which which lies on the ***Gamma*** $\to \mathbf{X}'$ line in the Brillouin zone (the other lies on the $\mathbf{\Gamma} \to -\mathbf{X}'$ line). A pair of Dirac point can also exist on the $k_y = \pi/a_2$ line, $\mathbf{M} \to \mathbf{X}$ line, provided a different set of conditions for τ_1 and τ_2 is satisfied. For $k_y = \pi/a_2$, the determinant, $\det(h_B)$ is

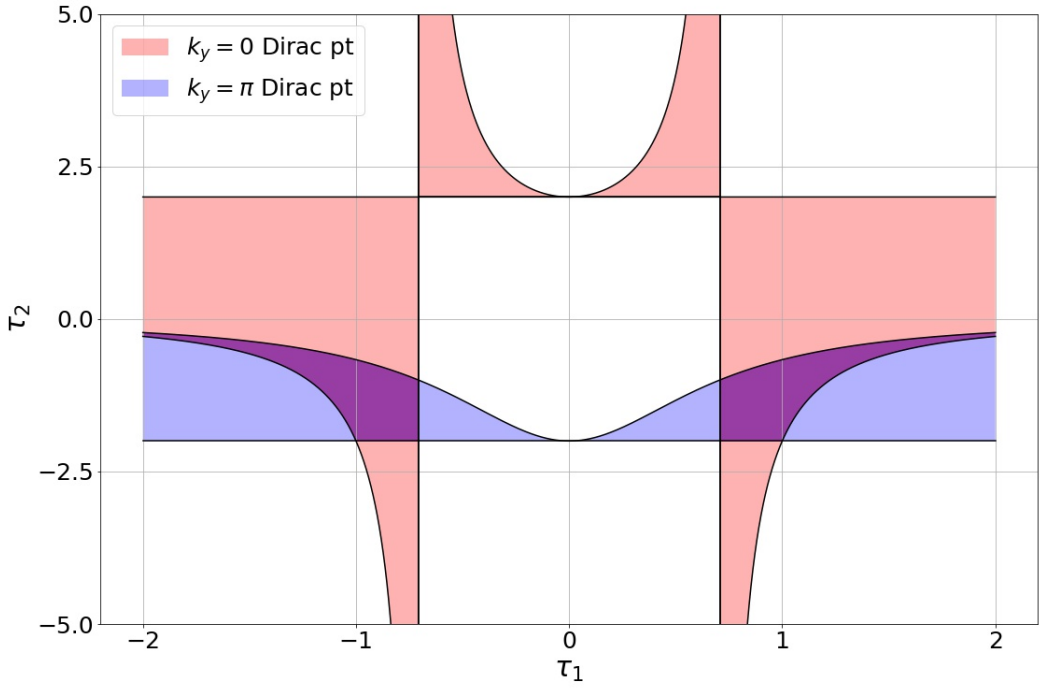

Figure 5.7: Phase diagram of (6,6,12)-graphyne, with the values of τ_1 and τ_2 allowing for Dirac points highlighted. In each distinct region there are two Dirac points, and in the overlapping region there are four Dirac points.

$$2 + 2\tau_1^2\left(1 - \cos\left(k_x a_1\right) - \tau_2\right) + \tau_2 = 0 \quad \Rightarrow \quad \cos\left(k_x a_1\right) = \frac{2 + \tau_2 + 2\tau_1^2 + 2\tau_1^2\tau_2}{2\tau_1^2} \tag{5.3.9}$$

Once again, applying the conditions of $-1 \leq \cos\left(k_x a_1\right) \leq 1$, we arrive at

$$-1 \leq \frac{2 + \tau_2 + 2\tau_1^2 + 2\tau_1^2\tau_2}{2\tau_1^2} \quad \Rightarrow \quad \tau_2 \geq -2, \tag{5.3.10}$$

and

$$\frac{2 + \tau_2 + 2\tau_1^2 + 2\tau_1^2\tau_2}{2\tau_1^2} \leq 1 \quad \Rightarrow \quad \tau_2 \leq -\frac{2}{1 + 2\tau_1^2}, \tag{5.3.11}$$

giving another set of conditions for a second pair of Dirac points to exist along the $M \to X$ line. The values of (τ_1, τ_2) that allow for Dirac points are highlighted in the phase diagram in Figure 5.7. From [20], we get $\tau_1 = -0.73$ and $\tau_2 = -1.03$, which according to the phase diagram allows for two pairs of Dirac points, each on the $\mathbf{\Gamma} \to \mathbf{X}'$ line and the $\mathbf{M} \to \mathbf{X}$ line. We verify this by explicitly calculating the band structure, see Figure 5.8.

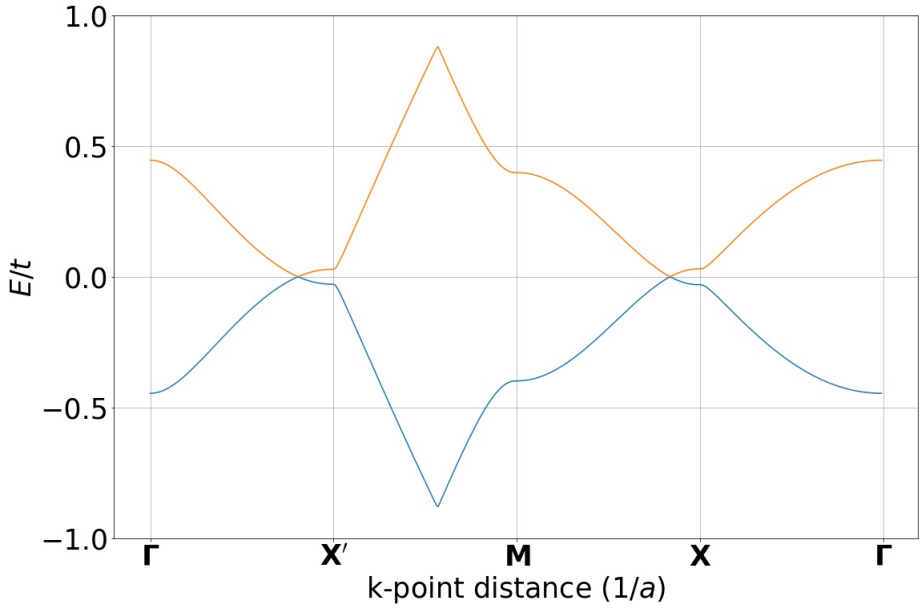

Figure 5.8: The tight-binding band structure of (6,6,12)-graphyne calculated along the $\Gamma \to X' \to M \to X \to \Gamma$ path in the first Brillouin zone.

5.4 Edge states in graphyne

Having established the existence of Dirac points in β- and (6,6,12)-graphyne (and α-graphyne, but that is trivial) we now look for potential edge states on the zigzag edge of these graphynes. There are two main purposes to searching for edge states in graphynes. One is to gain a better understanding of the relation between edge states and Dirac points. In chapter 4 we saw in AGNRs with zigzag and zigzag' edges that new edge states and Dirac points occured at the same frequency, both occurring for every six rows added to the ribbons. It is obvious that there is a physical relation between the two states, but it is not entirely clear what it is. The other purpose is to use the heuristic model on graphynes, and see if it can explain the number of edge states we find. We start by looking at β-and γ-graphyne.

5.4.1 Edge states in β- and γ-graphyne

As the unit cell for β- and γ-graphyne is not rectangular, it will have to be altered to accomodate an edge. Instead of holding six atoms, the rectangular unit cell will incorporate twelve atoms, see Figure 5.9. Based on what we know about zero-energy modes in the tight-binding model we can assume the edge states to have zero energy and to be sublattice polarised. As such we assume the amplitude to be zero on the blue sublattice and nonzero on the red (see Figure 5.9), and can, using the destructive interference on blue sites, derive an expression for $c_{j+1,2}$, $c_{j+1,4}$, and $c_{j+1,6}$ as a function of $c_{j,2}$, $c_{j,4}$, and $c_{j,6}$. $c_{j,i}$ refers to the amplitude on the red sites. Each blue site yields an equation and the set of equations to be solved is

$$-c_{11} - c_{12} - \tau e^{-ik_x} c_{16} = 0, \tag{5.4.1a}$$

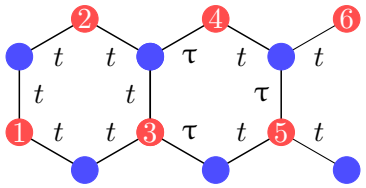

Figure 5.9: Unit cell of β-and γ-graphyne when taking the zigzag edge into account.

$$-c_{12} - \tau c_{14} - c_{13} = 0, \tag{5.4.1b}$$

$$-c_{14} - c_{16} - \tau c_{15} = 0, \tag{5.4.1c}$$

$$-c_{11} - c_{13} - \tau c_{22} = 0, \tag{5.4.1d}$$

$$-\tau c_{13} - c_{15} - c_{24} = 0, \tag{5.4.1e}$$

$$-c_{15} - \tau \mathrm{e}^{ik} c_{11} - c_{26} = 0. \tag{5.4.1f}$$

Solving these equations for c_{22}, c_{24}, and c_{26} gives the transfer matrix

$$T = \begin{pmatrix} \frac{2}{\tau} & 1 & \mathrm{e}^{-ik} \\ \tau & \frac{1}{\tau} + \tau^2 & \frac{1}{\tau} \\ \tau \mathrm{e}^{ik} & \frac{1}{\tau} & \tau^2 + \frac{1}{\tau} \end{pmatrix}. \tag{5.4.2}$$

Finding the eigenvalues analytically will be too hard, so we settle for finding them numerically. We are interested in edge states in the context of their relation to Dirac points, and the heuristic model. As we cannot analyse the eigenvalues of (5.4.2) analytically, we table the discussion to section 5.5.

5.4.2 Edge states in (6, 6,12)-graphyne

In (6,6,12)-graphyne, we can construct two different zigzag terminations, and for each of them we can derive the transfer matrix (the two terminations correspond to either starting with a row of C rings or A/B rings, see Figure 5.12a in the following section). The eigenvalues of both terminations are identical, but their eigenvectors are not. The eigenvalues alone therefore do not tell us whether there is an edge state on a given termination, but just that one of the two terminations supports edge states. We construct the transfer matrix in which the unit cell given in Figure 5.6 is the end termination. Using periodic boundary conditions along the zigzag edge and assuming the amplitude on the blue sites to be zero, we get the following set of equations

$$-\tau_1 (c_{11} + c_{13}) - c_{12} = 0, \tag{5.4.3a}$$

$$-c_{13} - \mathrm{e}^{ik} c_{11} - \tau_2 c_{14} = 0, \tag{5.4.3b}$$

$$-\tau_1 c_{12} - \mathrm{e}^{-ik} c_{14} - c_{21} = 0, \tag{5.4.3c}$$

$$-\tau_1 c_{12} - c_{14} - c_{23} = 0. \tag{5.4.3d}$$

Solving this for c_{21} and c_{23} yields the transfer matrix

$$T = \begin{pmatrix} \frac{1}{\tau_2} + \tau_1^2 & \frac{e^{-ik_x}}{\tau_2} + \tau_1^2 \\ \frac{e^{ik_x}}{\tau_2} + \tau_1^2 & \frac{1}{\tau_2} + \tau_1^2 \end{pmatrix}. \tag{5.4.4}$$

The eigenvalues are

$$\lambda_\pm = \frac{1}{\tau_2} + \tau_1^2 \pm \sqrt{\tau_1^4 + \frac{1}{\tau_2^2} + \frac{2\tau_1^2\cos(k_x)}{\tau_2}}. \tag{5.4.5}$$

The norm of each eigenvalue can tell us something important about the system. $|\lambda| = 1$ corresponds to a Dirac point and $|\lambda| < 1$ means that there is an edge state. This is very similar to the SSH model: the ratio between the internal and external hopping amplitudes, t_1/t_2, played the role that $\lambda_\pm$ plays here. To open and close a gap, and create and annihilate an edge state the hopping amplitudes need to be manipulated. In (6,6,12)-graphyne we have two hopping amplitudes, and a Bloch wave number which comes from having translational invariance in the x-direction. The key difference is that here we have the potential for two pairs of Dirac points and therefore also two edge states. Figure 5.7 shows the regions of the τ_1-τ_2 phase space in which the two Dirac points are allowed, with hard boundaries signifying the closing of gaps. We argue that these boundaries are in fact not only meaningful for Dirac points, but are indicators of edge states. First we show for good measure that $|\lambda_\pm| = 1$ yields the same conditions for the Dirac points as we derived above. We start with $|\lambda_+| = 1$. λ_+ can be taken to be $+1$ for the values of (τ_1, τ_2) we are interested in.

$$\lambda_+ = 1 \quad \Rightarrow \quad \sqrt{\tau_1^4 + \frac{1}{\tau_2^2} + \frac{2\tau_1^2\cos(k_x)}{\tau_2}} = 1 - \tau_1^2 - \frac{1}{\tau_2}. \tag{5.4.6}$$

Squaring both sides and rearranging gives

$$\cos(k_x) = \frac{2\tau_1^2 - 2 - 2\tau_1^2\tau_2 + \tau_2}{2\tau_1^2}, \tag{5.4.7}$$

which is identical to the expression in (5.3.3) for the Dirac point on the $k_y = 0$ line in the first Brillouin zone. For $|\lambda_-| = 1$, we take λ_- to be negative and solve $\lambda_- = -1$:

$$\frac{1}{\tau_2} + \tau_1^2 - \sqrt{\tau_1^4 + \frac{1}{\tau_2^2} + \frac{2\tau_1^2\cos(k_x)}{\tau_2}} = -1 \Rightarrow \cos(k_x) = \frac{2\tau_1^2 + 2 + 2\tau_1^2\tau_2 + \tau_2}{2\tau_1^2}, \tag{5.4.8}$$

identical to the expression in (5.3.9) for the Dirac point lying at the $k_y = \pi$ line on the boundary of the first Brillouin zone. Each eigenvalue is then responsible for a distinct Dirac point. It is therefore clear that the Dirac points can just as well be extracted from the transfer matrix as the Hamiltonian. What we are interested in are the edge states, however. In chapter 3 we derived an expression for an effective hopping in graphene (which played the role that λ plays here), which also depended on the wave number, k_x. We saw that for exactly one third of the allowed values of k_x, this t_2 was smaller than t_1, which meant that there was an edge state in every third unit cell.

As the eigenvalues are continuous, $|\lambda_\pm(k_x)|$ will (for given values of (τ_1, τ_2)) either be entirely above 1 for all $k_x \in [-\pi, \pi]$, entirely below 1 or cross 1 at $k_x = k_x^*$, where k_x^* is one of the Dirac points (depending on which eigenvalue it is). The Dirac points therefore serve as a critical value for the edge states. There need not be a Dirac point for there to be an edge state (this is the case when $|\lambda_\pm| < 1$, $\forall k_x \in [-\pi, \pi]$), but the Dirac points serve as a boundary between the phase with edge states

and the phase with no edge states. For an edge state to be added to or removed from the system, a gap needs to be opened or closed in the band structure. To illustrate this, we plot $|\lambda_{\pm}|$ for five different points in the phase diagram – this is done in Figure F.1 and F.2 in appendix F. What we find is the following:

1. In the totally gapped phase, there is one edge state, existing at all values of k_x.
2. When we enter the partially gapless phase, the edge state density decreases.
3. Entering the fully gapless phase, a new edge state appears.
4. As we leave the fully gapless phase, entering another partially gapless phase, the first edge state disappears, while the second remains.
5. Entering the fully gapped phase, the second edge state now exists at all values of k_x.

5.5 Graphynes in heuristic model

It is time to apply the heuristic model that was developed in chapter 3, and was so successful in describing graphene nanoribbons in chapter 4, to graphyne. We saw in chapter 3 that it was able to predict the edge state density along the zigzag edge of graphene. In chapter 4 it became apparent that not only did the model accurately predict edge states for several edges, but it also provided a description of Dirac points. It turned out that when $n \equiv_3 2$, where n is the number of rows in a ribbon, there was a Dirac point, because there was a leftover chain of atoms, whereas if $n \equiv_3 0, 1$ the spectrum was gapped. But when we are not analyzing ribbons of discrete width, the number of rows is a meaningless quantity, and the spectrum of graphene is not gapped. Of course the gap of the AGNRs whose number of rows, $n \equiv_3 0, 1$ goes to zero as n becomes large (the gap decreases as a power law) since we are squeezing more and bands into a finite range of energy.
With graphynes we are not analyzing discrete ribbons, but rather a system with assumed translational invariance, and it is clear that the existence of the Dirac points very much depends on the value of the different hopping parameters. So how can this issue be treated in the heuristic model? In this section we aim to provide an intuitive explanation of why Dirac points and edge states are possible and *when* they are possible in not so intuitive materials.

5.5.1 β- and γ-graphyne in heuristic model

To explain the issue of Dirac points and edge states in graphynes we draw a direct parallel between 2D graphene (and graphynes) and the 1D SSH model. In the SSH model the critical case, $t_1 = \pm t_2$ yields a Dirac point. In chapter 3 we argued that this could be seen as a result of the ambiguity of where to place the double bonds, whereas in the topological and trivial cases there was no ambiguity at all. In pristine graphene there is the same hopping amplitude between all the π-electrons, and this means that there is an ambiguity about where to place the aromatic rings, as for a given row of benzene rings, the aromatic ring can be placed in any of three benzene rings – there are thus three choices, all of which are equally stable and return the same many-body ground state energy. In graphene there is therefore a threefold ambiguity and there are two Dirac points, whereas in the SSH model there was in the critical case a twofold ambiguity and one Dirac point. An ambiguity in the heuristic model certainly seems to be an indicator of Dirac points, but whether the degree of ambiguity and number of Dirac points can be linked, is an open question.

From Figure 5.3, it is apparent that the reduced lattice of β- and γ-graphyne can be seen as a set of two different benzene rings connected to each other, see Figure 5.10. Notice that an isolated type B ring is in fact just the SSH model with periodic boundary conditions, with three unit cells. The dispersion is given in (3.2.6) and with three unit cells, the allowed values of k are $[-2\pi/3, 0, 2\pi/3]$, giving the energy levels

$$E(\tau) = \pm(1+\tau), \pm\sqrt{1-\tau+\tau^2}. \tag{5.5.1}$$

As $\cos(k)$ is even, the $k = \pm 2\pi/3$ levels are degenerate. The gap between the highest occupied and lowest unoccupied states is the measure of stability a benzene ring, and in the type B ring the gap is given by

$$\Delta_B(\tau) = \begin{cases} 2\sqrt{1-\tau+\tau^2}, & \tau \geq 0, \\ |2+2\tau|, & \tau < 0. \end{cases}$$

For certain values of τ, the type A ring is a more stable ring and in others, the type B ring is more stable. In these regimes of τ the graphyne spectrum is gapped, because there is no ambiguity in where to place the aromatic rings. A perfect example of this is when $\tau = 1$. As mentioned above this is just graphene, with the benzene ring as our unit cell. In this case there is a double Dirac point at $\mathbf{k} = 0$. But if τ varies just slightly from this value, $\tau = 1 + \delta\tau$ for some small $\delta\tau$, a gap opens because one type of ring is clearly more stable than the other (B is preferred if $\tau > 1$).
When $\tau < -2$, $\Delta_B(\tau) > 2$, so the type B Benzene ring is preferred. When $\tau = -2$, $\Delta_B(-2) = 2$, and there is once again an ambiguity giving rise to the Dirac point. When $-2 < \tau < -1$, $\Delta_B < 2$, but the ambiguity continues because the strength of the link connecting the A rings is larger than the individual bonds of the A ring – a gap of $2|\tau|$ is achieved by filling two electrons in a τ π-bond. When $-1 < \tau < 1$ the A ring is clearly more stable, and there is once again no Dirac point.
This analysis is also capable of predicting edge states. In the ranges where one ring is clearly more stable than the other, $\tau < -2, -1 < \tau < 1, \tau > 1$, the regular filling scheme should be used. Whether it be A or B rings that are filled, we would (like in zigzag graphene) see an edge state on every third site, or (given our choice of unit cell) one edge state pr. unit cell. This is the same as saying that the modulus of one of the three eigenvalues of (5.4.2) should be smaller than 1, which is indeed what we find in each range (see Figure 5.11 for three examples).

5.5.2 (6,6,12)-graphyne in heuristic model

Like β- and γ-graphyne, the Dirac points of (6,6,12)-graphyne can also be analysed in the heuristic model, and the (6,6,12) lattice can too be seen as a set of connected Benzene rings of different types. (6,6,12)-graphyne has three different types of Benzene rings: two types, A and B, occupy every second benzene ring of every second row, and type C occupies every ring of every other row (see Figure 5.12). What was apparent in the above section is that the important quantities are *a*) the gap between highest occupied and lowest unoccupied state in a given type of benzene ring, and *b*) the strength of the bond connecting different benzene rings. (6,6,12)-graphyne is significantly harder to deal with in the heuristic model, as there are three types of benzene rings whose individual spectra are not straightforward to calculate analytically, and there are three different hopping parameters. In fact (6,6,12) serves as the limit of what the heuristic model can predict. We can however take extreme values of (τ_1, τ_2) and look at what we can expect in terms of Dirac points (the phase diagram in Figure 5.7 will help us) and edge states (the calculations in section 5.4 can guide us).
Take for example $(\tau_1, \tau_2) = (-1, 2.5)$. This point is outside the highlighted regions in Figure 5.7, so

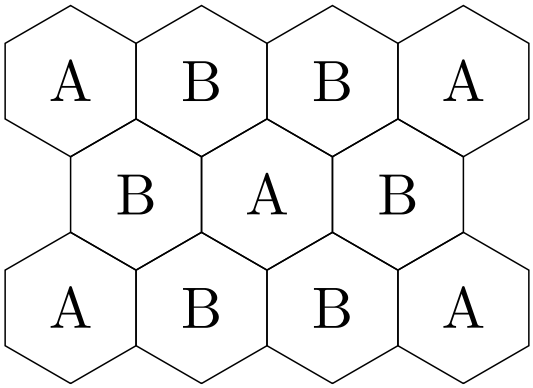

(a) The reduced lattice of β- and γ-graphyne can be seen as a set of two different benzene rings, where each type A ring is surrounded by six type B rings, and each type B ring is surrounded by three type A and three type B rings.

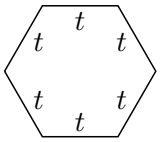

(b) Type A is just the standard benzene ring, with gap $\Delta_A = 2$.

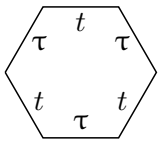

(c) Type B has hopping τ between every second pair of atoms.

Figure 5.10: To analyse β- and γ-graphyne in the heuristic model, we must look at the lattice as different sets of interlocking benzene rings.

we should be able to explain both the edge state density and the lack of Dirac points in the band structure. For the values given, the gaps are $(\Delta_A, \Delta_B, \Delta_C) = (2, 2, 1.68)$. Clearly rings A and B are equally stable There is no ambiguity though, because A rings are connected laterally with τ_2, a stronger bond than t, which connects B rings. The ground state is then the one, where B rings are entirely filled and each τ_2 bond is doubly filled by a bonding orbital. Along the edge there is an unpaired electron on the top site of each A ring, so there is one edge state pr. unit cell. This is exactly what the transfer matrix eigenvalues (5.4.5) tell us, since $|\lambda_+| < 1 | \lambda_-| > 1$, $\forall k \in [-\pi, \pi]$. Unfortunately the fact that there are three types of benzene rings to take into account, makes it a little to hard to make broader predictions in the heuristic model.

5.6 Berry phase in graphynes

So far, we have in this chapter studied edge states and Dirac points in graphynes, like we did with graphene nanoribbons in the previous chapter. Now we turn to deriving an expression for the Berry phase, the 2D analogue of the Zak phase which was calculated in the last chapter. If the Hamiltonian is given as in (5.2.1), where there is a Dirac point at $\mathbf{k} = \mathbf{k}^*$, let then $|\phi\rangle$ be the real space component of the Dirac point on both sublattices, such that $h_B(\mathbf{k}^*)\,|\phi\rangle = h_R(\mathbf{k}^*)\,|\phi\rangle = 0$. The states $\left|\psi_{\uparrow/\downarrow}\right\rangle = |\uparrow / \downarrow\rangle \otimes |\phi\rangle$ are then both zero-energy eigenstates of the full Hamiltonian, $h(\mathbf{k}^*)$, and so is any linear combination of the two. If we let $\mathbf{q}$ be a small deviation from $\mathbf{k}^*$, such that $\mathbf{k} = \mathbf{k}^* + \mathbf{q}$, we can expand h to first order in $\mathbf{q}$.

$$h = \sigma_1 \otimes \left(h_1\left(\mathbf{k}^*\right) + h_1^{(1)}\left(\mathbf{q}\right)\right) + \sigma_2 \otimes \left(h_2\left(\mathbf{k}^*\right) + h_2^{(1)}\left(\mathbf{q}\right)\right) + \ldots \tag{5.6.1}$$

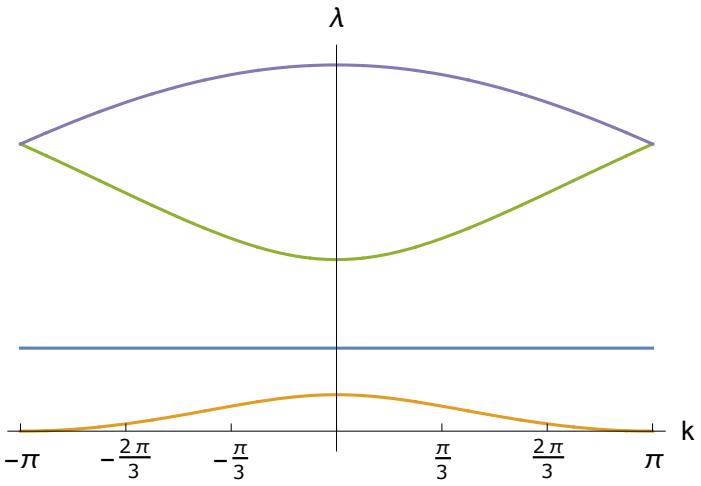

(a) Transfer matrix eigenvalues for $\tau = -2.1$

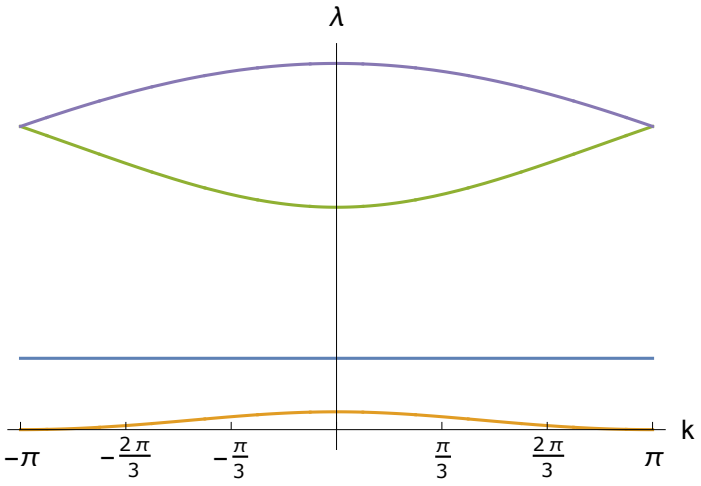

(b) $\tau = 0.5$

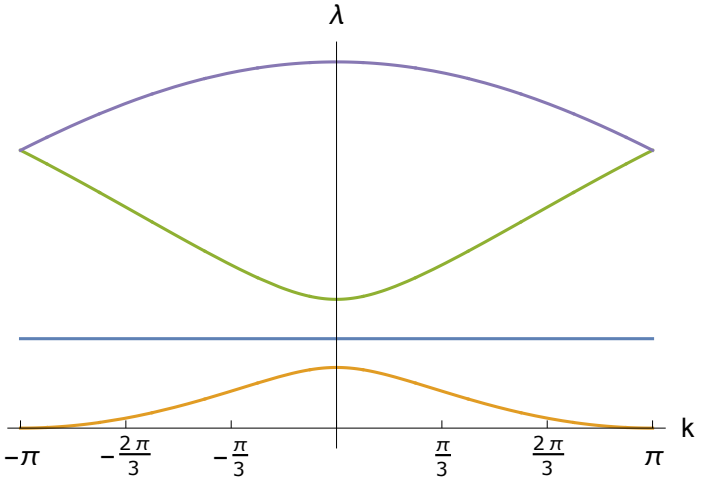

(c) $\tau = 1.2$

Figure 5.11: The modulus of the eigenvalues of (5.4.2) plotted for $-\pi \leq k \leq \pi$ for three different values of τ. The blue line is 1, and in each of the plots, one eigenvalue is smaller than $1 \forall k$. As none of the three values of τ are in the critical regions there is an unambiguous filling scheme, and the heuristic model predicts one edge state pr. unit cell, in agreement with the plots.

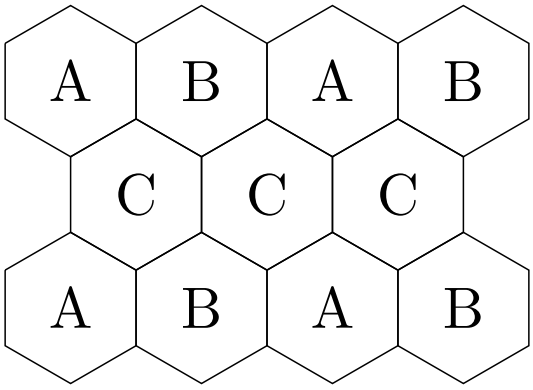

(a) The reduced lattice of (6,6,12)-graphyne can also be seen as a set of interlocking Benzene rings made up of different hopping elements.

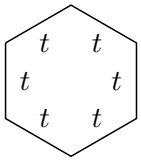

(b) Type A.

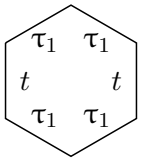

(c) Type B.

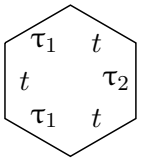

(d) Type C.

Figure 5.12: In (6,6,12)-graphyne, we deal with three types of benzene rings.

If $\mathbf{q}$ is small the eigenstate of the system is still a superpostion of the two sublattices' Dirac points, such that $h\left|\psi\right\rangle = h\left(\alpha\left|\uparrow\right\rangle + \beta\left|\downarrow\right\rangle\right)\otimes\left|\phi\right\rangle = E\left(\alpha\left|\uparrow\right\rangle + \beta\left|\downarrow\right\rangle\right)\otimes\left|\phi\right\rangle$. $h(\mathbf{k}^*)$ drops out as $h_{B/R}(\mathbf{k}^*)\left|\phi\right\rangle = 0$.

$$h^{(1)}\left|\psi\right\rangle = \alpha\left|\downarrow\right\rangle\otimes\left(h_1^{(1)}\left|\phi\right\rangle + ih_2^{(1)}\left|\phi\right\rangle\right) + \beta\left|\downarrow\right\rangle\otimes\left(h_1^{(1)}\left|\phi\right\rangle - ih_2^{(1)}\left|\phi\right\rangle\right) = E\left(\alpha\left|\uparrow\right\rangle + \beta\left|\downarrow\right\rangle\right)\otimes\left|\phi\right\rangle. \quad (5.6.2)$$

Taking the inner product with $\langle\phi|$ on both sides gives us

$$\alpha\left|\downarrow\right\rangle\left(d_1\left(\mathbf{q}\right) + id_2\left(\mathbf{q}\right)\right) + \beta\left|\uparrow\right\rangle\left(d_1\left(\mathbf{q}\right) - id_2\left(\mathbf{q}\right)\right) = E\left(\alpha\left|\uparrow\right\rangle + \beta\left|\downarrow\right\rangle\right), \quad (5.6.3)$$

where $d_i = \langle\phi|h_i^{(1)}|\phi\rangle$. As $h_i^{(1)}$ is first order in $\mathbf{q}$, $d_1\left(\mathbf{q}\right)$ and $d_2\left(\mathbf{q}\right)$ are also linear in $\mathbf{q}$ and can as such be written, $d_i\left(\mathbf{q}\right) = \boldsymbol{v}_i\cdot\mathbf{q}$, where $\boldsymbol{v}_i$ is some real valued vector. Taking the inner product with both $\langle\uparrow|$ and $|\downarrow\rangle$ on both sides of (5.6.3), gives us a matrix equation

$$\begin{pmatrix} 0 & \boldsymbol{v}_1\cdot\mathbf{q} - i\boldsymbol{v}_2\cdot\mathbf{q} \\ \boldsymbol{v}_1\cdot\mathbf{q} + i\boldsymbol{v}_2\cdot\mathbf{q} & 0 \end{pmatrix}\begin{pmatrix}\alpha\\ \beta\end{pmatrix} = E\begin{pmatrix}\alpha\\ \beta\end{pmatrix}. \quad (5.6.4)$$

The eigenvectors and eigenvalues are easily found

$$E = \pm\sqrt{\left(\boldsymbol{v_1}\cdot\mathbf{q}\right)^2 + \left(\boldsymbol{v_2}\cdot\mathbf{q}\right)^2}, \quad (5.6.5)$$

$$\psi_- = \frac{1}{\sqrt{2}}\begin{pmatrix}\left(-\boldsymbol{v_1}\cdot\mathbf{q} + i\boldsymbol{v_2}\cdot\mathbf{q}\right)/E\\ 1\end{pmatrix} = \frac{1}{\sqrt{2}}\begin{pmatrix}\left(-\boldsymbol{v}^*\cdot\mathbf{q}\right)/E\\ 1\end{pmatrix}, \quad (5.6.6a)$$

$$\psi_+ = \frac{1}{\sqrt{2}} \begin{pmatrix} 1 \\ (\boldsymbol{v_1} \cdot \mathbf{q} + i\boldsymbol{v_2} \cdot \mathbf{q})/E \end{pmatrix} = \frac{1}{\sqrt{2}} \begin{pmatrix} 1 \\ (\boldsymbol{v} \cdot \mathbf{q})/E \end{pmatrix}, \tag{5.6.6b}$$

where $\boldsymbol{v} = \boldsymbol{v}_1 + i\boldsymbol{v}_2$. We follow the convention of calculating the Berry phase in the lower band [21]

$$\gamma = -\mathrm{Im} \oint_C d\mathbf{q} \cdot \langle \psi_- | \nabla_{\mathbf{q}} | \psi_- \rangle = -\frac{1}{2} \mathrm{Im} \oint_C d\mathbf{q} \cdot \left(\frac{-\boldsymbol{v} \cdot \mathbf{q}}{E} \nabla_{\mathbf{q}} \left(\frac{-\boldsymbol{v}^* \cdot \mathbf{q}}{E} \right) \right). \tag{5.6.7}$$

As the integral can be performed over any closed contour enclosing the Dirac point, we are free to pick a contour on which $\nabla_{\mathbf{q}} E = 0$. Rearranging the dot products gives us

$$\gamma = -\frac{1}{2E^2} \mathrm{Im} \oint_C (\boldsymbol{v} \cdot \mathbf{q}) \boldsymbol{v}^* = -\frac{1}{2E^2} \frac{1}{2i} \oint_C d\mathbf{q} \cdot \left[\boldsymbol{v}^* (\mathbf{q} \cdot \boldsymbol{v}) - \boldsymbol{v} (\mathbf{q} \boldsymbol{v}^*) \right]. \tag{5.6.8}$$

Using the two vector identities $\mathbf{b}(\mathbf{a} \cdot \mathbf{c}) - \mathbf{c}(\mathbf{a} \cdot \mathbf{b}) = \mathbf{a} \times (\mathbf{b} \times \mathbf{c})$ and $\mathbf{a} \cdot (\mathbf{b} \times \mathbf{c}) = \mathbf{c} \cdot (\mathbf{a} \times \mathbf{b})$, we can rewrite the integrand

$$\boldsymbol{v}^* (\mathbf{q} \cdot \boldsymbol{v}) - \boldsymbol{v} (\mathbf{q} \cdot \boldsymbol{v}^*) = \mathbf{q} \times (\boldsymbol{v}^* \times \boldsymbol{v}) \Rightarrow d\mathbf{q} \cdot (\mathbf{q} \times (\boldsymbol{v}^* \times \boldsymbol{v})) = (\boldsymbol{v}^* \times \boldsymbol{v}) \cdot (d\mathbf{q} \times \mathbf{q}). \tag{5.6.9}$$

For any vector $\boldsymbol{v}^* \times \boldsymbol{v} = 2i\mathrm{Re}(\boldsymbol{v}) \times \mathrm{Im}(\boldsymbol{v})$. Inserting this in (5.6.8) yields

$$\gamma = -\frac{1}{2E^2} (\boldsymbol{v}_1 \times \boldsymbol{v}_2) \cdot \oint_C d\mathbf{q} \times \mathbf{q}. \tag{5.6.10}$$

$d\mathbf{q} \times \mathbf{q} = (0, 0, dq_x q_y - dq_y q_x)$, so we can evaluate the integral with Stokes' theorem

$$\oint_C (q_y dx - q_x dy) = -\iint_D \left(\partial_{q_x} q_x + \partial_{q_y} q_y \right) dq_x dq_y = -2 \iint_D dq_x dq_y = -2A, \tag{5.6.11}$$

where D is the region enclosed by the contour C. A is just the total area of the region D. The Berry phase is then

$$\gamma = \frac{1}{E^2} (\boldsymbol{v_1} \times \boldsymbol{v_2}) \cdot (A\hat{\mathbf{z}}). \tag{5.6.12}$$

Since $E^2 = (v_{1x} q_x + v_{1y} q_y)^2 + (v_{2x} q_x + v_{2y} q_y)^2$, which defines the contour, contains cross terms $\propto q_x q_y$, we make a change of coordinates to get an elliptic equation. The elliptic equation is $x^2/a^2 + y^2/b^2 = 1$, where a and b are the semi-minor and semi-major axes. Defining the reciprocal lattice vectors, $\mathbf{b}_1$ and $\mathbf{b}_2$ by $\boldsymbol{v}_i \cdot \mathbf{b}_j = \delta_{ij}$, $\mathbf{q}$ can be expressed as a linear combination of these two, $\mathbf{q} = x\mathbf{b}_1 + y\mathbf{b}_2$. As $q_x = x b_{1x} + y b_{2x}$ and $q_y = x b_{1y} + y b_{2y}$, the Jacobian determinant is $b_{1x} b_{2y} - b_{1y} b_{2x}$. The integral $\iint_D dq_x dq_y$ is then

$$\iint_D dq_x dq_y = \iint_{\tilde{D}} |\det(J)| dx dy = |b_{1x} b_{2y} - b_{1y} b_{2x}| \iint_{\tilde{D}} dx dy. \tag{5.6.13}$$

$E^2 = (\boldsymbol{v}_1 \cdot \mathbf{q})^2 + (\boldsymbol{v}_2 \cdot \mathbf{q})^2 = x^2 + y^2$ so the region $\tilde{D}$ defined in the (x, y) coordinate system is just a circle of radius E and $\iint_{\tilde{D}} dx dy = \pi E^2$. The norm of the Jacobian determinant $|b_{1x} b_{2y} - b_{1y} b_{2x}|$ is the length of $\mathbf{b}_1 \times \mathbf{b}_2$ (both $\boldsymbol{v}_1 \times \boldsymbol{v}_2$ and $\mathbf{b}_1 \times \mathbf{b}_2$ lie entirely along the $\hat{\mathbf{z}}$-axis). The quadruple product $(\boldsymbol{v}_1 \times \boldsymbol{v}_2) \cdot (\mathbf{b}_1 \times \mathbf{b}_2) = (\boldsymbol{v}_2 \cdot \mathbf{b}_1)(\boldsymbol{v}_2 \cdot \mathbf{b}_2) - (\boldsymbol{v}_1 \cdot \mathbf{b}_2)(\boldsymbol{v}_2 \cdot \mathbf{b}_2) = 1$, so that $|\mathbf{b}_1 \times \mathbf{b}_2| = 1/|\boldsymbol{v}_1 \times \boldsymbol{v}_2|$, yielding a final expression for the Berry phase

$$\gamma = \pi \frac{\boldsymbol{v}_1 \times \boldsymbol{v}_2}{|\boldsymbol{v}_1 \times \boldsymbol{v}_2|} \cdot \hat{\mathbf{z}}. \tag{5.6.14}$$

The vector $(\boldsymbol{v}_1 \times \boldsymbol{v}_2)/|\boldsymbol{v}_1 \times \boldsymbol{v}_2|$ is a unit vector pointing along the positive or negative $\hat{\mathbf{z}}$-axis, depending

on the handedness of the vectors $\boldsymbol{v}_1$ and $\boldsymbol{v}_2$ (i.e. if they span a right-handed or left-handed coordinate system). In the derivation we assumed that the real space component of the eigenstate, $|\phi\rangle$, was a zero-energy eigenstate of both $h_B(\mathbf{k}^*)$ and $h_R(\mathbf{k}^*)$. If this is not the case, the derivation must be altered and the vectors $\boldsymbol{v}_1$ and $\boldsymbol{v}_2$ defined differently, as done in appendix G.

5.6.1 Berry phase in β- and γ-graphyne

In β- and γ-graphyne, the two Dirac points lie at $\mathbf{k}'_\pm = \left(0, \frac{2}{3\sqrt{3}}\cos^{-1}\left(\frac{1}{\tau}+\frac{\tau^2}{2}-\frac{1}{2}\right)\right)$. In this case (5.2.2a) and (5.2.2b) have different zero-energy eigenvectors, so $\boldsymbol{v}_1$ and $\boldsymbol{v}_2$ must be defined as in appendix G. The eigenvectors *can* be found analytically, but as they are rather cumbersome expressions, we abstain from writing them and just state the matrices $h_x^{(1)}$ and $h_y^{(1)}$ and give the result for the Berry phase

$$h_x^{(1)} = \tau \begin{pmatrix} \sin(\mathbf{k}^*\cdot a_2)\left(\frac{3}{2}q_x + \frac{3\sqrt{3}}{2}q_y\right) & 0 & 0 \\ 0 & 0 & 0 \\ 0 & 0 & -\sin(\mathbf{k}^*\cdot \mathbf{a}_1\left(\frac{3}{2}q_x - \frac{3\sqrt{3}}{2}\right) \end{pmatrix}, \tag{5.6.15a}$$

$$h_y^{(1)} = \tau \begin{pmatrix} \cos(\mathbf{k}^*\cdot \mathbf{a}_2)\left(\frac{3}{2}q_x + \frac{3\sqrt{3}}{2}q_y\right) & 0 & 0 \\ 0 & -3q_x & 0 \\ 0 & 0 & \cos(\mathbf{k}^*\cdot \mathbf{a}_1)\left(\frac{3}{2}q_x - \frac{3\sqrt{3}}{2}q_y\right) \end{pmatrix}. \tag{5.6.15b}$$

The Berry phase for $\mathbf{k}'_+$ is $\gamma_+ = -\pi$ and $\gamma_- = \pi$. The two extremes of τ that give Dirac points, $\tau = -2$ and $\tau = -1$ correspond to two points in the Brillouin zone where the Dirac points meet and annihilate. At $\tau = -1$, they meet at $\pm\mathbf{M}$ and at $\tau = -2$, they meet at $\mathbf{\Gamma} = (0,0)$. We discuss the annihilation of Dirac points more below.

5.6.2 Berry phase in (6,6,12)-graphyne

In (6,6,12)-graphyne there can be up to four Dirac points $\mathbf{K}_\pm = (\pm k^*_{x1}, 0)$ and $\mathbf{K}'_\pm = (\pm k^*_{x2}, \pi)$, coming in mirror symmetric pairs. k^*_{1x} and k^*_{2x} are defined by (5.3.3) and (5.3.9). We can calculate the Berry phase in each of the Dirac points. At both the $k_y = 0$ and $k_y = \pi$ Dirac points, the Hamiltonians h_B and h_R, given in (5.3.1), have the same zero-energy eigenvectors, so the definition of $\boldsymbol{v}_1$ and $\boldsymbol{v}_2$ in the above section is relevant.

We start with the $\mathbf{K}_+$ Dirac point. The zero-energy eigenvector can be found analytically for specific values of either τ_1 or τ_2. If we set $\tau_1 = -1$ (this is not the value used to calculate the band structure, but the vertical line it defines slices through the same region of the phase diagram), it is

$$|\phi\rangle \doteq \frac{1}{\sqrt{5-\tau_2}} \begin{pmatrix} 1 \\ 1-\frac{\tau_2}{2} - i\sqrt{1-\frac{\tau_2^2}{4}} \\ -\frac{\tau_2}{2} - i\sqrt{1-\frac{\tau_2^2}{4}} \\ 1 \end{pmatrix}, \tag{5.6.16}$$

and the first order correction matrices h_x and h_y are

$$h_x^{(1)}(q_x, q_y) = \begin{pmatrix} 0 & 0 & 0 & -ie^{ik_{x1}^* q_x} \\ 0 & 0 & 0 & 0 \\ 0 & 0 & 0 & 0 \\ ie^{-ik_{x1}^* q_x} & 0 & 0 & 0 \end{pmatrix}, \tag{5.6.17a}$$

$$h_y^{(1)}(q_x, q_y) = \begin{pmatrix} -q_y & 0 & 0 & 0 \\ 0 & 0 & 0 & 0 \\ 0 & 0 & -q_y & 0 \\ 0 & 0 & 0 & 0 \end{pmatrix}. \tag{5.6.17b}$$

The vectors $\boldsymbol{v}_1$ and $\boldsymbol{v}_2$ are defined through the matrix elements $\langle\phi|h_x^{(1)}(q_x, q_y)|\phi\rangle$ and $\langle\phi|h_y^{(1)}(q_x, q_y)|\phi\rangle$ and they are

$$\boldsymbol{v}_1 = \frac{1}{5 - \tau_2} \begin{pmatrix} 2\sqrt{1 - \frac{\tau_2^2}{4}} \\ 0 \end{pmatrix}, \tag{5.6.18a}$$

$$\boldsymbol{v}_2 = \frac{1}{5 - \tau_2} \begin{pmatrix} 0 \\ -2 \end{pmatrix}. \tag{5.6.18b}$$

$\boldsymbol{v}_1$ lies along the positive x-axis for all relevant τ_2, while $\boldsymbol{v}_2$ lies along the negative y-axis, giving a Berry phase $\gamma = -\pi$. For the partner, $\mathbf{K}_-$, the sign in the exponent of $\left(h_x^{(1)}\right)_{14}$ and $\left(h_x^{(1)}\right)_{41}$ changes and the eigenvector φ in (5.6.16) is conjugated. The result is $v_1 \to -\boldsymbol{v}_1$, while $\boldsymbol{v}_2$ is unchanged. The Berry phase at $\mathbf{K}_-$ is then $\gamma = \pi$.

At $\mathbf{K}'_+$, the eigenvector is hard to calculate analytically (since $k_{x2}^* = \cos^{-1}\left(\frac{1}{2}\left[4 + 3\tau_2\right]\right)$ is a harder expression to work with), so instead we just evaluate it numerically. We get $\gamma_\pm = \pm\pi$ for $\mathbf{K}'_\pm$. We see that both $\mathbf{K}_\pm$ and $\mathbf{K}'_\pm$ have opposite Berry phases. As argued in Ref. [10], this means that in order to open a gap (either on the $k_y = 0$ or $k_y = \pi$ line), the $\mathbf{K}_\pm$ or $\mathbf{K}_\pm$ points must be brought together to annihilate with each other. This can happen in two ways: either they come together at $k_x = 0$, which for $\mathbf{K}_\pm$ happens when

$$\frac{\tau_2 - 2 + 2\tau_1^2 - 2\tau_1^2\tau 2}{2\tau_1^2} = 1 \quad \Rightarrow \quad \tau_2 = \frac{2}{1 - 2\tau_1^2}, \tag{5.6.19}$$

which is the lower boundary of the red region in the phase space. They can also merge at $k_x = \pm\pi$, since they are equivalent points in the Brillouin zone. This happens when

$$\frac{\tau_2 - 2 + 2\tau_1^2 - 2\tau_1^2\tau 2}{2\tau_1^2} = -1 \quad \Rightarrow \quad \tau_2 = 2, \tag{5.6.20}$$

which is the upper boundary. The boundaries of the blue region also correspond to the $k_x = 0$ and $k_x = \pm\pi$ mergers. However both points are fixed on the horizontal lines $k_y = 0$, $k_y = \pi$. It is only if we introduce next nearest neighbour hopping that the Dirac points move away from these lines. Looking at the reduced lattice in Figure 5.6, next nearest hopping can go through four combinations of nearest neighbour hops, so we could in principle introduce four next nearest hoppings, but for simplicity we introduce just one. Next nearest neighbour hopping adds a σ_0 and σ_3 term to the Hamiltonian in

(5.2.1), as it connects sites on the same sublattice:

$$h = \frac{1}{2}\left[\sigma_0 \otimes \left(h_R^{(nnn)} + h_B^{(nnn)}\right) + \sigma_1 \otimes (h_B + h_R) + \sigma_2 \otimes (ih_B - ih_R) + \sigma_3 \otimes \left(h_R^{(nnn)} - h_B^{(nnn)}\right)\right], \tag{5.6.21}$$

where

$$h_B^{(nnn)} = -T \begin{pmatrix} 0 & 1+\mathrm{e}^{ik_y} & 1+\mathrm{e}^{ik_x} & \mathrm{e}^{i(k_x+k_y)}+\mathrm{e}^{ik_x} \\ 1+\mathrm{e}^{-ik_y} & 0 & 1+\mathrm{e}^{-ik_y} & 1+\mathrm{e}^{ik_x} \\ 1+\mathrm{e}^{-ik_x} & 1+\mathrm{e}^{ik_y} & 0 & 1+\mathrm{e}^{-ik_y} \\ 1\mathrm{e}^{-i(k_x+k_y)} & 1+\mathrm{e}^{-ik_x} & 1+\mathrm{e}^{-ik_y} & 0 \end{pmatrix}. \tag{5.6.22}$$

As above, $h_R^{(nnn)}(k_x, k_y) = h_B^{(nnn)}(k_x, -k_y)$. Implementing this numerically we can see the effect next nearest neighbour hopping has on the band structure. We see in Figure 5.13 how the band structure changes for increasing next nearest neighbour hopping strength. The Fermi level is moved below zero, and the $\mathbf{K}$ and $\mathbf{K}'$ Dirac points (whether they are in fact Dirac points is up for debate, seeing as the spectrum is not linear and the states are not sublattice polarised) move towards each other and annihilate.

5.7 Conclusion

We have in this chapter introduced graphynes, carbon based materials similar to graphene containing sp-hybridised atoms. By integrating out the sp-hybridised atoms of different graphynes, we attained graphene-like models with more parameters than in pristine graphene. These extra parameters allowed us to explore the nature of Dirac points and edge states, and the relation between them. When applying the heuristic model of chapters 3 and 4 to graphynes, we saw that Dirac points can be seen as a result of the ambiguity present when constructing the many-body ground state, like in the SSH model. When we introduced the transfer matrix, the relation between edge states and Dirac points was made clear, namely that the Dirac points exist as the boundary between the phases with and without edge states. Finally, we calculated the Berry phase for both β/γ-graphyne and for (6,6,12)-graphyne. In both cases we demonstrated that when a gap opens in the band structure, two Dirac points of opposite Berry phases come together to annihilate with each other, and in (6,6,12)-graphyne we saw how next nearest neighbour hopping induced a different gap opening.

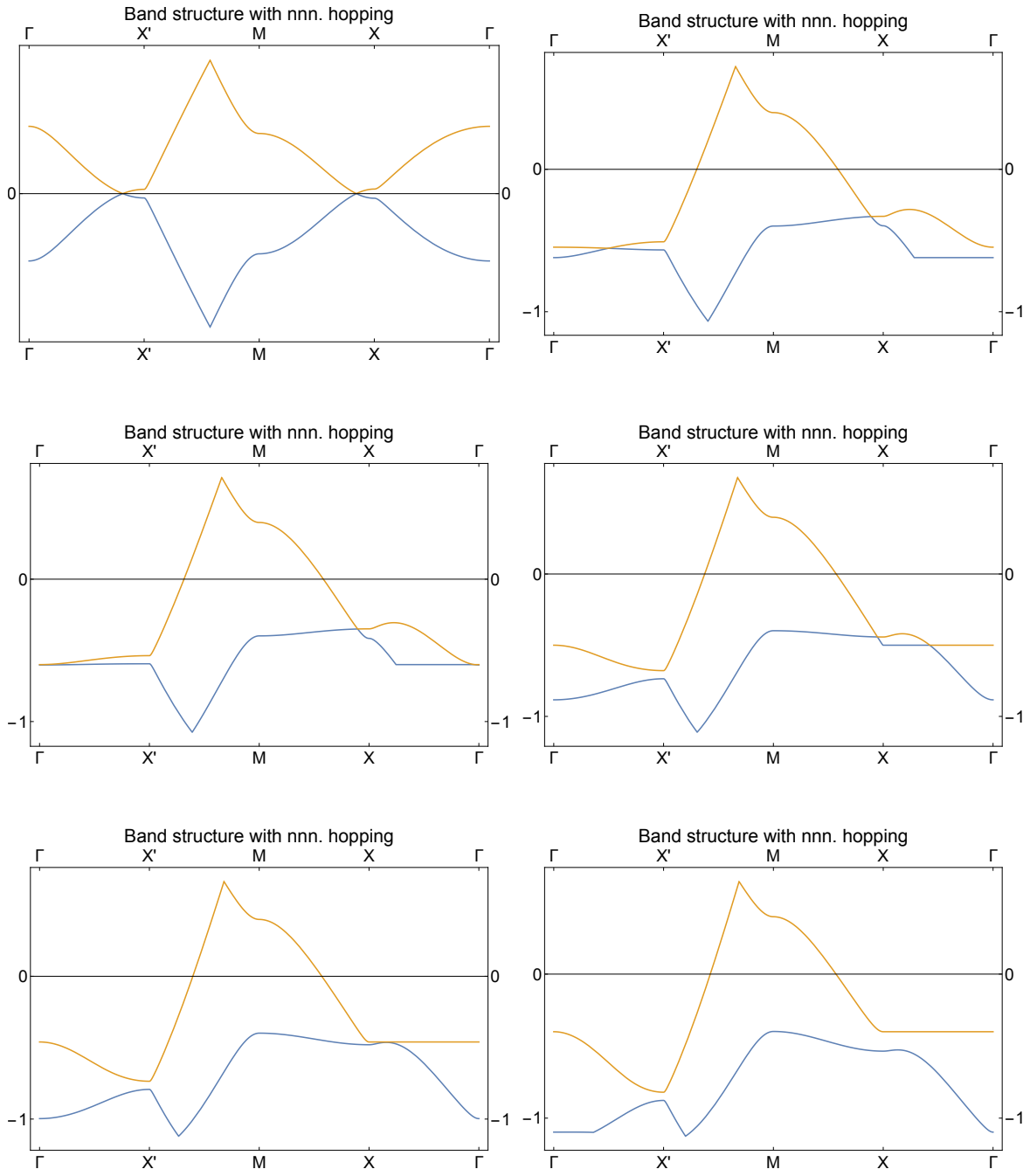

Figure 5.13: Band structure for next nearest hopping ampltiude $T = 0$, 0.19, 0.20, 0.25, 0.27, 0.30. The Dirac points are moved away from the $k_y = 0$ and $k_y = \pi$ lines. For strong enough T, the two points come together on the $X \to \Gamma$ line and annihilate to open a gap.

Chapter 6

Conclusion and outlook

In this thesis we have explored Dirac points and edge states in two-dimensional materials. The results of chapter 3 laid the groundwork for the mathematical formalism we adopted, the transfer matrix. More importantly, we introduced the heuristic model that uses concepts from chemistry, double bonds and aromatic structures, to describe carbon-based compounds. This model was first put to use to calculate the edge state density, along the zigzag edge of graphene, and it gave an intuitive explanation why the zigzag edge is magnetic. This was explained by the fact that the unpaired electrons, which are found on every third site on the edge, align their spins to minimise the Coulomb repulsion. In chapter 4, the model was put to use on specific graphene nanoribbons, and was found to not only provide a correct prediction of the number of edge states, but also an explanation of why Dirac points exist in GNRs. In chapter 5 the model was tested, by applying it to graphynes, which are less intuitive materials. In graphynes there are multiple hopping parameters in the Hamiltonian, making it harder to apply the heuristic model. It was still applicable, and the discussion, especially on β- and γ-graphyne, gave a deeper understanding of Dirac points within this model. Alongside the heuristic model, the transfer matrix was a powerful tool that served as mathematical verification of the results predicted with the heuristic model. The transfer matrix showed how Dirac points and edge states are connected. In a given model, for an edge state to be added to or removed from the system, a gap in the band structure must be opened or closed. This followed directly from the zero-energy transfer matrix, which contains information about both Dirac points and edge states.

In the entire thesis, the heuristic model remained purely heuristic, and we did not once put any mathematics behind it. Its predictions were of course confirmed, but the model itself was not mathematically well formulated. In the unpublished Ref. [15], the concepts that laid the groundwork for the heuristic model are mathematically reasoned and fully explained. However, this is in an interacting theory, wherein concepts such as Bloch waves and band structure are not well defined. Obviously, taking interactions into account only improves a theory, but having a mathematical formulation of the non-interacting heuristic model would be immensely useful. This might well be able to explain the different phases we found for (6,6,12)-graphyne in chapter 5, and provide a similar phase diagram that our band structure analysis did.

Bibliography

[1] K. S. Novoselov et al. "Electric Field Effect in Atomically Thin Carbon Films". In: *Science* 5696 (Oct. 2004).

[2] Ting Cao, Fangzhou Zhao, and Steven G. Louie. "Topological Phases in Graphene Nanoribbons: Junction States, Spin Centers, and Quantum Spin Chains". In: *Phys. Rev. Lett.* 119 (7 Aug. 2017).

[3] K. S. Novoselov et al. "Two-dimensional gas of massless Dirac fermions in graphene". In: *Nature* 438.7065 (2005).

[4] N. M. R. Peres. "Colloquium: The transport properties of graphene: An introduction". In: *Reviews of Modern Physics* 82.3 (Sept. 2010).

[5] 1967- Blundell Stephen. *Magnetism in condensed matter*. Oxford University Press, 2001.

[6] N.W. Ashcroft and N.D. Mermin. *Solid State Physics*. Saunders College Publishing, 2011.

[7] Alexander Altland and Ben D. Simons. *Condensed Matter Field Theory*. 2nd ed. Cambridge University Press, 2010.

[8] M. V. Berry. "Quantal Phase Factors Accompanying Adiabatic Changes". In: *Royal Society* 392.1802 (1984).

[9] J. J. Sakurai and Jim Napolitano. *Modern Quantum Mechanics*. 2nd ed. Cambridge University Press, 2017.

[10] B. ANDREI BERNEVIG and Taylor L. Hughes. *Topological Insulators and Topological Superconductors*. STU - Student edition. Princeton University Press, 2013.

[11] János K. Asbóth, László Oroszlány, and András Pályi. "A Short Course on Topological Insulators". In: *Lecture Notes in Physics* (2016).

[12] Nakada, Fujita, and Dresselhaus. "Edge state in graphene ribbons: Nanometer size effect and edge shape dependence." In: *Physical review. B, Condensed matter* 54 24 (1996).

[13] J. Clayden, N. Greeves, and S. Warren. *Organic Chemistry*. OUP Oxford, 2012.

[14] Dean Moldovan, Miša Anelković, and Francois Peeters. *pybinding v0.9.5: a Python package for tight- binding calculations*. Version v0.9.5. Aug. 2020.

[15] Per Hedegård. "Neoclassical valence bond theory". In: *Unpublished* ().

[16] Ricardo Ortiz et al. "Exchange Rules for Diradical -Conjugated Hydrocarbons". In: *Nano Letters* 19.9 (Sept. 2019).

[17] Nannan Han et al. "Possible Formation of Graphyne on Transition Metal Surfaces: A Competition with Graphene from the Chemical Potential Point of View". In: *The Journal of Physical Chemistry C* 120.27 (July 2016).

[18] Martin Drøhse Kilde et al. "Synthesis of radiaannulene oligomers to model the elusive carbon allotrope 6,6,12-graphyne". In: *Nature Communications* 10.1 (2019).

[19] Bog G. Kim and Hyoung Joon Choi. "Graphyne: Hexagonal network of carbon with versatile Dirac cones". In: *Phys. Rev. B* 86 (11 Sept. 2012).

[20] Zhe Liu et al. "A simple tight-binding model for typical graphyne structures". In: *New Journal of Physics* 14.11 (2012).

[21] David Vanderbilt. *Berry Phases in Electronic Structure Theory: Electric Polarization, Orbital Magnetization and Topological Insulators*. Cambridge University Press, 2018.

[22] George B. Arfken, Hans J. Weber, and Frank E. Harris. "Mathematical Methods for Physicists (Seventh Edition)". In: Boston: Academic Press, 2013.

[23] K. F. Riley. *Mathematical Methods for the Physical Sciences: An Informal Treatment for Students of Physics and Engineering*. Cambridge University Press, 1974.

[24] *Eigenvalues and eigenvectors of the second-order derivative*. https://en.wikipedia.org/wiki/Eigenvalues_and_eigenvectors_of_the_second_derivative. Accessed: 2020-12-30.

Appendices

Appendix A

Neoclassical valence bond theory

In this appendix we represent a simple version of Neoclassical valence bond theory (NVB). NVB is a way of describing resonance structures, in which the quantum mechanical basis states are different configurations of single, double, and triple bonds. For example, the two configurations of polyacetylene, $(C_2H_2)_3$ shown in Figure 3.5 are in NVB two basis states used to calculate the exact many-body ground state. We start by considering the Hubbard model

$$H = -t \sum_{\langle ij \rangle} \left(c_i^\dagger c_j + c_j^\dagger c_i \right) + U \sum_i n_{i\uparrow} n_{i\downarrow} = T + V, \tag{A.1}$$

which contains the standard hopping term of the tight-binding model which we label T, as well as a penalty term U for doubly occupied orbitals which we label V. We now introduce the projection operators P and Q. P projects into states with only singly occupied orbitals, while Q projects into states with doubly occupied orbitals. The effective Hamiltonian on the P subspace is

$$H_P = PHP + PHQ \frac{1}{E - QHQ} QHP, \tag{A.2}$$

as shown in chapter 3. The first term PHP is in this case zero, since H brings a P state into the Q subspace, which P subsequently kills. The second term can be written as

$$PHQ \frac{1}{E - QHQ} QHP = P \left[\frac{1}{E - U} TQT \right] P. \tag{A.3}$$

We have replaced $(E - QHQ)^{-1}$ with the scalar $E - U$, since QHP brings a P state into the Q subspace, and H just reads of the double occupancy. The effective Hamiltonian naturally begins and ends in the P subspace, but allows for transitions in between. Writing the spin operators as second quantized operators

$$S_i^z = \frac{1}{2} \left(c_{i\uparrow}^\dagger c_{i\uparrow} - c_{i\downarrow}^\dagger c_{i\downarrow} \right), \tag{A.4a}$$

$$S_i^+ = c_{i\uparrow}^\dagger c_{i\downarrow}, \tag{A.4b}$$

$$S_i^- = c_{i\downarrow}^\dagger c_{i\uparrow}, \tag{A.4c}$$

the effective Hamiltonian becomes

$$H_P = P\Big[\sum_{\langle ij\rangle}\frac{t^2}{E-U}\sum_{\sigma\sigma'}(c^\dagger_{i\sigma}c_{j\sigma}c^\dagger_{j\sigma'}c_{i\sigma'}+c^\dagger_{j\sigma}c_{i\sigma}c^\dagger_{i\sigma'}c_{j\sigma'})\Big]P$$

$$= P\Big[\sum_{\langle ij\rangle}\frac{t^2}{E-U}\sum_{\sigma\sigma'}\{\delta_{\sigma\sigma'}(c^\dagger_{i\sigma}c_{i\sigma'}+c^\dagger_{j\sigma}c_{j\sigma'})-c^\dagger_{i\sigma}c_{i\sigma'}c^\dagger_{j\sigma'}c_{j\sigma}-c^\dagger_{j\sigma}c_{j\sigma'}c^\dagger_{i\sigma'}c_{i\sigma}\}\Big]P$$

$$= P\left[\sum_{\langle ij\rangle}\frac{2t^2}{E-U}\left(\frac{1}{2}-S^+_iS^-_j-S^-_iS^+_j-2S^z_iS^z_j\right)\right]P = -\frac{4t^2}{E-U}\sum_{\langle ij\rangle}\left(\hat{\mathbf{S}}_i\cdot\hat{\mathbf{S}}_j-\frac{1}{4}\right)$$

$$= J\sum_{\langle ij\rangle}\left(\hat{\mathbf{S}}_i\cdot\hat{\mathbf{S}}_j-\frac{1}{4}\right), \tag{A.5}$$

which is just the Heisenberg Hamiltonian with exchange coupling $J = -4t^2/(E-U)$. As $E < U$, $J > 0$, and an antiferromagnetic coupling is preferred. This is not at all surprising, and is exactly what we have been assuming in our heuristic model, where a double bond represents two electrons occupying the bonding orbital in a singlet configuration. If we have two orbitals, 1 and 2, the singlet state

$$|s\rangle = \frac{1}{\sqrt{2}}\left(|\uparrow_1\downarrow_2\rangle - |\downarrow_1\uparrow_2\rangle\right) = S^\dagger_{12}|0\rangle \tag{A.6}$$

is an eigenstate of $\hat{\mathbf{S}}_1\cdot\hat{\mathbf{S}}_2-\frac{1}{4}$ with eigenvalue $-J$. $S^\dagger_{ij} = \left(c^\dagger_{i\uparrow}c^\dagger_{j\downarrow}-c^\dagger_{i\downarrow}c^\dagger_{j\uparrow}\right)/\sqrt{2}$ is the singlet creation operator. However if there is not a singlet state between orbitals 1 and 2, $\hat{\mathbf{S}}_1\cdot\hat{\mathbf{S}}_2-\frac{1}{4}$ creates a singlet bond between those two orbitals:

$$\left[\mathbf{S}_2\cdot\mathbf{S}_3-\frac{1}{4}\right]$$ 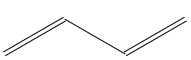 $$= \left[\mathbf{S}_2\cdot\mathbf{S}_3-\frac{1}{4}\right]\frac{1}{2}\left(|\uparrow\downarrow\uparrow\downarrow\rangle - |\uparrow\downarrow\downarrow\uparrow\rangle - |\downarrow\uparrow\uparrow\downarrow\rangle + |\downarrow\uparrow\downarrow\uparrow\rangle\right)$$

$$\left[S^z_2S^z_3+\frac{1}{2}\left(S^+_2S^-_3+S^-_2S^+_3\right)\right]\frac{1}{2}\left(|\uparrow\downarrow\uparrow\downarrow\rangle - |\uparrow\downarrow\downarrow\uparrow\rangle - |\downarrow\uparrow\uparrow\downarrow\rangle + |\downarrow\uparrow\downarrow\uparrow\rangle\right)$$

$$\frac{1}{4}\left(|\uparrow\uparrow\downarrow\downarrow\rangle - |\uparrow\downarrow\uparrow\downarrow\rangle - |\downarrow\uparrow\downarrow\uparrow\rangle + |\downarrow\downarrow\uparrow\uparrow\rangle\right) = \frac{1}{2}$$ 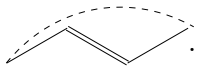 . $$\tag{A.7}$$

The operator $\mathbf{S}_i\cdot\mathbf{S}_j-\frac{1}{4}$ can therefore be seen as a singlet projection operator. If there is already a singlet bond between sites i and j, it returns the eigenvalue $-J$, and if not it creates a state with one. For convention's sake we then define $p_{ij} = -\left(\mathbf{S}_i\cdot\mathbf{S}_j - 1/4\right)$ and H takes the form

$$H = -J\sum_{\langle ij\rangle}p_{ij}. \tag{A.8}$$

If there is a nearest neighbour pair ij, where one of the sites is uncoupled and the other is in a double bond with a third site, the projection operator creates a singlet bond between i and j, and moves the uncoupled spin to the now unbound third site:

$$\left[\mathbf{S}_1 \cdot \mathbf{S}_2 - \frac{1}{4}\right] \quad = \left[\mathbf{S}_1 \cdot \mathbf{S}_2 - \frac{1}{4}\right] \frac{1}{\sqrt{2}} \left(|\uparrow\uparrow\downarrow\rangle - |\uparrow\downarrow\uparrow\rangle\right)$$

$$= \frac{1}{2\sqrt{2}} \left(|\uparrow\downarrow\uparrow\rangle - |\downarrow\uparrow\uparrow\rangle\right) = \frac{1}{2} \quad \Rightarrow \quad p_{12} \quad = -\frac{1}{2} \quad . \tag{A.9}$$

The red circle represents the unparied spin. In order to analyse the coupling between sites of greater separation than nearest neighbours, we expand the term $(E - QHQ)^{-1} = (E - QTQ - QVQ)^{-1}$ in a power series in QTQ

$$\frac{1}{E - QHQ} = \frac{1}{E - QVQ} + \frac{1}{E - QVQ} QTQ \frac{1}{E - QVQ} + \\ \frac{1}{E - QVQ} QTQ \frac{1}{E - QVQ} QTQ \frac{1}{E - QVQ} + \ldots \tag{A.10}$$

This can in fact be seen as an expansion in the number of hops. As each hop gives a factor of $(-t)$, the sign of an exchange between two spins is then directly determined by the number of hops that they must go through to reach each other. As the edge states reside on the same sublattice, they are always connected by an even number of hops. This then gives a *positive* exchange, which is the same as saying that they align their spins to form a magnetic edge.

Appendix B

AGNR band structures

In this appendix we show the band structure for the four smallest odd-numbered zigzag AGNRs, to give confirmation to the results predicted by the heuristic model in Figure 4.5.

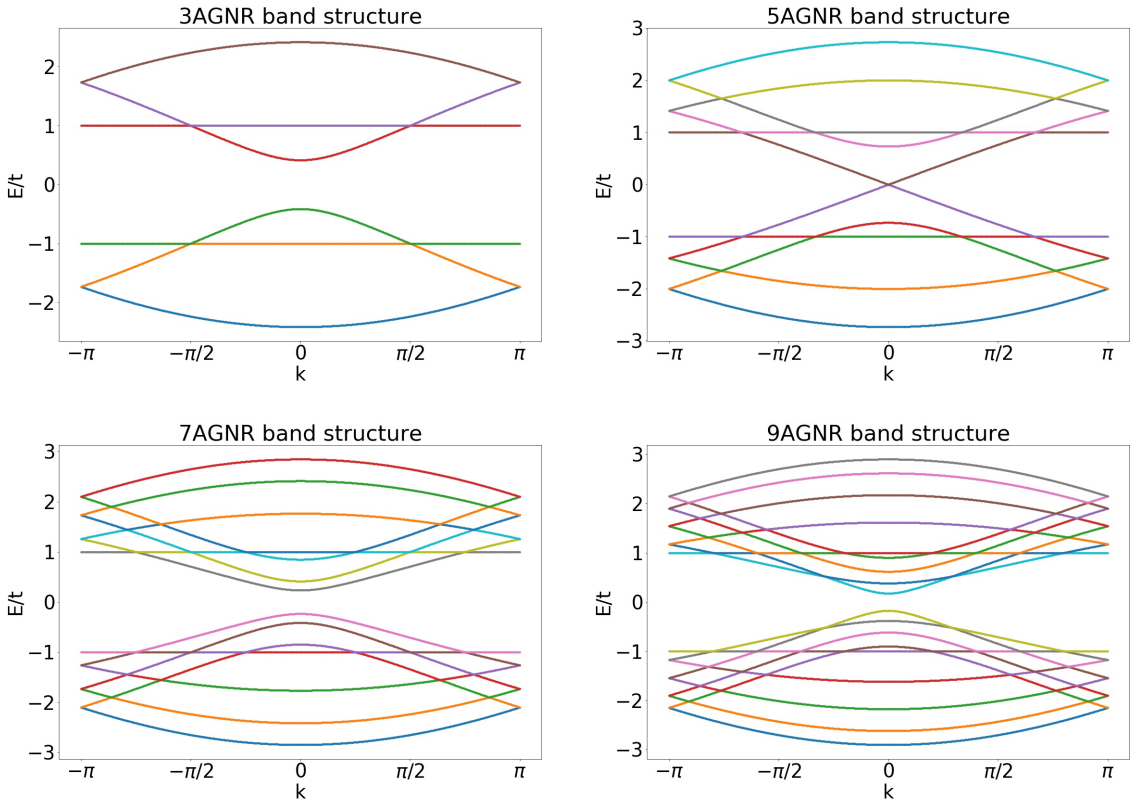

Figure B.1: Band structures of the four smallest zigzag AGNRs with $n =$ Odd rows. The heuristic model predicts that of these, only 5AGNR has a Dirac point, which is indeed what we see.

Appendix C

Eigenvalues of discrete Laplacian

In this appendix we derive the eigenvalues of the discrete Laplacian operator given different boundary conditions. These are useful when decoupling the reduced models of AGNRs into separate SSH chains, as done in chapter 4. There are three different sets of boundary conditions we concern ourselves with. They are known as Dirichlet, Neumann, and mixed Dirichlet-Neumann boundary conditions. We already dealt with the first in chapter 4, as these are just what we would call open boundary conditions. For good measure, and to give an idea of the mathematics, we show them all. The derivations are based on Chebyshev polynomials, which are functions defined by specific recurrence relations [22, 23]. We will derive the eigenvalues following the treatment given in Ref. [24]. The following is slightly mathematical, so the reader can skip to (C.1.6), (C.2.7), and (C.3.10) for the results of this appendix.

C.1 Dirichlet boundary conditions

The eigenvalues of the Laplacian with Dirichlet boundary conditions are used to decouple the reduced model for zigzag AGNRs. The Laplacian can be represented as a square matrix of dimension n:

$$T = \begin{pmatrix} -2 & 1 & & & 0 \\ 1 & -2 & 1 & & \\ & 1 & \ddots & \ddots & \\ & & \ddots & \ddots & 1 \\ 0 & & & 1 & -2 \end{pmatrix}. \tag{C.1.1}$$

The eigenvalues of this will then be the negative eigenvalues of (4.2.5) in chapter 4 (it does not matter whether the off-diagonal elements are ± 1). For an eigenvector $\boldsymbol{v}$ corresponding to an eigenvalue λ, the eigenvalue problem can be stated as

$$v_{k+1} - 2v_k + v_{k-1} = \lambda v_k, \tag{C.1.2}$$

where $v_0 = v_{n+1} = 0$. Up to a normalisation factor, $v_1 = 1$ (we do not actually need to normalise the eigenvectors, but it is good praxis). Rearringing the expression and defining $\alpha = 1 + \lambda/2$, we get a recurrence

$$v_{k+1} = 2\alpha v_k - v_{k-1}. \tag{C.1.3}$$

As every v_k is dependent on α, this recurrence is actually the one defining Chebyshev polynomials of

the second kind [22].

$$U_0(x) = 1, \tag{C.1.4a}$$

$$U_1(x) = 2x, \tag{C.1.4b}$$

$$U_{k+1}(x) = 2xU_k(x) - U_{k-1}(x). \tag{C.1.4c}$$

We see from this that $v_{k+1}(\alpha) = U_k(\alpha)$. As $v_{n+1} = 0$, $U_n(\alpha) = 0$. The eigenvalues of the above given problem are then given by the zeros of $U_n(\alpha)$, which are [22]

$$\alpha_k = \cos\left(\frac{k\pi}{n+1}\right), \, k = 1, \ldots, n, \tag{C.1.5}$$

giving us the eigenvalues

$$\lambda_k = -2 + 2\cos\left(\frac{k\pi}{n+1}\right), \; k = 1, \ldots n. \tag{C.1.6}$$

which is what is given in (4.2.7), up to a sign.

C.2 Neumann boundary conditions

The discrete Laplacian with Neumann boundary conditions is given by the matrix

$$T = \begin{pmatrix} -1 & 1 & & & 0 \\ 1 & -2 & 1 & & \\ & 1 & \ddots & \ddots & \\ & & \ddots & \ddots & 1 \\ 0 & & & 1 & -1 \end{pmatrix}, \tag{C.2.1}$$

which is the one that needs to be diagonalised to decouple the reduced model for zigzag' AGNRs. The eigenvalue problem is now

$$\lambda v_k = \begin{cases} -v_k + v_{k-1}, & k = 1, n, \\ v_k - 2v_k + v_{k-1}, & 1 < k < n. \end{cases}$$

We introduce the dummy variables v_0 and v_{n+1} via the relations $v_0 = v_1$ and $v_{n+1} = v_n$, as well as $w_k = v_{k+1} - v_k$. The point is to achieve a recurrence like the one above, with the same boundary conditions as above. With the variables v_0 and v_{n+1} defined, the expression

$$v_{k+1} - 2v_k + v_{k-1} = \lambda v_k \tag{C.2.3}$$

is now true for all k (instead of only for $1 < k < n$). The l.h.s. can be written in terms of the w_k's, and we get

$$w_k - w_{k-1} = \lambda v_k. \tag{C.2.4}$$

As $v_k = w_{k-1} + v_{k-1}$, the above expression can be cast into the form

$$w_k - w_{k-1} = \lambda\,(w_{k-1} - v_{k-1}) \quad \Rightarrow \quad w_{k+1} = (2+\lambda)\,w_k - w_{k-1}, \tag{C.2.5}$$

which is the same recurrence relation as above, with the boundary conditions $w_0 = w_n = 0$. This gives us $n-1$ eigenvalues of the same form as above

$$\lambda_k = -2 + 2\cos\left(\frac{k\pi}{n}\right),\ k = 1, \ldots, n-1. \tag{C.2.6}$$

Since there are only $n-1$ eigenvalues, there is one left over. The eigenvalue not included in this is $\lambda = 0$, which corresponds to the eigenvector $\boldsymbol{v} = \begin{pmatrix} 1 & 1 \ldots 1 \end{pmatrix}$. Including this, we get

$$\lambda_k = -2 + 2\cos\left(\frac{(k-1)\pi}{n}\right),\ k = 1, \ldots, n. \tag{C.2.7}$$

C.3 Dirichlet-Neumann boundary conditions

The final set of boundary conditions we analyse are a mix between the two above. They are represented by the matrix

$$T = \begin{pmatrix} -2 & 1 & & & 0 \\ 1 & -2 & 1 & & \\ & 1 & \ddots & \ddots & \\ & & \ddots & \ddots & 1 \\ 0 & & & 1 & -1 \end{pmatrix}, \tag{C.3.1}$$

and are relevant for the even numbered zigzag AGNRs in (4.2.10). We are once again working with the recurrence given in (C.1.2). Again, we need to write the recurrence in auxiliary variables that are introduced to ensure (C.1.2) holds for all k. In the two previous cases, we introduced v_0 and v_{n+1} as ways of implementing the boundary conditions. This time around, we define

$$v'_{k+0.5} = v_{k+1} - v_k. \tag{C.3.2}$$

Meaning that the recurrence in (C.1.2) becomes

$$v'_{k+0.5} - v'_{k-0.5} = \lambda v_k \quad \Rightarrow \quad v'_{k+0.5}\,(2+\lambda)\,v'_{k-0.5} - v'_{k-1.5}, \tag{C.3.3}$$

which is the same as for the v_k's. Redefining v_k to include half-integer k's, we now have $2n+1$ elements for which the recurrence (C.1.2) holds. Let us consider the recurrence

$$v_{k+0.5} = 2\beta v_k - v_{k-0.5}, \tag{C.3.4}$$

which holds for integer and half-integer k. If $\beta = 2 + \lambda$ this new recurrence solves our eigenvalue problem. It can be rewritten as

$$v_{k+1} = \left(4\beta^2 - 2\right) v_k - v_{k-1}, \tag{C.3.5}$$

and is the same form as Chebyshev polynomials two degrees separated:

$$U_{k+2}(x) = \left(4x^2 - 2\right) U_k(x) - U_{k-2}(x). \tag{C.3.6}$$

Defining $k' = 2k$, such that k' increases in integer steps, (C.3.5) takes the same form as the above relation for Chebyshev polynomials. Our boundary conditions are $v_{n+0.5} = v_{n+1} - v_n = 0 \Rightarrow v_{2n+1} - v_{2n-1} = 0$ means that

$$U_{2n+1}(\beta) - U_{2n-1}(\beta) = 0. \tag{C.3.7}$$

A formula that relates Chebyshev polynomials of the first and second kind reads [22]

$$U_k(\beta) - U_{k-2}(\beta) = T_k(\beta). \tag{C.3.8}$$

The eigenvalues are therefore the roots of $T_{2n+1}(\beta)$, which are [22]

$$\beta_k = \cos\left(\frac{\pi(k-0.5)}{2n+1}\right),\ k = 1, \ldots, 2n+1. \tag{C.3.9}$$

The eigenvalues that this leads to are degenerate. Sorting away the repeating eigenvalues gives

$$\lambda_k = -2\left(1 + \cos\left(\frac{k\pi}{n+1}\right)\right),\ k = 1, \ldots, n. \tag{C.3.10}$$

Appendix D

Heuristic model and transfer matrix for AGNRs

Here we show that the $n = 4$ and $n = 6$ bearded AGNRs are predicted to have one and two edge states respectively, in the heuristic model and we also derive the zero-energy transfer matrix for bearded, zigzag, and zizag' AGNRs.

D.1 Heuristic model

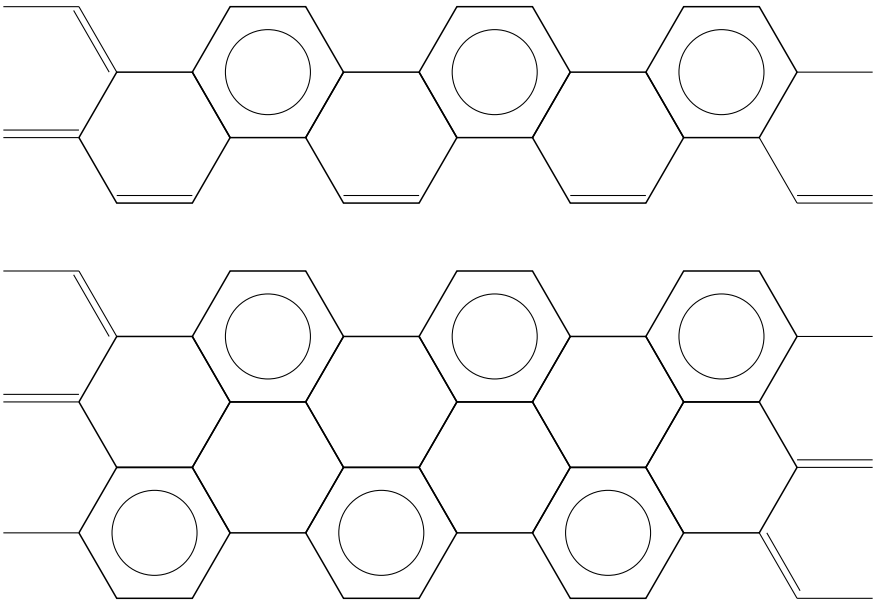

Figure D.1: 4AGNR and 6AGNR with the bearded termination. The heuristic model correctly predicts one and two edge states respectively.

D.2 Bearded AGNR transfer matrix

The transfer matrix is derived by assuming that the amplitude on the sublattice that does not carry the outermost sites is zero. In Figure D.2 below this is the red sublattice on the left edge, so we look

for zero-energy states localised to the blue sublattice (there is a corresponding state localised to the right edge on the red sublattice).

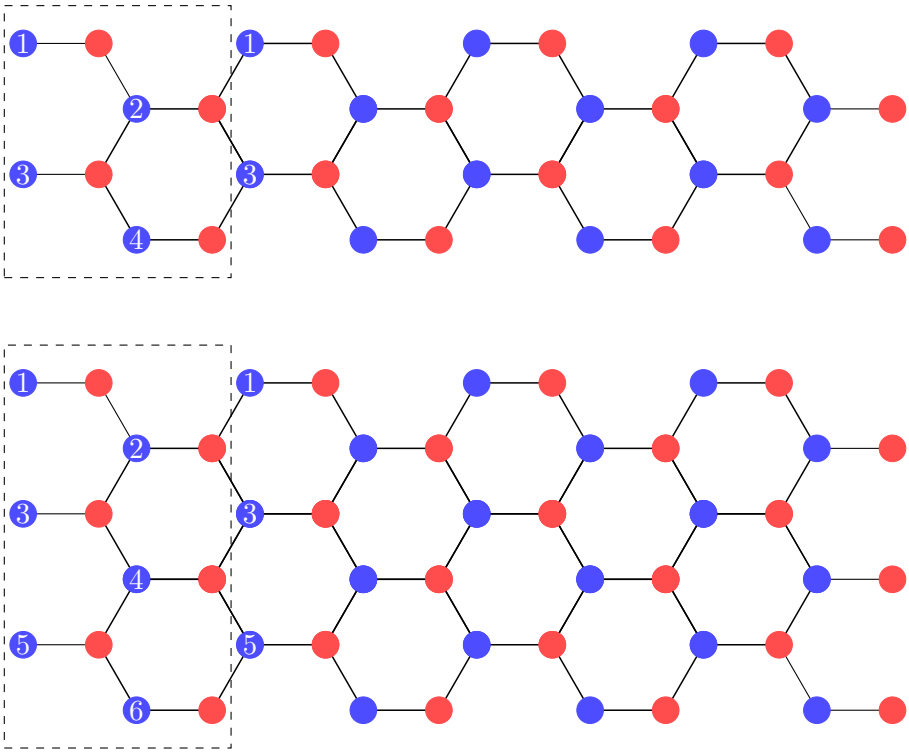

Figure D.2: 4AGNR and 6AGNR with the bearded termination.

Each red site's neighbours interfere destructively, yielding an equation for the three neighbours' ampltidue. For 4AGNR, the equations are

$$c_{1,1} + c_{1,2} = 0, \tag{D.2.1a}$$

$$c_{1,2} + c_{1,3} + c_{1,4} = 0, \tag{D.2.1b}$$

$$c_{1,2} + c_{2,1} + c_{2,3} = 0, \tag{D.2.1c}$$

$$c_{1,4} + c_{2,3} = 0, \tag{D.2.1d}$$

where $c_{i,j}$ is the amplitude on a blue site j in unit cell i. These equations are derived for the first unit cell, but they hold for any unit cell. For 6AGNR the set of equations is

$$c_{1,1} + c_{1,2} = 0, \tag{D.2.2a}$$

$$c_{1,2} + c_{1,3} + c_{1,4} = 0, \tag{D.2.2b}$$

$$c_{1,5} + c_{1,4} + c_{1,6} = 0, \tag{D.2.2c}$$

$$c_{1,2} + c_{2,1} + c_{2,3} = 0, \tag{D.2.2d}$$

$$c_{1,4} + c_{2,3} + c_{2,5} = 0, \tag{D.2.2e}$$

$$c_{1,6} + c_{2,5} = 0. \tag{D.2.2f}$$

The equations can be solved to give an expression for c_{2i}. For 4AGNR it gives

$$\begin{pmatrix} c_{2,1} \\ c_{2,3} \end{pmatrix} = \begin{pmatrix} 1 & -1 \\ -1 & 2 \end{pmatrix} \begin{pmatrix} c_{1,1} \\ c_{1,3} \end{pmatrix} = T \begin{pmatrix} c_{1,1} \\ c_{1,3} \end{pmatrix}, \tag{D.2.3}$$

and for 6AGNR it gives

$$\begin{pmatrix} c_{2,1} \\ c_{2,3} \\ c_{2,5} \end{pmatrix} = \begin{pmatrix} 1 & -1 & 1 \\ -1 & 2 & -2 \\ 1 & -2 & 3 \end{pmatrix} \begin{pmatrix} c_{1,1} \\ c_{1,3} \\ c_{1,5} \end{pmatrix} = T \begin{pmatrix} c_{1,1} \\ c_{1,3} \\ c_{1,5} \end{pmatrix}. \tag{D.2.4}$$

What becomes evident from a few more examples is that the elements of the general transfer matrix are $T_{ij} = \min(i,j)\,(-1)^{i+j}$. It too hard to solve, but as there are other methods to calculate the edge states of bearded AGNRs, we can use this to compare with the results of those methods.

D.3 Zigzag and zigzag' transfer matrices

We now show that the zero-energy transfer matrices of zigzag and zigzag' AGNRs, take the same form as (4.2.5), (4.2.10), and (4.2.14). Like above, we use the fact that zero-energy states are sublattice polarised to derive the transfer matrix. For 5AGNR the equations to be solved are (see Figure D.3)

$$-c_{1,1} - c_{1,2} = 0, \tag{D.3.1a}$$
$$-c_{1,2} - c_{1,4} - c_{1,3} = 0, \tag{D.3.1b}$$
$$-c_{1,4} - c_{1,5} = 0, \tag{D.3.1c}$$
$$-c_{1,1} - c_{1,3} - c_{2,2} = 0, \tag{D.3.1d}$$
$$-c_{1,3} - c_{1,5} - c_{2,4} = 0, \tag{D.3.1e}$$

and for 7AGNR they are

$$-c_{1,1} - c_{1,2} = 0, \tag{D.3.2a}$$
$$-c_{1,2} - c_{1,4} - c_{1,3} = 0, \tag{D.3.2b}$$
$$-c_{1,4} - c_{1,6} - c_{1,5} = 0, \tag{D.3.2c}$$
$$-c_{1,6} - c_{1,7} = 0, \tag{D.3.2d}$$
$$-c_{1,1} - c_{1,3} - c_{2,2} = 0, \tag{D.3.2e}$$
$$-c_{1,3} - c_{1,5} - c_{2,4} = 0, \tag{D.3.2f}$$
$$-c_{1,5} - c_{1,7} - c_{2,6} = 0. \tag{D.3.2g}$$

Solving these for $c_{2,i}$, $i = 2, 4, 6$, we get the matrices

$$T_5 = \begin{pmatrix} 2 & 1 \\ 1 & 2 \end{pmatrix}, \quad T_7 = \begin{pmatrix} 2 & 1 & 0 \\ 1 & 2 & 1 \\ 0 & 1 & 2 \end{pmatrix} \tag{D.3.3}$$

taking the same form as in (4.2.5).

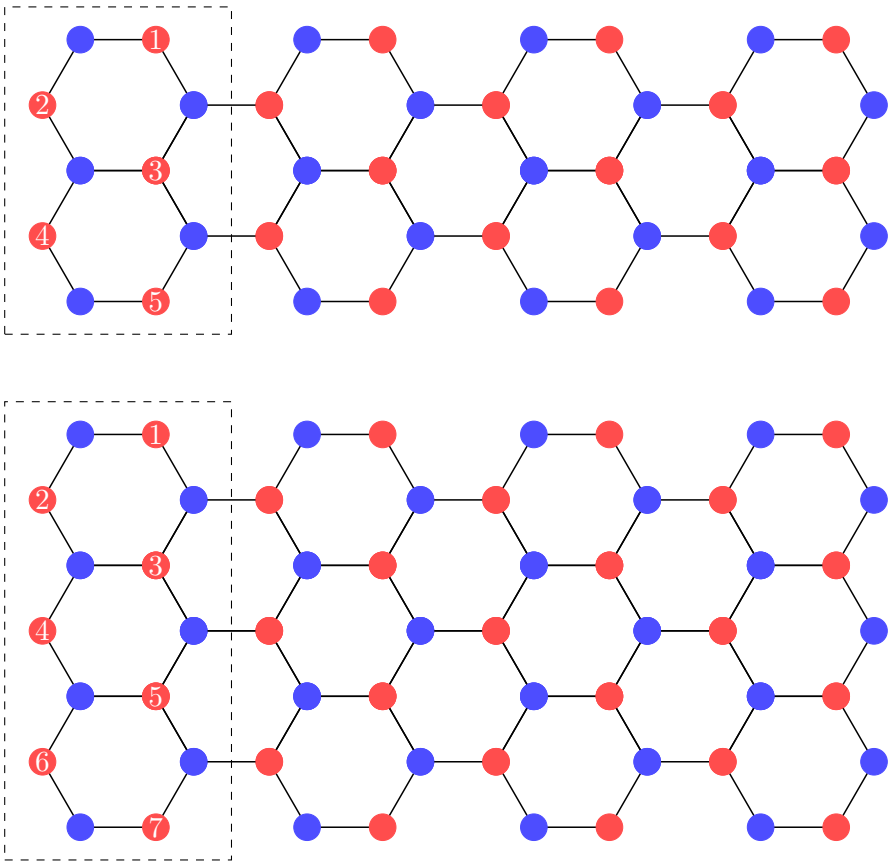

Figure D.3: Zigzag 5AGNR and 7AGNR. An edge state confined to the left edge will have zero amplitude on the blue sites.

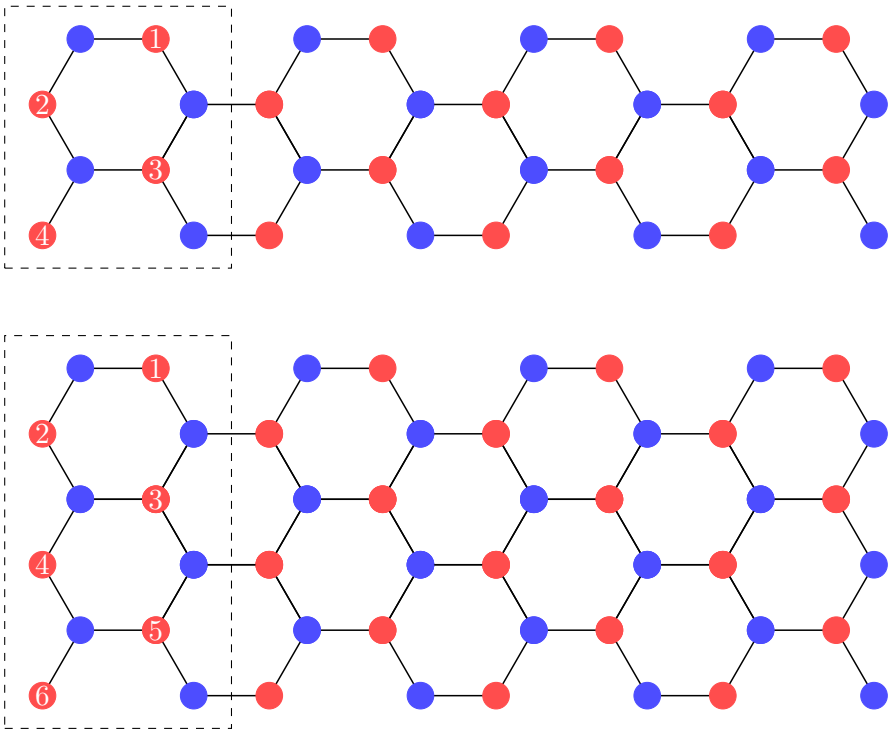

Figure D.4: Zigzag 4AGNR and 6AGNR.

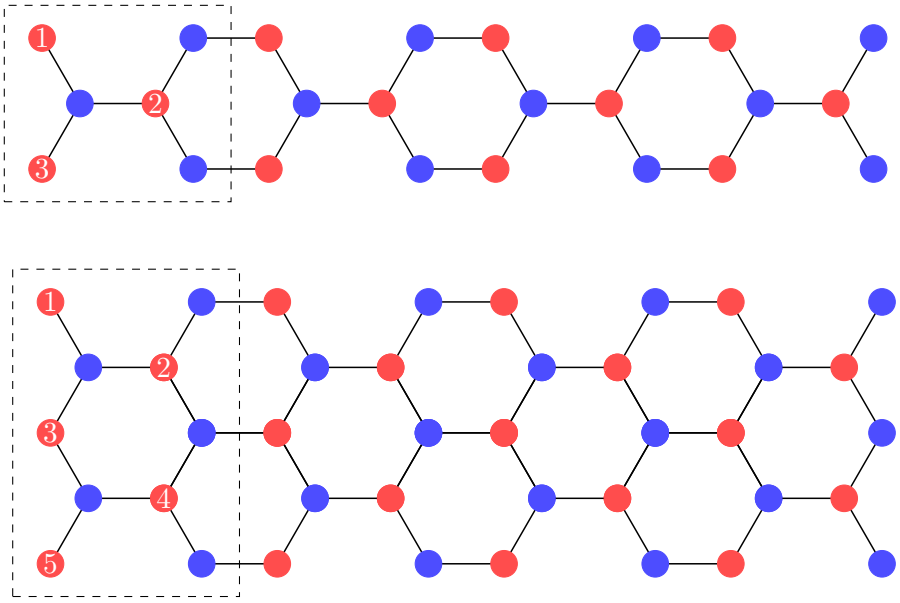

Figure D.5: The two smallest zigzag' AGNRs, with three and five rows.

For zigzag' 4AGNR and 6AGNR, the equations to be solved are (see Figure D.4)

$$c_{1,1} - c_{1,2} = 0, \tag{D.3.4a}$$
$$c_{1,2} - c_{1,4} - c_{1,3} = 0, \tag{D.3.4b}$$
$$c_{1,1} - c_{1,3} - c_{2,2} = 0, \tag{D.3.4c}$$
$$c_{1,3} - c_{2,4} = 0, \tag{D.3.4d}$$

and

$$c_{1,1} - c_{1,2} = 0, \tag{D.3.5a}$$
$$c_{1,2} - c_{1,4} - c_{1,3} = 0, \tag{D.3.5b}$$
$$c_{1,4} - c_{1,6} - c_{1,5} = 0, \tag{D.3.5c}$$
$$c_{1,1} - c_{1,3} - c_{2,2} = 0, \tag{D.3.5d}$$
$$c_{1,3} - c_{1,5} - c_{2,4} = 0, \tag{D.3.5e}$$
$$c_{1,5} - c_{2,6} = 0. \tag{D.3.5f}$$

Solving these for $c_{2,i}$, $i = 2, 4, 6$ we get the matrices

$$T_4 = \begin{pmatrix} 1 & 1 \\ 1 & 2 \end{pmatrix}, \quad T_6 = \begin{pmatrix} 1 & 1 & 0 \\ 1 & 2 & 1 \\ 0 & 1 & 2 \end{pmatrix}. \tag{D.3.6}$$

And finally, for the two smallest zigzag' AGNRs, we get the sets of equations (see Figure D.5)

$$-c_{1,1} - c_{1,3} - c_{1,2} = 0, \tag{D.3.7a}$$

$$-c_{1,2}-c_{2,1}=0, \tag{D.3.7b}$$

$$-c_{1,2}-c_{2,3}=0, \tag{D.3.7c}$$

and

$$-c_{1,1}-c_{1,3}-c_{1,2}=0, \tag{D.3.8a}$$

$$-c_{1,3}-c_{1,5}-c_{1,4}=0, \tag{D.3.8b}$$

$$-c_{1,2}-c_{2,1}=0, \tag{D.3.8c}$$

$$-c_{1,2}-c_{1,4}-c_{2,3}=0, \tag{D.3.8d}$$

$$-c_{1,4}-c_{2,5}=0. \tag{D.3.8e}$$

Solving these equations gives the transfer matrices

$$T_3=\begin{pmatrix}1 & 1\\ 1 & 1\end{pmatrix},\quad T_5=\begin{pmatrix}1 & 1 & 0\\ 1 & 2 & 1\\ 0 & 1 & 1\end{pmatrix}. \tag{D.3.9}$$

which has the same form as the matrix in (4.2.14).

Appendix E

Interface states in AGNR heterojunctions

In this appendix we show some examples of interface states between topologically equivalent and inequivalent AGNRs. The first example is between a zigzag 7AGNR and a zigzag' 5AGNR, which are topologically inequivalent, since the 7AGNR has one edge state and no Dirac point ($Z_2 = 1$), whereas the 5AGNR has one edge state and a Dirac point ($Z_2 = 0$). The Dirac point of 5AGNR changes its configuration to pair up with the edge state on 7AGNR, while the edge state on 5AGNR is left unpaired.

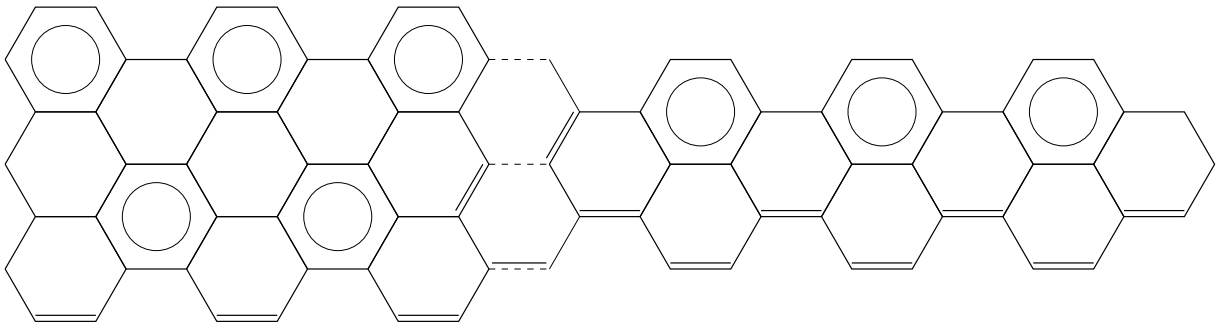

Figure E.1: A zigzag 7AGNR and zigzag' 5AGNR joined together have one interface state.

If we pair zigzag 6AGNR and zigzag 8AGNR, we expect to find one interface state, as they are inequivalent.
Here the Dirac point changes the configuration of its bonds again to pair up with the unpaired site on the opposite AGNR, and we are left with one interface state as expected. If we combine two bearded ribbons with 8 and 10 rows, the heuristic model predicts zero edge states, see Figure E.3

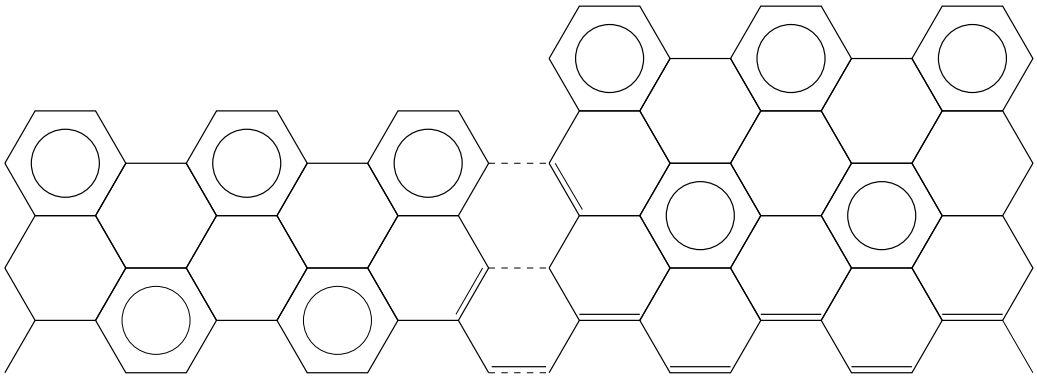

Figure E.2: Pairing two zigzag AGNRs with 6 and 8 rows we find one interface state in the heuristic model.

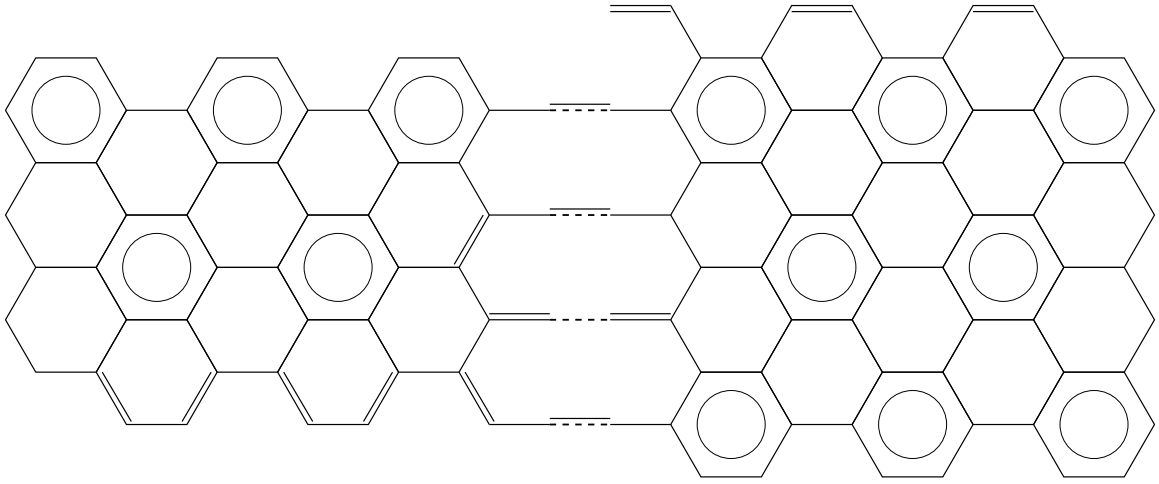

Figure E.3: Combining two bearded AGNRs with 8 and 10 rows each, the heuristic model predicts zero interface states, because the Dirac chain of 8AGNR changes its configuration to pair up with one of the edge states on 10AGNR.

Appendix F

Edge states in (6,6,12) phase diagram

In this appendix we show the relation between Dirac points and edge states, using (6,6,12)-graphyne as an example. We show how we need to close a gap in the band structure to add or remove an edge state from the system.

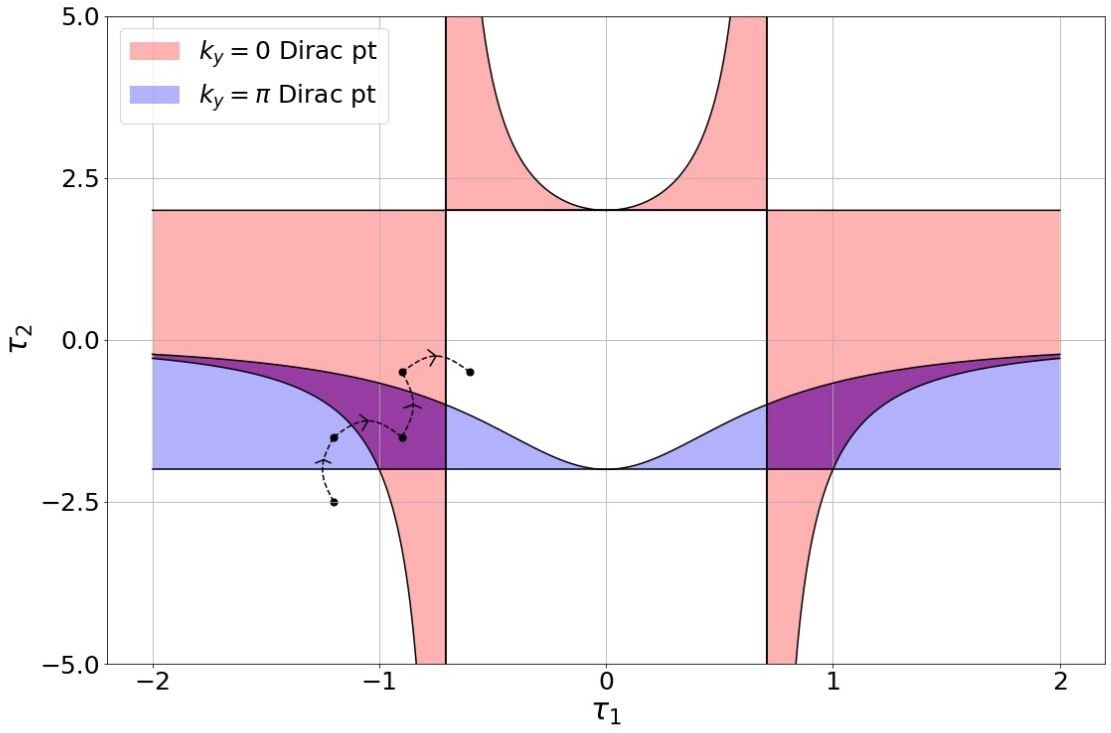

Figure F.1: Path taken in the phase diagram of (6,6,12)-graphyne. The values at each point are, $(\tau_1, \tau_2) = (-1.2, -2.5)$, $(-1.2, -1.5)$, $(-0.9, -1.5)$, $(-0.9, -0.5)$, $(-0.6, -0.5)$.

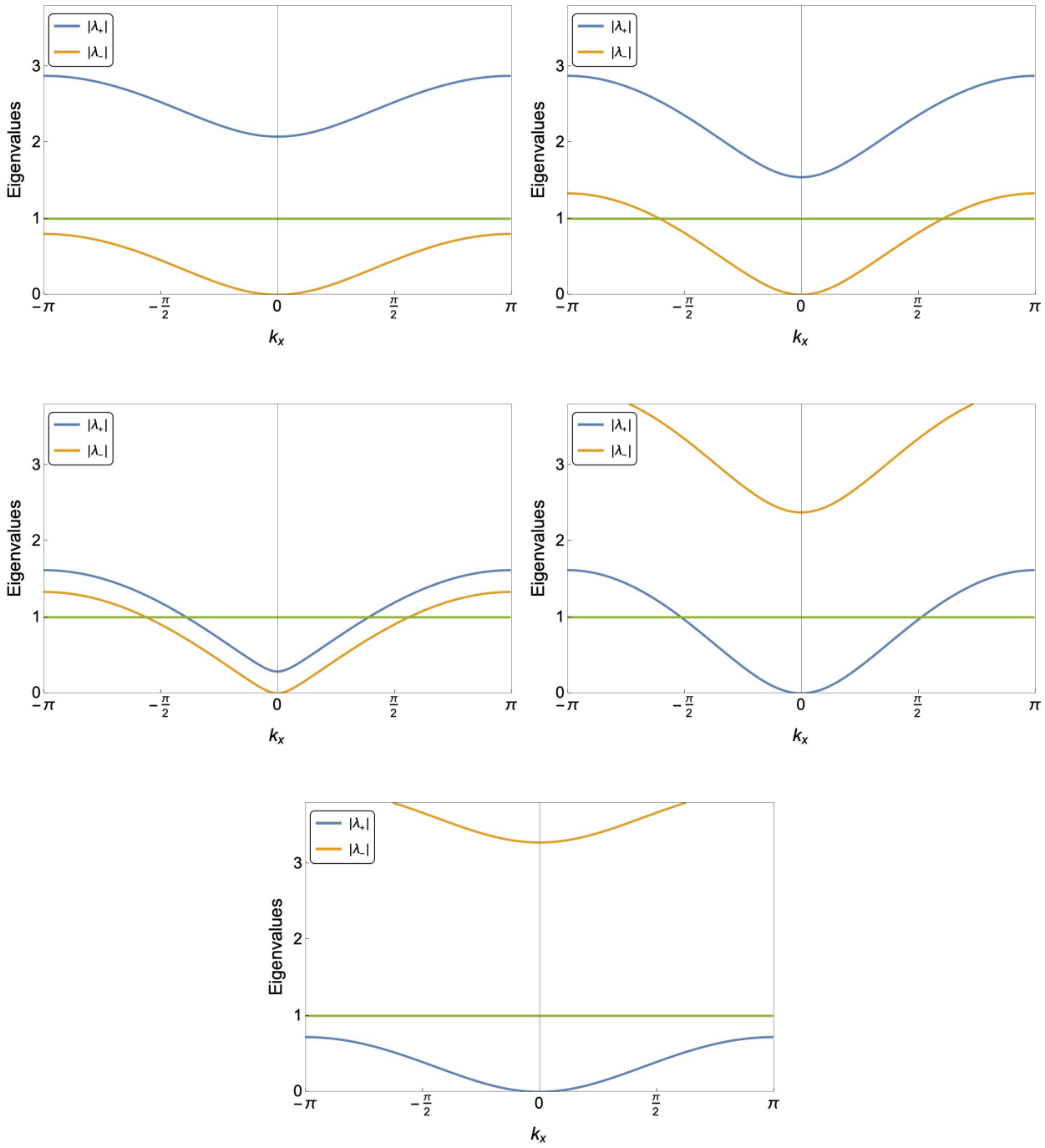

Figure F.2: Eigenvalues of the transfer matrix for (6,6,12)-graphyne in five different regions of the phase diagram.

Appendix G

Berry phase for generic A-B Hamiltonian

We derive an expression for the Berry phase at the Dirac point of an A-B Hamiltonian when the two sublattice Hamiltonians do not have the same zero-energy eigenstate, i.e. $h_A |\phi_A\rangle = 0$, $h_B |\phi_B\rangle = 0$, $|\phi_A\rangle \neq |\phi_B\rangle$. The derivation is similar to the one done for $|\phi_A\rangle = |\phi_B\rangle$ in section 5.6. Let $h(\mathbf{k})$ be a nearest neighbour tight-binding Hamiltonian that has two sublattice components, h_A and h_B, such that

$$h(\mathbf{k}) = \begin{pmatrix} 0 & 1 \\ 0 & 0 \end{pmatrix} \otimes h_A(\mathbf{k}) + \begin{pmatrix} 0 & 0 \\ 1 & 0 \end{pmatrix} \otimes h_B(\mathbf{k}) = \sigma_x \otimes h_x(\mathbf{k}) + \sigma_y \otimes h_y(\mathbf{k}), \tag{G.1}$$

where $h_x(\mathbf{k}) = (h_A(\mathbf{k}) + h_B(\mathbf{k}))/2$ and $h_y(\mathbf{k}) = i(h_A(\mathbf{k}) - h_B(\mathbf{k}))/2$. By hermiticity of the full Hamiltonian, $h_A(\mathbf{k}) = h_B(\mathbf{k})^\dagger$. If the A sublattice has a zero-energy eigenstate, $|\phi_A\rangle$, the B sublattice also has one, $|\phi_B\rangle$. The linear combination $|\psi\rangle = \alpha |\uparrow\rangle \otimes |\phi_B\rangle + \beta |\downarrow\rangle \otimes |\phi_A\rangle$ is also an eigenstate. $|\uparrow / \downarrow\rangle$ refers to the sublattice component of states localised to the B and A sublattices respectively. If the Dirac point is at $\mathbf{k} = \mathbf{k}^*$, we expand $h_x(\mathbf{k})$ and $h_y(\mathbf{k})$ around this point. To first order in the deviation $\mathbf{q}$, the Schrödinger equation is

$$\left(h_x^{(0)}(\mathbf{k}^*) + h_y^{(0)}(\mathbf{k}^*) + h_x^{(1)}(\mathbf{q}) + h_y^{(1)}(\mathbf{q})\right)(\alpha |\uparrow\rangle \otimes |\phi_B\rangle + |\downarrow\rangle \otimes |\phi_A\rangle) = E(\alpha |\uparrow\rangle \otimes |\phi_B\rangle + |\downarrow\rangle \otimes |\phi_A\rangle). \tag{G.2}$$

Taking the inner product with $\langle\uparrow|$ and $\langle\downarrow|$ yields two equations

$$\alpha h_x^{(1)}(\mathbf{q}) |\phi_B\rangle + i\alpha h_y^{(1)}(\mathbf{q}) |\phi_B\rangle = \beta E |\phi_A\rangle, \tag{G.3a}$$

$$\beta h_x^{(1)}(\mathbf{q}) |\phi_A\rangle - i\beta h_y^{(1)}(\mathbf{q}) |\phi_A\rangle = \alpha E |\phi_B\rangle. \tag{G.3b}$$

We multiply both sides of (G.3a) from the left by $\langle\phi_A|$ and both sides of (G.3b) by $\langle\phi_B|$ to get

$$\begin{pmatrix} 0 & d_x(\mathbf{q}) - id_y(\mathbf{q}) \\ d_x^*(\mathbf{q}) + id_y^*(\mathbf{q}) & 0 \end{pmatrix} \begin{pmatrix} \alpha \\ \beta \end{pmatrix} = E \begin{pmatrix} \alpha \\ \beta \end{pmatrix}, \tag{G.4}$$

where $d_x(\mathbf{q}) = \langle\phi_B|h_x^{(1)}(\mathbf{q})|\phi_A\rangle$ and $d_y(\mathbf{q}) = \langle\phi_B|h_y^{(1)}(\mathbf{q})|\phi_A\rangle$. As they are off-diagonal elements of hermitian matrices they are not necessarily real, so we write each as $d_i = \mathrm{Re}(d_i) + i\mathrm{Im}(d_i)$. Defining $\boldsymbol{v}_1$ and $\boldsymbol{v}_2$ through

$$\boldsymbol{v_1} \cdot \mathbf{q} = \mathrm{Re}(d_x) + \mathrm{Im}(d_y), \tag{G.5}$$

and

$$\boldsymbol{v_2} \cdot \mathbf{q} = \mathrm{Im}(d_x) - \mathrm{Re}(d_y), \tag{G.6}$$

the above equation reads

$$(\boldsymbol{v}_1 \cdot \mathbf{q}\,\tau_x + \boldsymbol{v}_2 \cdot \mathbf{q}\,\tau_y) \begin{pmatrix} \alpha \\ \beta \end{pmatrix} = E \begin{pmatrix} \alpha \\ \beta \end{pmatrix}, \tag{G.7}$$

bringing it to the form of (5.6.4). The Berry phase in the lower band is then given by

$$\gamma = \pi \frac{\boldsymbol{v_1} \times \mathbf{v_2}}{|\boldsymbol{v_1} \times \mathbf{v_2}|} \cdot \hat{\mathbf{z}}. \tag{G.8}$$